Review

Structure and dynamics of the oceanic lithosphere-asthenosphere system

Fred Richards[a,b,*], Mark Hoggard[b,c], Alistair Crosby[d], Siavash Ghelichkhan[e], Nicky White[f]

[a] *Department of Earth Science and Engineering, Imperial College London, UK*
[b] *Department of Earth and Planetary Sciences, Harvard University, Cambridge, USA*
[c] *Lamont-Doherty Earth Observatory, Columbia University, New York, USA*
[d] *BP Exploration Ltd., Sunbury-on-Thames, London, UK*
[e] *Research School of Earth Sciences, Australian National University, Canberra, Australia*
[f] *Bullard Laboratories, Department of Earth Sciences, University of Cambridge, UK*

ARTICLE INFO

ABSTRACT

The thermochemical evolution of oceanic lithosphere and its interaction with the underlying asthenosphere exerts a fundamental control on the dynamics of the Earth system. Since the 1960s, the range, accuracy and spatial coverage of geophysical and geochemical datasets collected in the oceanic realm have substantially increased. These additional constraints have helped to elucidate many aspects of the lithosphere-asthenosphere system, but some apparently contradictory observations have presented additional interpretational challenges. Here, we summarise the merits, limitations and ambiguities of available observational constraints on the thermomechanical evolution of oceanic upper mantle. Newly developed cooling models are generally compatible with these constraints, although there is evidence for systematic differences in behaviour between different oceanic basins. Subsidence, magnetotelluric and seismological observations from the Pacific Ocean are consistent with plate rather than half-space cooling models, whereas results from the Atlantic and Indian Oceans are more equivocal. We provide an overview of proposed mechanisms for seafloor flattening and we show that regional deviations from globally averaged trends can be attributed to asthenospheric temperature variation and to local changes in lithospheric thickness. Although the plate cooling model generally provides a good description of available observations, it is probably a crude approximation of the dynamic processes operating within the thermal boundary layer that underlies oceanic basins. By incorporating mantle density structure inferred from surface wave tomography into more sophisticated convection simulations, we show that the plate model provides a good approximation of the predicted age-dependent behaviour of bathymetric and gravity fields. While the results presented here suggest a unified understanding of the lithosphere-asthenosphere system is within reach, unambiguous evidence for small-scale convection at the base of the lithosphere remains elusive. As a result, the precise mechanism responsible for sea-floor flattening has yet to be identified. It is also unclear why models that incorporate the effect of phase changes such as the garnet-spinel transition tend to fit observations less well than simpler counterparts. These outstanding controversies suggest further research is needed to develop a complete description of the structure and dynamics of the oceanic upper mantle but, encouragingly, the tools at our disposal have never been more powerful.

1. Introduction

Age-progressive cooling and thermal contraction of oceanic lithosphere is one of the most extensively studied and universally acknowledged Earth processes in modern geophysics. With magnetic anomalies confirming the theory of mid-ocean ridge spreading, it became clear in the early 1960s that both seafloor elevation and heat flow decrease systematically as a function of increasing oceanic crustal age (Hess, 1962; Vine and Matthews, 1963; Wilson, 1965). Later that decade, pioneering work by Turcotte and Oxburgh (1967) and McKenzie (1967) demonstrated that these first-order observational trends can be satisfactorily explained using simple models of conductive cooling. The simplest of these models is the half-space cooling model, which proposes that oceanic lithosphere steadily cools by conduction of heat to the surface in a semi-infinite half-space, with an initial temperature profile defined by a fixed potential temperature at the mid-ocean ridge (Fig. 1a; Turcotte and Oxburgh, 1967). Subsidence and heat flow are proportional to the square-root of crustal age, and this cooling

* Corresponding author at: Department of Earth Science and Engineering, Imperial College London, UK.
  E-mail address: f.richards19@imperial.ac.uk (F. Richards).

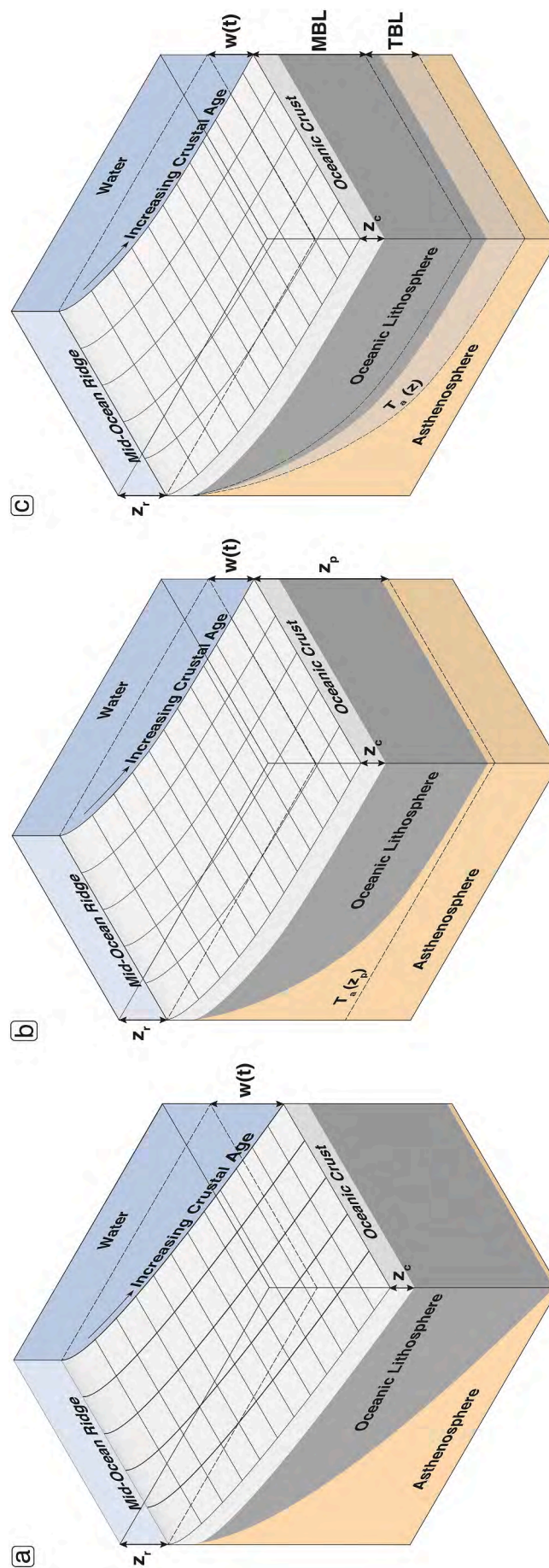**Fig. 1.** Thermal models of oceanic lithosphere. (a) Half-space cooling model. z_c = crustal thickness; z_r = zero-age ridge depth; $w(t)$ = subsidence as a function of age. (b) Plate model. z_p = plate thickness; $T_a(z_p)$ = adiabatic temperature at z_p. (c) Boundary layer model. MBL = mechanical boundary layer; TBL = thermal boundary layer; $T_a(z)$ = adiabatic temperature at base of TBL.

process is predicted to continue indefinitely. However, as the quantity and quality of observations from older portions of the oceanic basins grew throughout the 1970s, it was observed that measurements of shiptrack bathymetry and heat flow at ages greater than ∼70 Ma appear to asymptotically approach a constant value (e.g. Sclater and Francheteau, 1970). This behaviour indicates that some physical mechanism is resupplying basal heat at older ages leading the geotherm to evolve towards a steady-state profile. This thermal structure can be approximated using a plate cooling model, whereby an additional physical constraint is introduced such that the temperature at a specific depth is fixed through time (the *plate thickness*; Fig. 1b; McKenzie, 1967).

Over the intervening decades, the plate cooling model has been successfully applied to explain subsidence and heat flow observations in a manner consistent with available independent constraints (Parsons and Sclater, 1977; Stein and Stein, 1992; McKenzie et al., 2005; Richards et al., 2018). However, the precise mechanism by which heat is resupplied to the base of oceanic plates has remained a subject of debate. Many studies argue that this process occurs by small-scale convection, since thickening of the lithosphere beyond a critical threshold leads to the initiation of Rayleigh-Taylor instabilities, placing an effective upper limit on oceanic plate thickness (McKenzie and Weiss, 1975; Parsons and McKenzie, 1978; Robinson and Parsons, 1988; Huang and Zhong, 2005; Section 3.3). Although it does not incorporate the dynamics of convection, proponents of the plate model believe that it represents a valid approximation of the actual thermal state of oceanic lithosphere (Parsons and McKenzie, 1978; Crosby et al., 2006). The depth at which temperature is fixed in this model occurs, in reality, between the base of the mechanical lid and the base of the thermal boundary layer at old ages (Fig. 1c; see Section 5.3). However, detractors argue that this phenomenological model is insufficiently sophisticated to accurately capture the impact of small-scale convection and possible resupply of heat by plumes on lithospheric thermal structure (Davies, 1988; Korenaga and Korenaga, 2008; Sleep, 2011). In an effort to better approximate the thermal consequences of small-scale convection, Doin and Fleitout (1996) proposed a formulation in which a constant heat flux boundary condition is applied at a specified isotherm, rather than a constant temperature. However, this model requires the existence of steep temperature gradients at the base of the cooling plate close to the ridge axis that are inconsistent with expected axial temperature profiles, which are dominantly controlled by adiabatic decompression and melting.

Since these thermal models were originally proposed, several important advances have further refined our understanding of the temporal evolution of oceanic lithosphere. First, experimental work has placed tighter constraints on thermophysical parameters of key minerals such as olivine, which makes up > 75% of the mantle lithosphere (Dick et al., 1984; Boyd, 1989). Variations of thermal conductivity, expansivity and heat capacity as a function of both pressure and temperature are now well established (Fei and Saxena, 1987; Gillet et al., 1991; Berman and Aranovich, 1996; Bouhifd et al., 1996; Hofmeister, 2005; Pertermann and Hofmeister, 2006; Hofmeister, 2007; Hofmeister and Pertermann, 2008; Benisek et al., 2012). Secondly, improvements in computing power, the quantity of seismograms, seismic tomographic methods, and a focus on surface waves have resulted in high-resolution models that reveal the shear-wave velocity structure and seismic anisotropy of the lithosphere-asthenosphere system in unprecedented detail (Burgos et al., 2014; Debayle et al., 2016; Schaeffer et al., 2016; Ho et al., 2016). Thirdly, subsidence and heat flow datasets that more accurately account for variations in crustal thickness, sediment thickness and hydrothermal circulation have helped to reduce uncertainties on these key observations (Hasterok et al., 2011; Hoggard et al., 2017; Richards et al., 2018). Finally, the growing number of magnetic reversal picks have enabled the creation of increasingly accurate global grids of oceanic crustal age, although mispicks, gridding artifacts, and necessary interpolations between picks (particularly problematic for the

83.0–120.6 Ma Cretaceous normal polarity superchron) can introduce errors of up to 10 Myr in some locations (Müller et al., 2008, 2016; Rowley, 2018).

In this review, we show how these recent advances have shed new light on the general behaviour of the oceanic lithosphere-asthenosphere system. Two major, interlinked questions that motivate much of this discussion are: (a) is it more appropriate to use half-space or plate cooling models to represent the thermal structure of oceanic regions? and, (b) what are the implications for mantle rheology, which controls many of the physical processes we observe in oceanic lithosphere? We therefore first provide an in-depth overview of the modern observational datasets used to interrogate these issues. Secondly, we demonstrate how these recently collected datasets can be combined with insights from mineral physics to build comprehensive thermal models that simultaneously satisfy available constraints on the thermal and rheological structure of the crust and upper mantle. Thirdly, we demonstrate how deviations from the globally averaged behaviour of oceanic lithosphere can be used to glean novel insights into less well understood processes, such as melt generation, dynamic topography, boundary layer convection and mantle rheology. Lastly, we discuss outstanding controversies and suggest avenues of research that will likely be key to resolving them.

2. Observational constraints on the structure and rheology of oceanic lithosphere

A wide range of data types have been used to investigate the physical state of oceanic lithosphere. The first to be extensively collected were ship-board measurements including bathymetry and heat flow, which yield information on its integrated thermal structure (Fig. 2). Over the past few decades, the growing number of seismological and, more recently, magnetotelluric studies have significantly improved resolution of deeper parts of the lithosphere and asthenosphere. The variable sensitivity of each dataset to different properties means that, when applied in combination, parameter trade-offs and ambiguity found in earlier studies can be significantly reduced.

2.1. Subsidence measurements

Mid-ocean ridges typically sit 2.5–3.0 km below sea level (Dalton et al., 2014; Gale et al., 2014). Due to isostasy, the cooling, contraction and densification of oceanic lithosphere through time produces a systematic increase in basement depth with age. Although bathymetric soundings have been collected since the late 1800s, comprehensive and reliable global compilations have been lacking until recently for two important reasons. First, oceanic crust is of variable thickness and is generally covered by sediment, particularly close to continental margins where increased supply of siliciclastic material results in sediment thicknesses that regularly exceed 1 km. Crustal isostasy and sedimentary loading therefore break the direct connection between observed bathymetry and thermal structure of the underlying lithosphere. This issue can be circumvented in one of two ways. The first involves exclusion of affected areas by excising locations covered by thick sediment, seamounts, oceanic plateaux and fracture zones, using maps of bathymetry and short-wavelength free-air gravity anomalies, whilst applying an isostatic correction for sedimentary loading elsewhere using global grids of sediment thickness (Hillier and Watts, 2005; Crosby et al., 2006; Korenaga and Korenaga, 2008; Crosby and McKenzie, 2009; Hillier, 2010). Unfortunately, the remaining measurements may still be inaccurate, whilst also being spatially biased towards the Pacific Ocean and to younger lithospheric ages, thus compromising their global applicability.

An alternative approach involves correcting for oceanic crustal thickness variations and sedimentary loading, requiring accurate constraints on the local thickness and density of sediment and oceanic crust (Winterbourne et al., 2009; Czarnota et al., 2013; Winterbourne et al.,
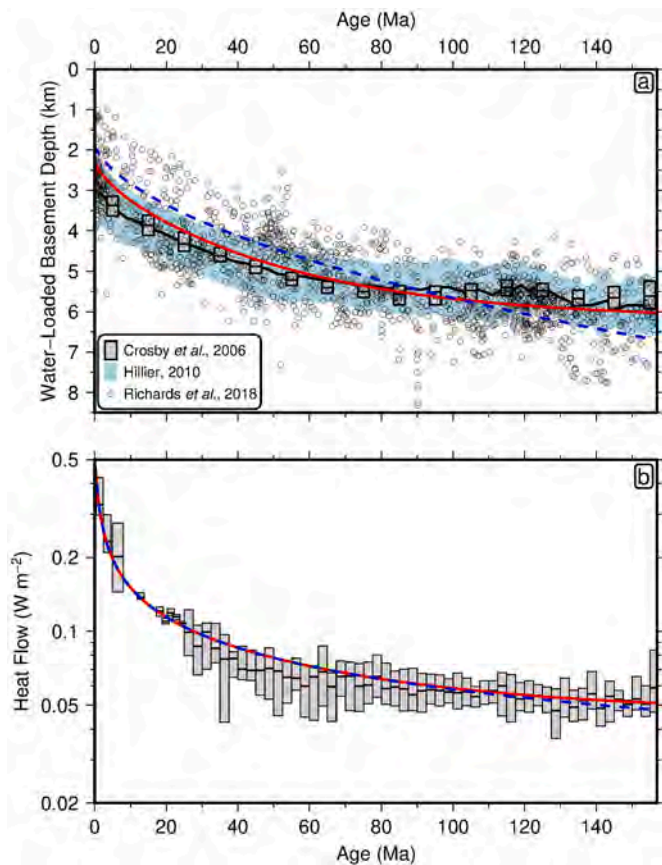
Fig. 2. Subsidence and heat flow constraints on thermal evolution of oceanic lithosphere. (a) Water-loaded depth to oceanic basement as function of plate age. Black circles = spot measurements from controlled-source seismic surveys corrected for sedimentary loading and crustal thickness variations (Hoggard et al., 2017; Richards et al., 2018); black line/blue envelope = mean and 2σ errors for 'normal' seafloor corrected for sedimentary loading using global sediment thickness grid (Hillier, 2010); grey boxes with bars = median and interquartile range following excision of areas inferred to be affected by dynamic topography using long-wavelength gravity anomalies (Crosby et al., 2006); dashed blue line = predicted subsidence from geochemically constrained (T_p = 1333°C) optimal half-space cooling model (z_r = 1906 m); red line = same for geochemically constrained (T_p = 1333°C) optimal plate model (z_p = 132 km; z_r = 2292 m). (b) Surface heat flow as function of plate age; grey boxes with bars = median and interquartile ranges of measurements corrected for sedimentation rates and filtered to remove hydrothermal circulation (Richards et al., 2018); dashed blue line = predicted heat flow from optimal half-space cooling model; red line = same for optimal plate model.

2014; Hoggard et al., 2017). International Ocean Drilling Program (IODP) and Deep Sea Drilling Program (DSPD) boreholes provide useful constraints on sedimentary thickness versus density relationships, but they are sparse and rarely penetrate the whole sediment pile (Johnson and Carlson, 1992). In contrast, active source marine seismic experiments generally image the sediment-basement interface and sometimes the Moho, although seismic reflection surveys require a velocity model to convert from two-way travel time (TWTT) into true thickness. This methodology has at present been applied to inventories of > 2000 marine seismic experiments, yielding well-resolved spot measurements of water-loaded basement depth (Hoggard et al., 2017). Although these data are more robust than estimates obtained from global grids, they are still spatially biased, this time towards passive margins where hydrocarbon exploration is focused. Despite these divergent approaches, average subsidence trends from the high accuracy spot measurements are comparable with compilations from global grids (Fig. 2a).

The second important consideration when constructing an observational database of basement depths is the potential bias that may arise from dynamic topographic variations that are supported by convection in the underlying mantle, which remains a subject of some controversy (Hoggard et al., 2016; Yang and Gurnis, 2016; Steinberger et al., 2019; Davies et al., 2019). Prior to the 1990s, ship-track bathymetric measurements were heavily concentrated in the North Pacific and North Atlantic Oceans, with significant gaps in the South Pacific and South Indian Oceans (Parsons and Sclater, 1977; Stein and Stein, 1992). Due to this limited spatial extent, long-wavelength dynamic topography arising from deep mantle flow may have systematically biased subsidence trends (Cazenave and Lago, 1991; Watkins and Conrad, 2018). Crosby et al. (2006) and Crosby and McKenzie (2009) attempted to mitigate this bias by excising regions with positive or negative long-wavelength gravity anomalies. This approach assumes a strong correlation between convectively generated topography and free-air gravity anomalies, which, although generally thought to be valid for short-wavelength convection cells in the shallow mantle, breaks down for longer-wavelength contributions sourced from the deeper mantle (Colli et al., 2016). The most recent compilations rely on the assumption that dynamic topography is approximately evenly distributed as a function of plate age. Thus, an extensive geographical footprint ensures recovery of the average bathymetry, although data points at older ages inevitably become more spatially localised. Nevertheless, even for ages > 150 Ma, the large number of near-margin data points in the spot measurements of Richards et al. (2018) results in extensive coverage at old ages within all ocean basins, which at least partly mitigates this potential bias.

As the coverage and accuracy of subsidence measurements has substantially improved in recent years, the apparent flattening at old ages has remained a consistent feature. It is possible to generate acceptable fits to this data using half-space cooling parameterisations, but best-fitting models require either implausibly cold potential temperatures (< 1100°C) or shallow ridge depths (~2 km; Hoggard et al., 2017; Richards et al., 2018). This flattening behaviour has therefore generally been used to argue in favour of plate cooling models, which yield more realistic thermal parameters. However, subsidence data in isolation cannot be used to uniquely determine the optimal potential temperature and plate thickness. Since subsidence depends upon the vertically integrated density change, the required density increase can either be generated by modest cooling over a large depth range, or by more significant cooling over a smaller depth range. Mantle potential temperature and plate thickness therefore trade off strongly against one another, resulting in a large range of potential thermal structures that each satisfy the subsidence data. This non-uniqueness, combined with differences in the parameterisation of heat transport properties, has led to a wide range of suggested plate thicknesses (90–135 km) and mantle temperatures (1280–1450°C; Parsons and Sclater, 1977; Stein and Stein, 1992; Doin and Fleitout, 1996; McKenzie et al., 2005; Grose and Afonso, 2013; Richards et al., 2018). Nevertheless, if resupply of basal heat is occurring by small-scale convection, the rate and spatial variability of flattening contains important information on the rheology and density structure of the upper mantle (Parsons and McKenzie, 1978; Huang and Zhong, 2005).

2.2. Heat flow measurements

Oceanic lithosphere steadily cools as heat escapes through the surface. With time, the temperature gradient beneath the surface reduces, causing a progressive decrease in conductive heat flow. Therefore, if thermal conductivity is known, heat flow as a function of age can place important constraints on the thermal evolution of oceanic lithosphere (McKenzie, 1967). One major benefit of this constraint is that, due to the long thermal time constant of an oceanic plate (i.e., the e-folding time of conductive cooling, which is ~70 Myr for a 150 km-thick layer of silicates), transient asthenospheric temperature perturbations associated with sub-plate convection cause only modest deviations in heat

flow in comparison to the associated deviations in subsidence (McKenzie, 1967; Turcotte and Schubert, 2002).

The most reliable heat flow values are obtained by inserting thermistor probes into the seafloor in thickly sedimented regions and measuring the local temperature gradient. Care must be taken to account for three important effects. First, sediments have a thermal conductivity of ~1 W m^{-1} K^{-1}, which is approximately half that of oceanic crust (Clark, 1966; Erikson, 1973; Waples and Waples, 2004; Kelemen et al., 2004). Thus accurate measurements of this property are also required, which are best obtained directly on the ship before samples have time to desiccate. Secondly, sediment rains out of the ocean at the temperature of bottom water. High sedimentation rates therefore suppress the temperature gradient by up to ~20% and cause underestimates of the basement heat flow, which can be locally corrected using analytical solutions (Von Herzen and Uyeda, 1963; Hasterok, 2013; Richards et al., 2018).

The third and potentially most significant effect occurs on young oceanic lithosphere, where vigorous hydrothermal circulation at shallow depths can result in significant advective heat loss and considerable scatter in heat flow measurements (Lister, 1980). This issue initially prevented early studies from using these measurements alongside subsidence data to determine best-fitting values of thermal model parameters (e.g. Parsons and Sclater, 1977). However, deposition of sedimentary cover does eventually seal fluid pathways, ensuring that stable heat flow values representative of basal conduction can be obtained once sedimentary thicknesses exceed ~400 m (Lister, 1972; Hasterok et al., 2011). Moreover, beyond ~65 Ma, hydrothermal circulation is thought to contribute negligibly to heat flow (Stein and Stein, 1992; Hasterok, 2013; Grose and Afonso, 2015). Thus by excluding data near seamounts or with insufficient sediment cover, hydrothermally induced scatter in oceanic heat flow values for ages greater than 25 Ma can largely be eliminated. However, in younger regions, only a few focused studies specifically targeting areas of high sedimentation are typically deemed to be sufficiently accurate for comparison to thermal models (Hasterok, 2013). Even in these thickly sedimented regions, complex hydrothermal circulation patterns may result in heat flow values that either exceed or fall short of values expected for purely conductive heat transport (Grose and Afonso, 2015). Consequently, although inclusion of these site-specific heat flow estimates places useful constraints on optimal model parameters, inferred 0–25 Ma heat flow trends are subject to greater spatial bias and higher uncertainty than those at older ages.

Despite the caveats associated with these careful filtering and correction procedures, as well as a more limited spatial coverage in comparison to bathymetric measurements, heat flow measurements do approach a steady-state value at ages > 100 Ma (Fig. 2b). This observation was initially regarded as independent support for the resupply of basal heat inherent to the plate-cooling model, since predicted heat flow values were expected to diverge beyond 70 Ma in the early analytical cooling models with constant thermal properties (Parsons and Sclater, 1977; Stein and Stein, 1992). However, it is important to note that this is not the case for cooling models which account for pressure- and temperature-dependence of thermal properties and include an insulating 7 km-thick crustal layer. These models predict that, even by 160 Ma, divergence in predicted heat flow is only ~5%, which is comparable to measurement uncertainties (Fig. 2b; Richards et al., 2018). While divergence does increase beyond 160 Ma in these predictions, heat flow measurements at these older ages are scarce and geographically restricted, so may be unrepresentative of average behaviour. Thus, it is not clear that it is possible to discriminate between half-space and plate cooling models on the basis of heat flow data alone. Nevertheless, when plate cooling models are constrained using heat flow in isolation, optimal plate thicknesses tend to be thinner (75–120 km) and mantle temperatures higher (1350–1450°C) than those determined from fitting subsidence measurements (Stein and Stein, 1992; Grose, 2012; Hasterok, 2013). Crucially, the trade-off

between these two variables is less pronounced than for basement depths, meaning that joint fitting of subsidence and heat flow datasets can markedly reduce parameter uncertainty.

2.3. Seismological observations

A wide range of seismological observations on oceanic lithosphere have been obtained from a mixture of passive source (earthquakes) and active source (airguns and explosives) experiments. Here, we provide a brief overview of these techniques, including their respective limitations and sensitivity to mantle structure, composition, and rheology.

2.3.1. Surface wave dispersion

The shear modulus of peridotite is strongly dependent on temperature (Isaak, 1992; Cammarano et al., 2003; Stixrude and Lithgow-Bertelloni, 2005; Schutt and Lesher, 2006). Moreover, recent experimental studies show that, at near-solidus conditions in the upper mantle, the passage of seismic waves induces viscoelastic deformation of mantle minerals, resulting in attenuation of seismic energy and a strong reduction of shear-wave velocity (Faul and Jackson, 2005; McCarthy and Takei, 2011; Faul and Jackson, 2015; Yamauchi and Takei, 2016). Observational constraints on shear-wave velocity (and attenuation) therefore contain useful information about the thermal structure of oceanic lithosphere and asthenosphere.

Lithospheric cooling models predict two broad patterns. At any given depth, velocities are expected to systematically increase as a function of plate age as material cools. In addition, at any specific location, velocities are expected to first reduce with depth across the transition from colder conducting lithosphere into warm asthenosphere, where geotherms make their closest approach to the solidus, before increasing again deeper into the mantle as pressure effects begin to dominate over the adiabatic temperature gradient. Over the past two decades, many different studies have successfully imaged this cooling signal (Ritzwoller et al., 2004; Priestley and McKenzie, 2006, 2013; Beghein et al., 2014).

Since olivine dominates upper mantle mineralogy and is highly anisotropic, a number of studies have also used changes in azimuthal anisotropy to infer the transition between the mechanical lithosphere, where fast directions are predominantly frozen in parallel to the fossil spreading direction, and the underlying asthenosphere, where orientations can vary according to mantle flow patterns. These results indicate a deepening of the transition between the lithosphere and asthenosphere as a function of plate age, up to a maximum depth of ~110 km (Fig. 3a and b; Burgos et al., 2014; Schaeffer et al., 2016; Steinberger and Becker, 2018; Russell et al., 2019).

Surficial observations, such as subsidence and heat flow, yield bulk constraints on the integrated thermal evolution of oceanic lithosphere, but are sensitive to trade-offs between parameters such as potential temperature and plate thickness. A key advantage of regional surface wave dispersion studies is that vertical variations in seismic velocity provide a more direct probe of the distribution of temperature with depth, although vertical resolution in these models is currently limited to ~20 km (Beghein et al., 2018). Nevertheless, debate remains over whether these seismological constraints are in better agreement with half-space cooling or plate cooling models, with some studies suggesting systematic differences in behaviour between basins (Ma and Dalton, 2019; Fig. 3a and c). As seismological constraints continue to improve, surface wave models using larger quantities of data, higher modes, and more advanced inversion techniques will provide crucial insights into processes operating at the lithosphere-asthenosphere interface. One such target is the possibility of detecting whether small-scale convection is indeed responsible for observed 'flattening' in global seafloor subsidence and heat flow trends.

2.3.2. Seismic attenuation

Seismic attenuation refers to the observed loss of energy and
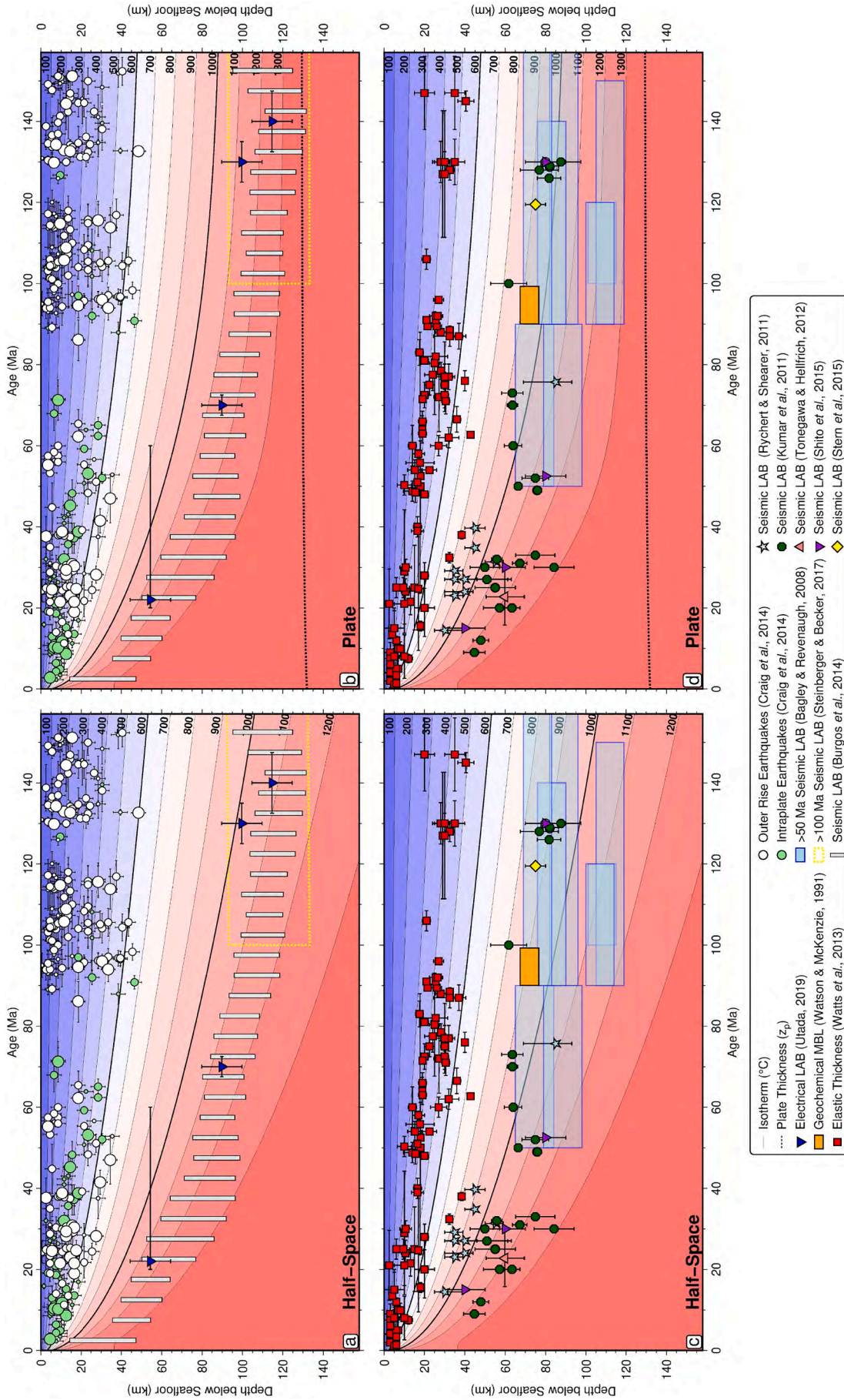
Fig. 3. Geophysical and geochemical observations pertaining to the thermal evolution of oceanic lithosphere. (a) Predicted thermal structure of geochemically constrained optimal half-space cooling model (T_p = 1333°C; z_r = 1906 m) overlaid with selected seismological and magnetotelluric observations. Numbered contours = isothermal surfaces plotted in °C; green/white circles with error bars = oceanic intraplate/outer rise earthquakes (Craig et al., 2014) where small/medium/large size = M_b < 5.5/5.5 ≤ M_b ≤ 6.5/5.5 ≤ 6.5/M_b > 6.5; vertical grey bars = Pacific LAB inferred using depth to top of layer in which azimuthal anisotropy aligns with absolute motion (Burgos et al., 2014); dashed yellow box = envelope of LAB depths, assumed to correspond to 1132 °C isothermal surface, for plate ages > 100 Ma from array of seismic tomography models (Steinberger and Becker, 2018); blue inverted triangles = depth to high (electrical) conductivity layer defined using maximum curvature of conductivity profile (HCL; Utada, 2019). (b) Same for the geochemically constrained optimal plate cooling model (T_p = 1333°C; z_p = 132 km; z_r = 2292 m), where black dotted line = plate thickness. (c) Optimal half-space cooling model overlain with additional seismological, geochemical and elastic thickness observations. Red squares = effective elastic thicknesses (Watts et al., 2013); blue rectangles = negative S-wave impedance contrast from ScS reverberations (Bagley and Revenaugh, 2008); green circles = negative S-wave impedance contrast from receiver functions (Kumar et al., 2011); blue stars = negative S-wave impedance contrast from SS precursors (Rychert and Shearer, 2011); light red triangle = negative S-wave impedance contrast from SH precursors to SS (Tonegawa and Helffrich, 2012); purple inverted triangles = depth to transition in Po/So wave propagation efficiency (Shito et al., 2015); yellow diamond = LAB inferred from deep seismic reflections (Stern et al., 2015); orange rectangle = estimate of mechanical boundary layer thickness from geochemical and geodynamic modelling of Hawaiian plume (Watson and McKenzie, 1991). (d) Same for optimal plate cooling model.

associated drop in amplitude of a seismic wave packet as it propagates through the Earth, and is composed of two parts (Romanowicz and Mitchell, 2015). *Extrinsic* attenuation is caused by elastic scattering and defocusing of the wave field into incoherent signals, which produces a drop in amplitude at points of observation, but conserves seismic energy throughout the whole Earth (Ricard et al., 2014). By contrast, *intrinsic* attenuation involves conversion of elastic energy into heat, and occurs in response to viscoelastic deformation, fluid flow and friction on grain boundaries.

Our theoretical and experimental understanding of attenuation at seismic frequencies and mantle grain sizes is less advanced than for seismic velocities (Faul and Jackson, 2005; Jackson and Faul, 2010; Abers et al., 2014; Kawakatsu and Utada, 2017). However, recent experiments on mantle minerals and rock analogues have greatly improved constraints on the pressure and temperature dependence of intrinsic attenuation at physical conditions appropriate to the upper mantle (Jackson and Faul, 2010; Faul and Jackson, 2015; Yamauchi and Takei, 2016; Takei, 2017). Therefore observations of intrinsic attenuation have the potential to yield useful insights into the structure of the lithosphere-asthenosphere system, especially when combined with seismic velocity information, since they have different sensitivities to temperature, grain size, water content and melt fraction (Abers et al., 2014). Moreover, under different physical conditions (e.g. pressure, temperature, composition, loading frequency, strain rate), there are multiple possible mechanisms that may operate to accommodate deformation at seismic frequencies, such as elastically accommodated grain boundary sliding, diffusionally accommodated grain boundary sliding, dislocation damping, and melt squirt (Jackson et al., 2004; Farla et al., 2012; Jackson et al., 2014; Yamauchi and Takei, 2016). As each mechanism is expected to give rise to a distinct relationship between seismic velocity and attenuation, constraints on this short-time-scale rheological behaviour may yield insights into long-term deformation mechanisms operating in the upper mantle (e.g. diffusion versus dislocation creep).

Unfortunately, intrinsic attenuation is notoriously difficult to extract from measured seismic waveform data, since extrinsic sources must be carefully accounted for and separated. Despite these difficulties, a number of global models of upper mantle attenuation have been produced, which tend to have lower spatial resolution than global seismic velocity models (Selby and Woodhouse, 2002; Gung and Romanowicz, 2004; Dalton et al., 2008; Adenis et al., 2017; Karaoğlu and Romanowicz, 2018). In oceanic regions, shear-wave attenuation and velocity are generally found to be anti-correlated, as expected if the dominant cause of variability is temperature and the associated anelasticity observed in laboratory experiments. However, it has also been observed that high attenuation can coincide with regions of increased shear-wave velocity at depths shallower than ~100 km, especially in the fast-moving Pacific plate (Dalton et al., 2009; Adenis et al., 2017). One potential explanation for this behaviour is that, at shallow depths, attenuation may be more sensitive than shear-wave velocity to the presence of hotspot-related melts, although imaging artifacts cannot yet be ruled out. Notwithstanding the seemingly ambiguous results for fast-moving plates, attenuation patterns generally match seismic velocity variations for slow-moving plates, and within the asthenosphere.

Seismic studies on a local scale have also been used to place important constraints on changes in attenuation signature between the lithosphere and asthenosphere. The asthenosphere as a whole seems to have relatively constant shear-wave attenuation, with similar values (~0.01) found both at shallow depth below 2–6 Ma lithosphere near the East Pacific Rise (25–100 km depth) and at greater depths beneath 150–160 Ma lithosphere in the Northwest Pacific Ocean (100–250 km; Yang et al., 2007; Booth et al., 2014). This simple result may break down at the ridge axis, with Eilon and Abers (2017) finding shear-wave attenuation values ≤ 0.04 beneath the Juan de Fuca and Gorda spreading centers, requiring the presence of volatile-bearing melt throughout the upper 180 km of the mantle. However, away from ridge

axes, one recent study observed that the change in attenuation as a function of seismic frequency is approximately linear in the lithosphere, whereas it appears to plateau at high frequencies within the asthenosphere (Takeuchi et al., 2017). Importantly, this result is consistent with recent experimental findings of an attenuation peak at seismic frequencies when temperatures approach the solidus (Takei et al., 2014; Yamauchi and Takei, 2016). The apparent agreement between experimental and seismic observations suggests that attenuation may now be sufficiently well understood to be used as a direct constraint in future models of the cooling of oceanic lithosphere.

2.3.3. Receiver functions and related passive seismic techniques

Several seismological techniques are very sensitive to sharp transitions in thermomechanical properties. Reverberations, precursors, and conversions can all be generated within the Earth when a seismic wavefield encounters boundaries with 5–10% velocity contrasts, and have been widely used to image the evolution of oceanic lithosphere. It is important to note that most simple lithospheric cooling models lose heat by conduction and so do not generate abrupt temperature transitions. Nevertheless, in the mantle, where dynamic processes operate, temperature is a first-order control on the onset of rheological transitions and melting, which may act to localise deformation processes and can lead to the development of compositional and/or mechanical boundaries. Therefore, these techniques may still provide important insights into the thermal evolution of oceanic lithosphere.

ScS reverberations are generated when shear waves undergo multiple reflections off a combination of shallow velocity contrasts and the core-mantle boundary. Their analysis provides constraints on both average seismic properties of the mantle and the depth to internal discontinuities. Following seismic migration of these phases, the resulting radial reflectivity profiles can be compared to synthetics to detect the presence and depth of major reflectors in the Earth's interior, from crust to core (Bagley and Revenaugh, 2008). SS precursors are shear waves that reflect off the underside of internal velocity contrasts, and therefore arrive slightly before the main SS phase that reflects off the Earth's surface. By stacking numerous SS precursor arrivals as a function of bounce point location and inverting the part of the waveforms preceding the main SS peak, the amplitude, depth and sharpness of seismic discontinuities at shallow mantle depths can be constrained (Rychert and Shearer, 2011). Finally, Sp and Ps phases represent teleseismic S- or P-waves converted to P- and S-waves at a particular impedance contrast within the mantle. These conversions are generally analysed using receiver functions, which are generated by deconvolving a seismogram to isolate solid Earth response signals from those related to seismic source and path. The resulting time series provides amplitude and polarity information for multiple phases, with arrival time delays between primary P- or S-waves and their converted waves constraining the depth and intervening velocity structure responsible for the conversions (Kawakatsu et al., 2009).

ScS reverberation studies find an apparently age-independent depth distribution, with velocity discontinuities consistently imaged between 70 km and 110 km depth, albeit in > 70 Ma lithosphere, where lateral temperature variations, and associated variations in plate thickness, are expected to be modest (Bagley and Revenaugh, 2008). Analyses of SS precursors have come to divergent conclusions. By modelling long-period (> 10 s) SS waveforms, Rychert and Shearer (2011) imaged an age-dependent discontinuity beneath normal oceanic crust, deepening from ~25 km at young ages to 90 km at ~75 Ma. However, after adapting a similar dataset to emphasise higher frequency components, Schmerr (2012) found a bimodal depth distribution of impedance contrasts, with one cluster at ~60 km, one at ~140 km, and no clear dependence on lithospheric age. By contrast, receiver function analysis of Ps and Sp conversions consistently find an age-dependent impedance jump in the Pacific and Philippine oceanic lithosphere deepening from 40 km to 90 km at ages between 10 Ma and 130 Ma (Kawakatsu et al., 2009; Kumar et al., 2011). This age-dependence has recently been

corroborated in the same region by analysis of Po- and So-waves that are generated by scattering of the seismic wavefield following interaction with horizontally elongated heterogeneities in the oceanic lithosphere (Shito et al., 2015). This latter study found that the maximum depth of scattering increased from 40 km to 80 km between 15 Ma and 130 Ma.

A commonly used thermal definition for the lithosphere-asthenosphere boundary (LAB) is the center of the thermal boundary layer, over which the geotherm transitions from a conductive gradient in the shallow mantle to an isentropic gradient in the convecting interior. As this transition is relatively smooth over a depth range of ~ 25–50 km, it is not clear that the seismologically detected discontinuities correspond with this thermally defined LAB (Richter and McKenzie, 1981). Nevertheless, recent studies on the anelastic behaviour of polycrystalline solids suggest that $\sim 5 - 10\%$ shear-wave velocity drops can occur over a $\sim 100°C$ window, as mantle temperature approaches the solidus (Yamauchi and Takei, 2016). This mechanism could potentially explain receiver function observations of age-dependent deepening of the LAB without the need to invoke the presence of melt at the interface (Fig. 3c and d). However, while certain observations appear to coincide with a thermally defined LAB, many studies also detect a large impedance contrast at depths of ~ 70 km that does not deepen with age (Rychert et al., 2012; Schmerr, 2012). Recent rock mechanic experiments have suggested that this boundary may represent a frozen-in discontinuity in radial anisotropy related to decompression melting at the ridge axis (Auer et al., 2015; Hansen et al., 2016). However, others have questioned the robustness of the layered radial anisotropy structure observed in surface wave studies and argue that the velocity drop across such an interface would be insufficient to explain receiver function observations (Rychert and Harmon, 2017). Instead, it has been suggested that the imaged age-independent discontinuity could be generated by trapped metasomatic melts that are frozen against the wet solidus during melting near the axis and subsequently transported with the plate (Pilet et al., 2011).

Although these passive seismic techniques can potentially provide higher resolution estimates of lithospheric thickness than surface wave dispersion methods (vertical resolution of ~ 5 km), ambiguity surrounding their interpretation and restricted spatial coverage limit their use for directly constraining models of plate cooling at present. However, if in the future, imaged impedance contrasts can be reliably tied to a particular thermal boundary within the lithosphere, receiver function analysis may provide important corroborating evidence for age-dependent lithospheric thickness changes inferred from other methodologies.

2.3.4. Controlled-source experiments

Rather than using naturally occurring earthquakes, controlled-source seismic experiments generate acoustic energy using either explosives or compressed air that is injected into the water column and subsequently expands. Two related techniques have been widely adopted by both academics and the hydrocarbon industry to image subsurface structures. The first uses the delay time of near-vertically propagating seismic energy that reflects off interfaces such as the sediment-basement contact, whilst the second additionally exploits horizontally propagating refracted energy.

Deep *seismic reflection* surveys can image impedance contrasts down to ~ 100 km, provided that sources are both sufficiently energetic and rich in low frequencies. Nevertheless, the frequency content of an active source is typically higher than that of an earthquake, meaning that this technique can provide vertical resolution of ~ 200 m in the mantle lithosphere, an order-of-magnitude improvement on the 2–10 km typical of teleseismic waves used to generate receiver functions (Steer et al., 1998; Fischer et al., 2010). In order to produce reflections, impedance contrasts must occur over depth ranges that are narrower than ~ 1 km and involve velocity changes of typically $> 6\%$ (Sheriff and Geldart, 1995).

As with receiver functions and related passive seismic techniques, it is unclear that deep reflections are imaging the thermal LAB since, given the modest temperature gradients at this depth, implausibly strong anelastic effects would be needed to generate a sufficiently strong and sharp velocity contrast. Indeed, by modelling changes in the reflection coefficient as a function of compositional variation, Stern et al. (2015) suggest that the reflections imaged by their experiment at 70–80 km are caused by a 10 km-thick layer of pooled melt and/or hydrous peridotite, possibly in the vicinity of the mechanical LAB (Fig. 3c and d). Currently, deep seismic reflection experiments are of limited use in constraining the thermal evolution of the oceanic lithosphere due to their restricted spatial coverage and ambiguity surrounding the interpretation of imaged reflections. Nevertheless, they provide important insights into internal lithospheric structure that other methods would not have sufficient vertical resolution to detect and, as more deep reflections are documented, these observations may help to determine the age-dependence of mechanical LAB depths.

Compared with seismic reflection surveys, *wide-angle refraction* experiments have slightly poorer vertical resolution but give direct information on the velocity structure of the subsurface, yielding better resolved constraints on the depth of particular interfaces. Refraction profiles are often acquired in conjunction with reflection surveys and require similarly large acoustic sources for imaging mantle depths. In addition, receivers used to record incoming seismic energy must be placed at a distance ≥ 4–5 times the depth of the velocity contrast of interest, in order to record its associated diving wave (Sheriff, 2002). These limitations mean that, away from spreading ridges where the boundary is relatively shallow, few refraction experiments have successfully imaged the interface between high-velocity lithosphere (~ 8.2 km s^{-1}) and lower velocity asthenosphere (~ 7.8 km s^{-1}; Mooney et al., 2002). Those experiments that do have sufficient depth penetration often detect a low-velocity zone at 80–100 km beneath oceanic regions, which appears to be independent of lithospheric age (Pavlenkova, 1996). One suggestion is that the uniform depth of this interface may reflect a reduction in P-wave velocity that occurs when the geotherm approaches or oversteps the solidus of volatile-bearing peridotite (~ 100 ppm of water and/or carbon dioxide; Thybo, 2006). It is important to note that active source experiments are using P-wave energy, which is significantly less sensitive to temperature than shear-wave velocities (Schutt and Lesher, 2006). Consequently, existing refraction experiments appear to be less useful for directly constraining thermal models of oceanic lithosphere, but they do place bounds on the thickness and bulk P-wave velocities of different sub-surface layers, and have been particularly helpful for understanding the thickness and internal structure of oceanic crust (White et al., 1992).

2.3.5. Earthquake depths

The maximum depth of earthquakes within oceanic lithosphere places important bounds on the changing depth of the brittle-ductile transition. In the latest compilations, outer rise and intraplate earthquakes in young lithosphere (< 5 Ma) extend to maximum depths of 10 km, systematically increasing to ~ 45 km by 90 Ma, and subsequently flattening off at older ages (Craig et al., 2014; Fig. 3a and b). Rock mechanics experiments suggest that the switch from velocity-weakening to velocity-strengthening behaviour in olivine, which is related to the brittle-ductile transition, may be strongly dependent on temperature, grain size, water content, strain rate and total accumulated strain (Goetze, 1978; Warren and Hirth, 2006; Boettcher et al., 2007; King and Marone, 2012; Hansen et al., 2013, 2019). Some recent experimental studies have cited 600 ± 50°C as the critical isotherm corresponding to the seismic-aseismic transition, but this estimate does not fully account for representative ranges of key parameters in the upper mantle (i.e. dry to water-saturated conditions; strain rate $=10^{-15} - 10^{-12}$ s^{-1}; grain size $=0.1$–10 mm; accumulated strain $=0$–2%), nor does it reflect additional uncertainties in activation enthalpy, Peierl's stress and extrapolation of laboratory results to

geological strain rates (cf. Boettcher et al., 2007). Accounting for these sources of uncertainty, the brittle-ductile transition may coincide with any temperature between 500˚C and 800˚C (King and Marone, 2012; Richards et al., 2018). This larger, condition-dependent range is more consistent with independent pressure-temperature estimates obtained from geothermometry on dredged gabbro and peridotite mylonites, which suggest temperatures at the brittle-ductile transition of 600–800˚C (Jaroslow et al., 1996; Hansen et al., 2013).

Irrespective of the exact value of the limiting temperature for brittle behaviour, since changes in temperature dominate the evolution of oceanic lithosphere, a successful thermal model should be consistent with the deepening of maximum earthquake depths as a function of age. The apparent flattening of maximum depths beyond ~80 Ma may be more consistent with plate models (McKenzie et al., 2005; Grose and Afonso, 2013; Richards et al., 2018). However, their patchy coverage and sensitivity to other parameters means that intraplate earthquakes provide only a weak constraint on lithospheric cooling models, particularly since isotherms predicted by half-space and plate cooling models in the range 500–800˚C are very similar. Nevertheless, if accurate models of the temperature structure in seismogenic regions can be combined with bounds on water content, grain size, strain rate and accumulated strain, the depth extent of intra-oceanic seismic events will be critical for constraining the rheological properties of oceanic lithosphere.

2.4. Elastic thickness

The elastic thickness of the lithosphere is determined by its ability to support elastic stresses on geological timescales, and hence its rheology. Given the temperature dependence of most deformation mechanisms, elastic thickness is expected to increase with age as the lithosphere cools. Estimates derived from flexural modelling at seamounts and ocean trenches largely bear this out, following the depth to the 300–600˚C isotherm as a function of lithospheric age at time of loading (Fig. 3c and d; Watts et al., 2013; Hunter and Watts, 2016). However, it should be noted that several other studies assessing elastic thickness at ocean trenches have found no obvious age relationship (Bry and White, 2007; Craig and Copley, 2014). Moreover, there is considerable scatter in elastic thickness estimates obtained at sites with identical lithospheric ages, some of which could potentially be attributed to strain-hardening effects. Recent low-temperature rheological experiments in the regime of permanent, non-recoverable deformation (plasticity) suggest that, as plastic strain accumulates up to 2% beyond the initial yield point, lithospheric strength increases (Hansen et al., 2019). This observation may explain why comparatively low elastic thicknesses are recovered at medium-sized seamounts, where the total strain may be < 2%, whereas in environments with more extreme strain, such as oceanic trenches, higher elastic thicknesses are often recorded.

As with earthquake depths, due to the strong influence of other properties on effective elastic thickness, these estimates provide only weak constraints on thermal models. Nevertheless, if the local thermal structure can be constrained by other means, elastic thickness can be used to infer rheological properties, such as the maximum temperature at which long-term strength can be sustained.

2.5. Curie depth

The Curie temperature refers to the temperature at which a material loses its permanent magnetism, and is thought to coincide with the ~550˚C isotherm in oceanic crust and lithosphere, assuming that magnetite is the dominant magnetic mineral (Mayhew, 1982). The three-dimensional spectral properties of magnetic anomalies can be used to estimate the depth of this transition, thereby potentially placing constraints on the thermal evolution of oceanic lithosphere. Recent inversion algorithms applied to satellite-derived EMAG2 anomalies

have found evidence for an age-dependent deepening of the Curie depth from ~15 km near the ridge axis to ~30 km at old ages (~150 Ma; Li et al., 2017).

These inversion methods are not straightforward and are known to underestimate Curie depths (Li and Wang, 2018). Since shorter wavelength information quickly attenuates with increasing observation distance, deep interfaces produce long-wavelength signals within a narrow range of low wavenumbers. However, to maintain computational stability, magnetic data must be windowed in relatively broad wavenumber bands, which dilutes deeper signals with shallow structure. Linking Curie depths to a particular isotherm is further complicated by the solid solution between magnetite (Fe_3O_4) and titanium-bearing ulvöspinel (Fe_2TiO_4). The compositional heterogeneity of the mantle is poorly constrained, but increasing the proportion of ulvöspinel from 0 to 100% will cause the Curie temperature to reduce from 550˚C to −100˚C (Lattard et al., 2006). Finally, the principal minerals comprising mantle peridotite generally have low magnetic susceptibility unless they have been extensively altered to form serpentinite. It has therefore also been suggested that variations in Curie depth may actually reflect the depth of hydrothermal fluid penetration (Li et al., 2013).

Thus, despite the apparent age-progressive deepening observed in global compilations, it remains unclear that Curie depth can be reliably retrieved by existing magnetic measurements, and whether its variation primarily reflects changes in temperature structure or compositional effects. These technical and interpretational difficulties currently limit our ability to test cooling model outputs using these data. However, if thermal properties can be independently constrained, Curie depth may be used as a proxy for mineralogical variations within oceanic lithosphere.

2.6. Magnetotelluric studies

Although the application of magnetotelluric inverse modelling is in its infancy compared to seismic tomography, much like seismic velocity, electrical conductivity is highly sensitive to temperature. Electrical conductivity is also strongly dependent on melt and water content, making magnetotelluric surveys especially effective for detecting fluid pathways and melt lenses (Shankland and Waff, 1977). Magnetotelluric studies of oceanic upper mantle generally obtain high conductivities in the crust and asthenosphere, bounding a low conductivity lithosphere (Sarafian et al., 2015). High values in the crust reflect the higher conductivity of basalt and elevated water content resulting from hydrothermal circulation, whereas low conductivities observed in the lithosphere are consistent with its relatively cool temperature and dehydrated state (Yoshino and Katsura, 2013). The origin of high conductivities in the asthenosphere remain controversial, with some models suggesting that high temperature alone is sufficient, while others invoke the additional presence of variable quantities of water and melt (Sarafian et al., 2015; Selway and O'Donnell, 2019).

Despite these disagreements, it is generally accepted that temperature is the dominant driver of upper mantle conductivity variations (Utada, 2019). As a result, the depth of the electrically defined LAB — estimated by calculating the point of maximum curvature in a given electrical conductivity profile — can be directly linked to the thermal evolution of the oceanic lithosphere (Kawakatsu and Utada, 2017). For example, after removing measurements from magnetotelluric arrays near plate boundaries that are likely affected by strong lateral variations in conductivity, Utada (2019) suggested that electrical LAB depths flatten at old ages in a manner consistent with the plate cooling model (Fig. 3a and b). This study also found a linear relationship between mean bathymetry and the electrical LAB depth, which they believe is consistent with dynamic rejuvenation of the base of the lithosphere.

Although magnetotelluric inverse modelling, like surface wave tomography, can image structure across the whole depth range of the
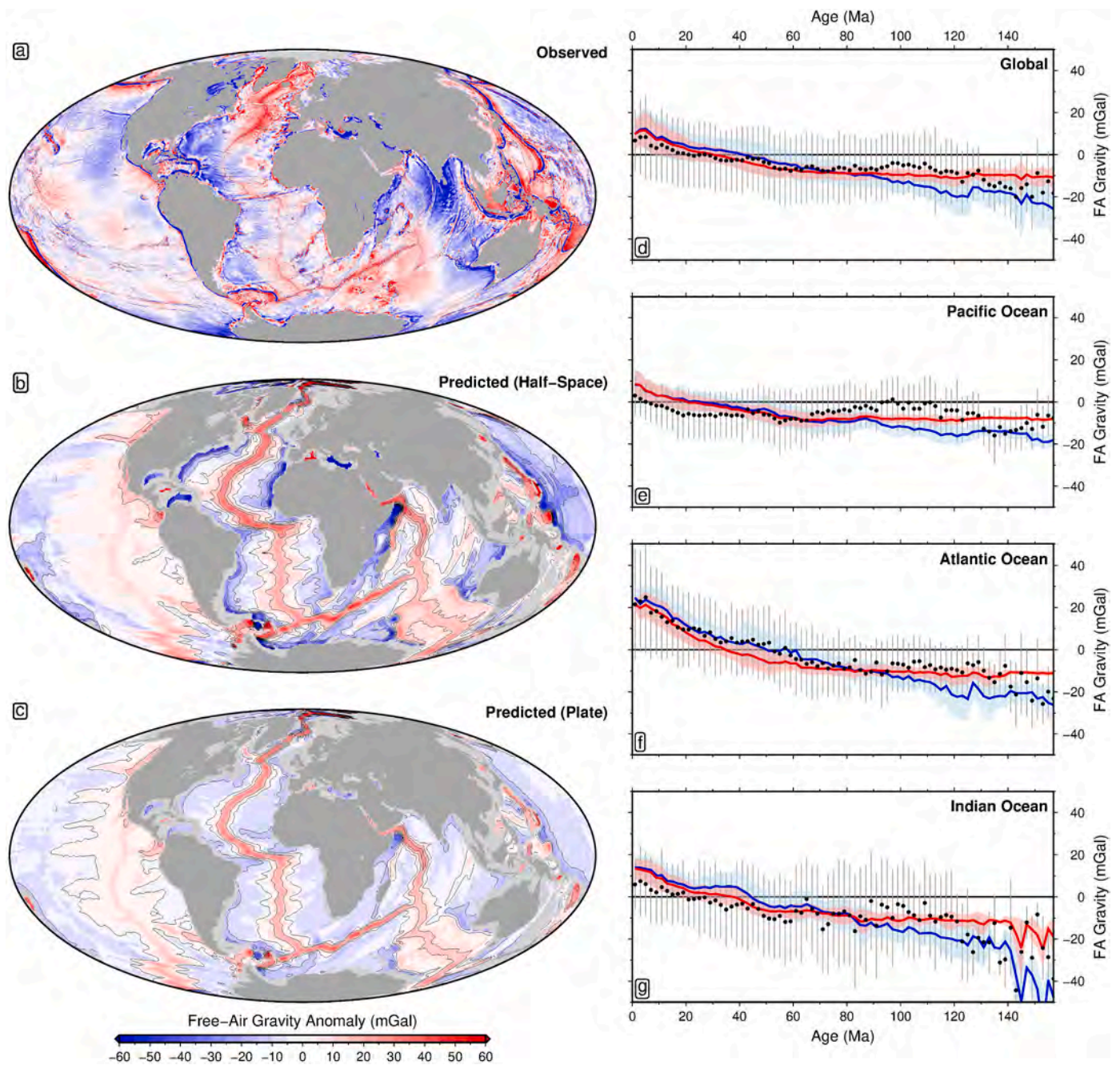
Fig. 4. Inter-basin comparison of observed and predicted free-air gravity anomalies. Predictions are calculated using method outlined in Appendix E. (a) Measured oceanic free-air (FA) gravity anomalies (Sandwell et al., 2014). (b) Isostatic anomalies predicted from optimal geochemically constrained half-space cooling model ($T_p = 1333°C$; $z_r = 1906$ m); contour interval = 10 mGal. (c) Same for plate cooling model ($T_p = 1333°C$; $z_p = 132$ km; $z_r = 2292$ m). (d) Blue line/envelope = mean and standard deviation of anomalies predicted by half-space model as a function of age, binned globally in 2 Ma increments and excluding regions of anomalous oceanic crust defined using polygons of Hoggard et al. (2017); red line/envelope = same for plate cooling model; circles with vertical bars = observed anomalies with 2σ errors. (e) Same for subset of data in the Pacific Ocean. (f) Same for Atlantic Ocean. (g) Same for Indian Ocean.

lithosphere-asthenosphere system, far fewer oceanic studies have been carried out, and those that have tend to be on more localised scales. As a result, while magnetotelluric experiments currently help to confirm the validity of upper mantle thermochemical structure inferred from other methods, more studies are required before it can be reliably used as an independent constraint on the average behaviour of the lithosphere-asthenosphere system. Nevertheless, the heightened sensitivity of magnetotelluric studies to the presence of melt and water provides important insights on the nature of discontinuities imaged by receiver functions, as well as the melt fraction and water content of the asthenosphere.

2.7. Geochemical constraints

Along the Earth's spreading ridge system, covariation of mid-ocean ridge basalt (MORB) composition with variations in axial ridge depth and shear-wave velocity anomalies suggest that the geochemistry of oceanic crust provides useful insights into the thermal state of the upper mantle (Klein and Langmuir, 1987; Dalton et al., 2014). In particular, MORB geochemistry can give an independent assessment of *mantle potential temperature* (i.e. the temperature that the solid, convecting asthenospheric mantle would have if it could decompress to the surface without undergoing melting). Geochemical estimates of this critical

thermophysical parameter vary according to petrological technique, with ranges spanning 1280–1400°C (Herzberg et al., 2007), 1314–1464°C (Dalton et al., 2014) and 1286–1362°C (Matthews et al., 2016). The thickness of oceanic crust can also be used to infer the average temperature of the mantle through its relationship with melt fraction (White et al., 1992). An average crustal thickness of 6.9 ± 2.2 km has been inferred from global compilations of seismic reflection and refraction data (Hoggard et al., 2017). Adopting the anhydrous peridotite solidus of Katz et al. (2003) and applying the decompression melting parameterisation of Shorttle et al. (2014), this thickness range corresponds to a mantle potential temperature of 1331 ± 35°C, which is consistent with the 1315°C value obtained by McKenzie et al. (2005) using the melting model of McKenzie and Bickle (1988). Finally, mineral physics constraints on temperatures at the 410 km discontinuity and adiabatic gradients in the upper mantle provide an estimate of 1337 ± 35°C (Katsura et al., 2010). Taken together, these geochemical and petrological constraints imply an ambient mantle potential temperature of 1340 ± 60°C, and thermal models that invoke axial temperatures outside this range should therefore be used with caution (cf. Stein and Stein, 1992).

In addition to potential temperature, ocean island basalt geochemistry at magmatic hotspots can be inverted to infer the local depth to the top of the melting zone. This depth is widely believed to be controlled by the mechanical boundary layer (MBL), beyond which further upwelling and decompression melting is inhibited. By modelling rare earth element (REE) signatures of Hawaiian lavas, Watson and McKenzie (1991) obtained a depth of 72 km beneath this ~95 Ma seafloor (Fig. 3c and d). Similarly, Ellam (1992) demonstrated that the change in melting source from spinel to garnet lherzolite has profound effects on the REE distributions of erupted magmas, potentially providing a means for determining changes in the thickness of the oceanic MBL if the melting zone transitions between different stability fields (Putirka, 1999). Geochemical studies suggest that the mechanical boundary layer thickness is probably age-dependent and tracks close to the 1100°C isotherm, potentially adding a useful observation to test models of oceanic temperature structure (Niu et al., 2011). However, these inferences are tentative due to relatively patchy coverage of geochemical observations, coupled with rheological uncertainties surrounding the temperature at which lithospheric mantle becomes sufficiently rigid to inhibit further upwelling. Furthermore, plumes may locally modify thermal structure of the lithosphere, particularly for slow-moving plates, making ocean island basalt melting zones unrepresentative of 'normal' MBL depths at these ages (Courtney and White, 1986; Sleep, 1990). As a result, while geochemical studies provide some of the most direct measurements of mantle temperatures, their sparsity and inherent assumptions limit their utility for constraining cooling models.

2.8. Gravity anomalies

Cooling, densification and subsidence of oceanic lithosphere produces spreading-geometry-dependent spatiotemporal variations in free-air gravity anomalies, which in theory can be used to constrain thermal evolution (Lambeck, 1972; Crosby et al., 2006). However, unlike subsidence data, where cooling dominates the signal, its expression in gravity is locally dwarfed by larger signals related to flexural loading and mantle convection (Fig. 4a). Observed geoid anomalies suffer from the same problem and, while some studies that attempt to account for these issues by using geoid slopes across fracture zones suggest that best-fitting cooling models can be discriminated, others disagree (Hager, 1983; Richardson et al., 1995; DeLaughter et al., 1999; Cadio and Korenaga, 2012). Therefore, although cooling model predictions must be consistent with observations, these datasets are generally too noisy to tightly constrain model parameters such as plate thickness or mantle potential temperature (Fig. 4b–f; Richards et al., 2018).

Despite these issues, regional variations in gravity-to-topography

spectral ratios (known as the *admittance, Z*) can be used at plume swell locations to crudely estimate the midpoint depth of density anomalies supporting surface deflections. Based on the ~2000 km wavelength of the Hawaiian swell and an observed admittance of ~30 mGal km^{-1}, Crosby and McKenzie (2009) estimated that the mass compensating the anomalous bathymetry must have a midpoint depth of ~100 km. This value is consistent with other local estimates of plate thickness and asthenospheric depth, suggesting a mechanical boundary layer thickness of around 80 km (corresponding to an isotherm between 1000 and 1100°C). Moreover, since a similar admittance value is observed globally throughout the oceans, the implication is that, at relatively short wavelengths (~1000–2000 km), active mantle flow does not extend significantly shallower than 100 km. This inference is consistent with the suggestion that dehydration of fertile peridotite during the initial stages of melting may increase its viscosity above ~100 km sufficiently to inhibit convection (Afonso et al., 2008b).

3. Present understanding of the thermal structure of oceanic lithosphere

Over the past decades, augmentation of existing measurements, the application of innovative techniques to collect new observational datasets, and improved experimental constraints on upper mantle material properties have enhanced our understanding of the oceanic lithosphere-asthenosphere system. The challenge for geophysicists is to devise a unified model that can successfully explain this wealth of information while accounting for the often very different sensitivities of individual datasets (Table 1). Although some inconsistencies remain, recent advances have generally helped to reconcile previously conflicting findings and are summarised here.

3.1. Effects of temperature, pressure and composition on thermal parameters

The key material properties determining the rate of conductive heat loss and, therefore, thermal evolution of oceanic lithosphere are conductivity, heat capacity and the temperature-dependence of density, known as *thermal expansivity*. When the earliest lithospheric cooling models were developed, experimental constraints on these properties, especially their variation as a function of pressure and temperature,

Table 1
Summary of different constraints on oceanic lithospheric structure. Coverage refers to the current geographical extent of measurements; depth extent is the depth range over which observations are typically made; physical properties that each observation is sensitive to include T = temperature; ρ = density; X = composition; η = rheology (viscosity); ϕ = melt fraction; C_w = water content; fO_2 = oxygen fugacity; H/M/L = high/medium/low sensitivity.

Data type	Coverage	Depth extent	Property (sensitivity)
Subsidence	Global	Surficial	T(H), ρ(H), X(H)
Heat flow	Global	Surficial	T(H), X(H)
Surface wave dispersion	Global	~400 km	T(H), X(M), η(M), ϕ(M)
Attenuation	Global	Whole mantle	T(H), X(M), η(H), ϕ(H)
Receiver functions	Regional	Whole mantle	T(L), X(H), ϕ(H), C_w(M)
Controlled-source seismology	Regional	~100 km	X(H), ϕ(H), C_w(M)
Earthquake depths	Regional	~50 km	T(M), η(H)
Elastic thickness	Global	~150 km	T(M), η(H)
Curie depth	Global	~70 km	T(H), X(H)
Magnetotelluric surveys	Regional	~200 km	T(H), X(H), ϕ(H), C_w(H), fO_2(H)
Basalt geochemistry	Regional	Surficial	T(H), X(H), ϕ(H), C_w(H), fO_2(H)
Gravity/geoid anomalies	Global	Whole mantle	T(H), ρ(H), X(H)
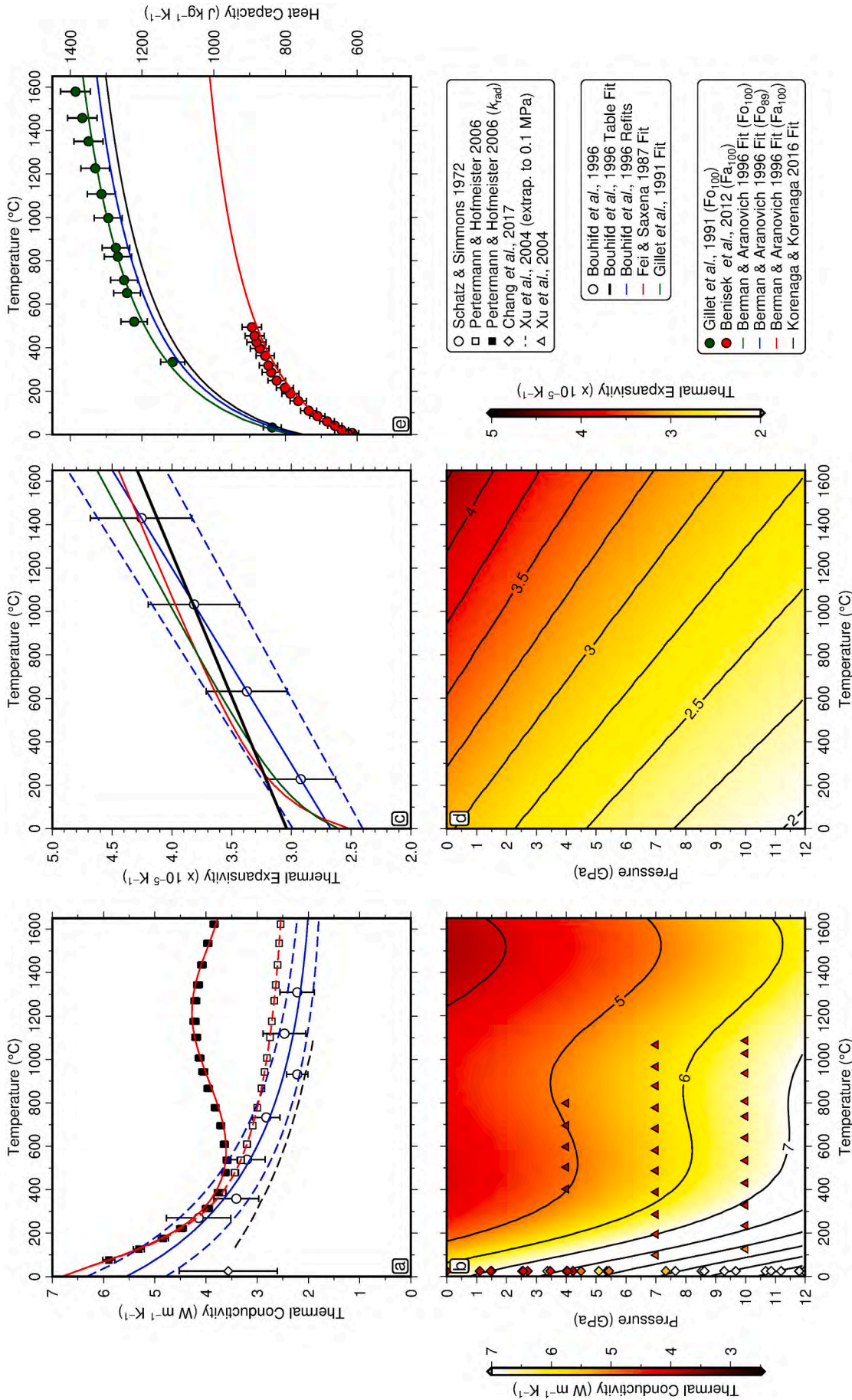
Fig. 5. Temperature- and pressure-dependence of conductivity, expansivity and heat capacity. (a) Thermal conductivity of forsterite (Mg$_2$SiO$_4$) plotted as a function of temperature at constant pressure of 0.1 MPa. Circles with ± 1σ error bars fitted with solid/dashed blue lines = lattice conductivity measurements from Schatz and Simmons (1972); black/white squares with dashed/solid red lines = lattice conductivity measurements from Pertermann and Hofmeister (2006) excluding/including additional contribution from 5 mm radiative conductivity measurements of Hofmeister (2005); diamond with error bar = lattice conductivity measurement for anhydrous forsterite from Chang et al. (2017); dashed black line = lattice conductivity parameterisation of Xu et al. (2004) extrapolated to 0.1 MPa. (b) Thermal conductivity (lattice plus radiative) of forsterite as a function of pressure and temperature based on lattice conductivities of Pertermann and Hofmeister (2006) and Hofmeister (2007). Diamonds = Chang et al. (2017) lattice conductivities; triangles = Xu et al. (2004) lattice conductivities. The additional contribution of radiative conductivity from Hofmeister (2005), for a grain size of 0.5 cm, has been added in each case. (c) Thermal expansivity of forsterite plotted as function of temperature at constant pressure of 0.1 MPa. Circles with ± 1σ error bars fitted with solid/dashed blue lines = measurements from Bouhifd et al. (1996); black line = Bouhifd et al. (1996) original parameterisation of fit to data; red/green lines = relationships used by Fei and Saxena (1987) and Gillet et al. (1991), respectively. (d) Thermal expansivity of forsterite as a function of pressure and temperature based upon parameterisation of Berman (1988) fitted using parameterisation of Berman (1988) fitted using circles with green line = measurements for forsterite from Gillet et al. (1991) fitted using parameterisation of Berman (1988); red circles with red line = measurements for fayalite (Fe$_2$SiO$_4$) from Benisek et al. (2012) fitted using parameterisation of Berman (1988) assuming olivine is composed of 89% forsterite and 11% fayalite; black line = parameterisation described by Eq. (2) of Korenaga and Korenaga (2016). Note that pressure dependence of olivine heat capacity over the relevant range of plate thicknesses is negligible (Hofmeister, 2007). Figure adapted from Richards et al. (2018). See Appendix C for details of calculations.

were relatively scarce. As a result, they were sometimes left free to vary when fitting model predictions to observations (e.g. Parsons and Sclater, 1977; Stein and Stein, 1992). However, over the intervening years, a number of experimental studies have established the pressure and temperature dependence of thermal conductivity, expansivity and heat capacity for olivine and other key minerals (Fig. 5; Fei and Saxena, 1987; Gillet et al., 1991; Berman and Aranovich, 1996; Bouhifd et al., 1996; Hofmeister, 1999; Xu et al., 2004; Hofmeister, 2005; Pertermann and Hofmeister, 2006; Hofmeister, 2007; Hofmeister and Pertermann, 2008; Benisek et al., 2012; Chang et al., 2017). These updates have steadily been incorporated into newer generations of lithospheric cooling models.

Studies incorporating the temperature dependence of thermal properties of olivine into cooling models find that, although a similar quality of fit to observed subsidence and heat flow data can be obtained, the inferred thermal structure at depth can be significantly different (Denlinger, 1992; McKenzie et al., 2005). In particular, the parameter known as *lattice conductivity*, associated with heat transport through the crystal lattice by elastic vibrations (phonons), strongly decreases with increasing temperature (Fig. 5a; Schatz and Simmons, 1972; Pertermann and Hofmeister, 2006). This inverse relationship dominates changes to the predicted thermal evolution, producing a widening of temperature isotherms at shallow depths and a narrowing of their depth separation in the deeper, warmer sections of the lithosphere ($T > 800$°C).

In Figs. 6b and 7b, we illustrate this effect in both half-space and plate cooling models. We adopt a temperature-dependent olivine conductivity law that also includes the additional contribution of *radiative conductivity*, associated with heat transport through the crystal lattice by photons, which is thought to become increasingly significant at higher temperatures (Hofmeister, 2005; Pertermann and Hofmeister, 2006). Arguments based upon the thickness of oceanic crust and the geochemical composition of mid-ocean ridge basalts suggest an ambient mantle potential temperature of $T_p = 1333$°C (Section 2.7). Fixing this value and simultaneously fitting heat flow and subsidence data illustrates that isotherms separate as anticipated. In the case of the plate model, we find a larger optimal plate thickness is required in comparison to models with constant conductivity (~ 126 km versus $z_p \sim 93$ km; Fig. 7b versus Fig. 7a). This result contrasts with that of McKenzie et al. (2005), primarily due to our use of an updated temperature-dependent conductivity parameterisation.

More recently, parameterisations for the pressure dependence of lattice conductivity and thermal expansivity have also been developed (Fig. 5b and d; Hofmeister, 2007; Grose and Afonso, 2013; Korenaga and Korenaga, 2016). Lattice conductivity increases as a function of pressure which, when combined with the increase in radiative contributions at higher temperature, largely cancels out the decreasing separation between high temperature isotherms identified in purely temperature-dependent models (Figs. 6c and 7c; Richards et al., 2018). The net result is that pressure- and temperature-dependent models require lower optimal potential temperatures to fit heat flow data. Moreover, at higher pressures, thermal expansivity reduces and so density varies less strongly as a function of temperature. In plate cooling models, this necessitates a greater optimal plate thickness in order to provide sufficient vertical contraction to match observed subsidence trends (Fig. 7c versus Fig. 7b).

Finally, as initially pointed out by Grose and Afonso (2013), the thermal properties of lithospheric mantle are probably well-described by those of olivine, which makes up > 75% of its mineralogy. However, olivine is only a minor phase in oceanic crust (~ 5%) and the high abundance of plagioclase will lead to significantly lower thermal conductivity and density values. Adopting representative thermal properties based on an appropriate averaging of clinopyroxene, olivine and plagioclase components, the inclusion of a 7 km-thick crustal layer insulates the underlying mantle and has a dramatic impact on thermal evolution of the lithosphere. When left free to vary, the potential
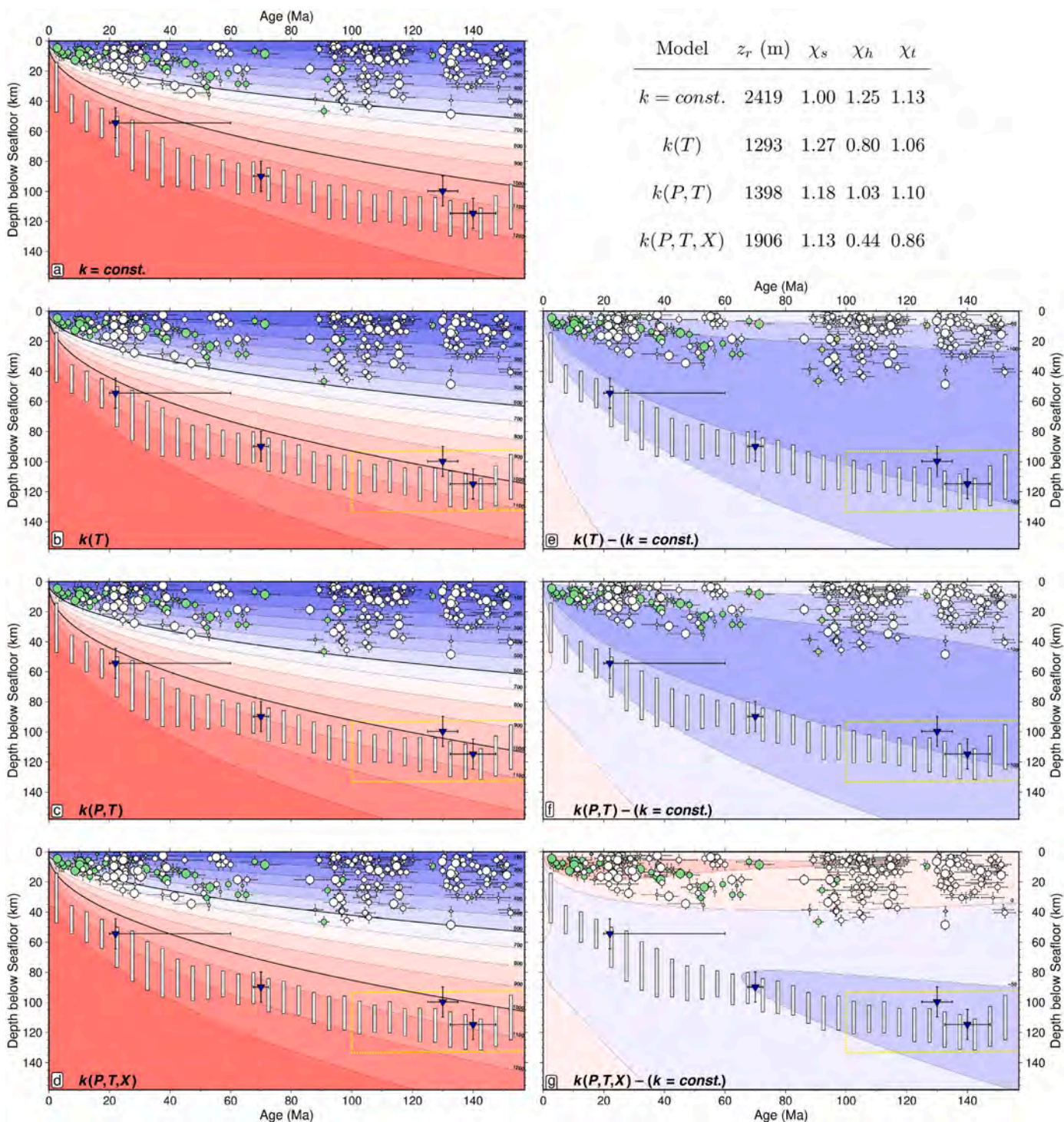
temperature required to simultaneously fit heat flow and subsidence data becomes significantly more consistent with geochemical constraints, while the slower rate of cooling provides better fits to subsidence data and seismological observations of the LAB (e.g. Figs. 6d and 7d; Burgos et al., 2014; Steinberger and Becker, 2018). Notably, plate models generally achieve better fits in comparison to half-space cooling. Furthermore, in the case of plate models, incorporation of these increasingly physically realistic thermal properties results in more consistent optimal parameters required by individual fits to either subsidence or heat flow observations (Richards et al., 2018).

Despite the apparent success of cooling models that incorporate a compositionally distinct oceanic crust alongside pressure- and temperature-dependent thermal properties, there remains significant uncertainty for certain thermal parameters. Thermal expansivity and heat capacity of olivine are believed to be accurate to ~ 10% and ~ 3%, respectively, based on experimental uncertainties and the level of agreement between different studies (Fig. 5c and e). Accounting for these variations causes only modest changes in optimal model parameters, with variations in inferred mantle potential temperature of ± 13°C, differences in optimal zero-age ridge depth of ± 0.2 km, and changes in best-fit plate thickness of ± 2.5 km.

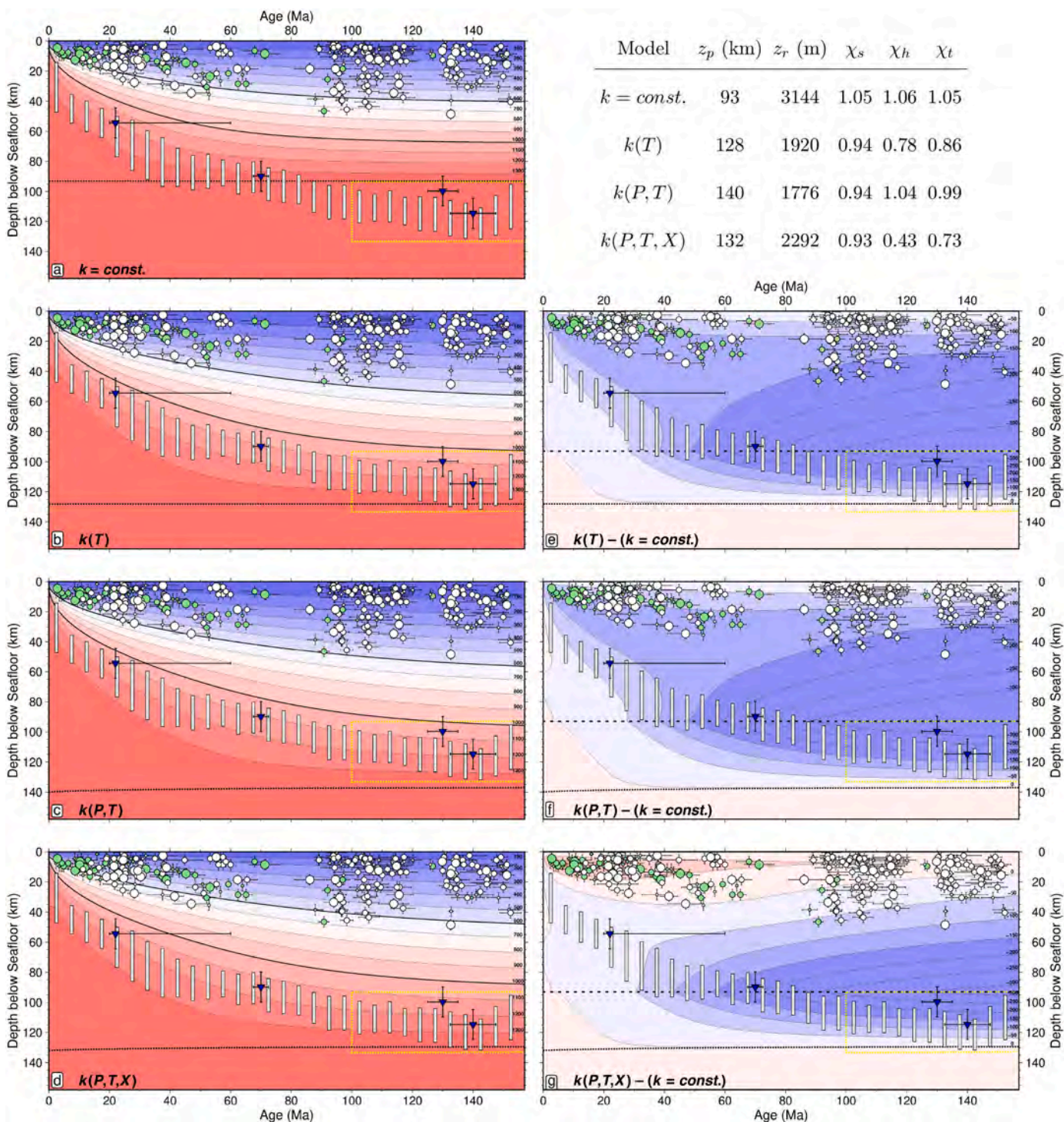However, estimates of olivine lattice conductivity at room pressure and temperature are substantially more variable (3.5–7.0 W m^{-2}), which is believed to be caused by anisotropy of the crystal lattice and methodological differences, such as laser-flash versus contact measurement techniques (Fig. 5a; Gibert et al., 2003; Pertermann and Hofmeister, 2006). As surface heat flow is highly sensitive to conductivity close to the seafloor, uncertainty in conductivity at low temperature leads to a wide range of suitable model parameters. Incorporating this range for the lattice conductivity introduces variation in the optimal mantle potential temperature of ± 115°C, and plate thickness of ± 5 km. Furthermore, there remains significant debate surrounding the magnitude of the radiative component of thermal conductivity and how it may vary as a function of pressure and temperature (Shankland et al., 1979; Hofmeister, 2005; Grose and Afonso, 2019b). Therefore, tighter experimental constraints on thermal conductivity are likely to provide the largest reduction in the range of parameters obtained by lithospheric cooling models.

Some previous attempts to model lithospheric cooling have also found that, when thermal expansivity is reduced by ~ 10–20% compared to experimental predictions for olivine, an improved fit to subsidence observations can be obtained (Grose and Afonso, 2013). This deficit has been suggested to result from incomplete thermal relaxation, whereby horizontal thermal contraction of the lithosphere is resisted by intraplate stresses, possibly leading to the development of deep tension cracks (Pollack, 1980; Korenaga, 2007). However, this hypothesis is challenged by evidence indicating that the lithosphere undergoes full thermal contraction in both horizontal and vertical directions. These observations include a change in intraplate earthquake focal mechanisms from thrust to normal with depth, and systematic variation in transform fault azimuths away from predictions for a perfectly rigid, non-horizontally shrinking plate (Wiens and Stein, 1983; Huang et al., 2015; Mishra and Gordon, 2016). It has also been proposed that effective thermal expansivity may be lower than predicted for pure olivine due to the presence of other mineral phases in the oceanic upper mantle (~ 20% orthopyroxene, ~ 15% clinopyroxene; Grose and Afonso, 2013). However, experimental studies on orthoenstatite suggest that orthopyroxene, the second most abundant phase, has very similar expansivity to olivine (Jackson et al., 2003).

We can test the effects of reducing expansivity on optimal values of the plate model parameters. For a ~ 10% reduction, fitting subsidence data alone gives a ~ 100°C higher best-fitting mantle potential temperature, in closer agreement with the equivalent value obtained for heat flow. However, the lowest combined misfit to both subsidence and heat flow data (χ_t) only reduces by ~ 0.5% compared to the model with unadjusted expansivity values. Thus, in contrast to some previous

Model	z_r (m)	χ_s	χ_h	χ_t
$k = const.$	2419	1.00	1.25	1.13
$k(T)$	1293	1.27	0.80	1.06
$k(P,T)$	1398	1.18	1.03	1.10
$k(P,T,X)$	1906	1.13	0.44	0.86

Fig. 6. Effect of including temperature, pressure, and composition-dependence of thermal properties in half-space cooling models. All models are jointly fitted to subsidence and heat flow data. The initial temperature profile is derived using the $T_p = 1333°C$ isentrope and decompression melting parameterisation for a dry aluminous lherzolite, which is compatible with the thickness and geochemistry of mid-ocean ridge basalts (Section 2.7; Katz et al., 2003; Shorttle et al., 2014). (a) Temperature evolution when thermal properties are constant and fixed to the values from Parsons and Sclater (1977). Symbols are selected geophysical observations from Fig. 3a and b. (b) Same for the purely temperature-dependent half-space model using parameterisations from Korenaga and Korenaga (2016) for conductivity, expansivity and heat capacity. (c) Same for pressure and temperature-dependent model using parameterisations from Korenaga and Korenaga (2016). (d) Same for pressure and temperature-dependent model, including a 7 km-thick oceanic crustal layer and using parameterisations from Korenaga and Korenaga (2016). (e) Difference in temperature evolution between purely temperature-dependent model and version with constant properties. (f) Same for pressure and temperature-dependent model. (g) Same for model including a 7 km-thick oceanic crustal layer. Table summarises model fitting results. z_r = optimal zero-age ridge depth; χ_s and χ_h = misfit to subsidence and heat flow data, respectively; χ_t = combined misfit. See Appendices A–D for details of thermal modelling, misfit calculations and thermal property parameterisations.

Model	z_p (km)	z_r (m)	χ_s	χ_h	χ_t
$k = const.$	93	3144	1.05	1.06	1.05
$k(T)$	128	1920	0.94	0.78	0.86
$k(P,T)$	140	1776	0.94	1.04	0.99
$k(P,T,X)$	132	2292	0.93	0.43	0.73

Fig. 7. Effect of including temperature, pressure, and composition-dependence of thermal properties in plate cooling models. All models are jointly fitted to subsidence and heat flow data. The initial temperature profile is derived using the $T_p = 1333°C$ isentrope and decompression melting parameterisation for a dry aluminous lherzolite, which is compatible with the thickness and geochemistry of mid-ocean ridge basalts (Section 2.7; Katz et al., 2003; Shortle et al., 2014). (a) Temperature evolution when thermal properties are constant and fixed to the values from Parsons and Sclater (1977). Symbols are selected geophysical observations from Fig. 3a and b; horizontal dotted black line = optimal plate thickness. (b) Same for the purely temperature-dependent plate model using parameterisations from Korenaga and Korenaga (2016) for conductivity, expansivity and heat capacity (cf. McKenzie et al., 2005). (c) Same for pressure and temperature-dependent model using parameterisations from Korenaga and Korenaga (2016). (d) Same for pressure and temperature-dependent model, including a 7 km-thick oceanic crustal layer and using parameterisations from Korenaga and Korenaga (2016). (e) Difference in temperature evolution between purely temperature-dependent model and version with constant properties. Horizontal dashed line = optimal plate thickness for the model with constant thermal properties. (f) Same for pressure and temperature-dependent model. (g) Same for model including a 7 km-thick oceanic crustal layer. Table summarises model fitting results. z_p = optimal plate thickness; z_r = optimal zero-age ridge depth; χ_s and χ_h = misfit to subsidence and heat flow data, respectively; χ_t = combined misfit. See Appendices A–D for details of thermal modelling, misfit calculations and thermal property parameterisations.
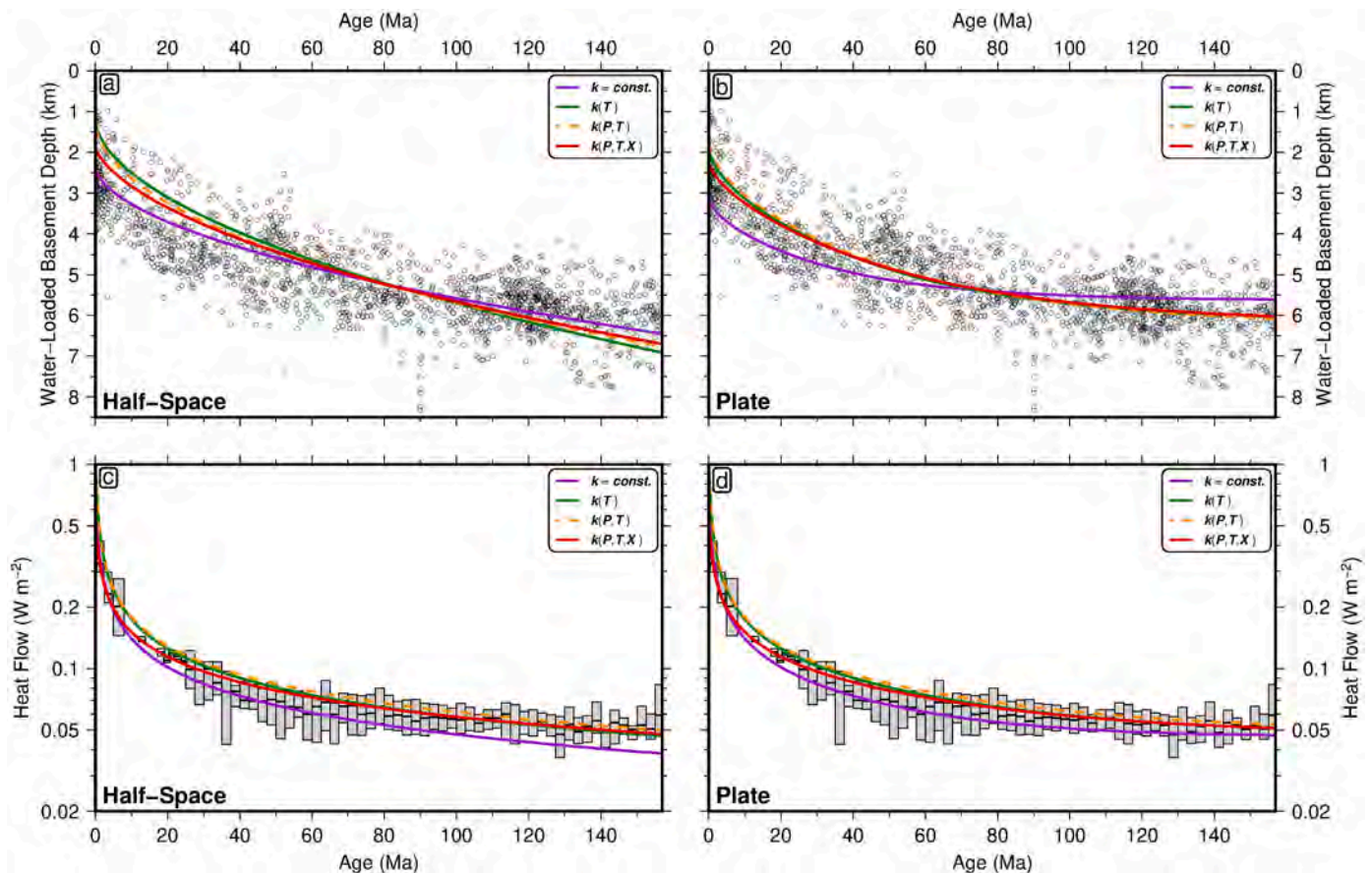
Fig. 8. Effect of including temperature, pressure, and composition dependence of thermal properties on subsidence and heat flow predictions. (a) Predictions for optimal half-space cooling models fitted to global subsidence data. Black circles = water-loaded oceanic basement depths (Hoggard et al., 2017; Richards et al., 2018); purple line = model with constant thermal properties fixed to the values from Parsons and Sclater (1977); green line = purely temperature-dependent model using parameterisations from Korenaga and Korenaga (2016) for conductivity, expansivity and heat capacity; dashed orange line = pressure and temperature-dependent model using parameterisations from Korenaga and Korenaga (2016); red line = pressure and temperature-dependent model, including a 7 km-thick oceanic crustal layer and using parameterisations from Korenaga and Korenaga (2016). (b) Same for plate cooling models. (c) Predictions for optimal half-space cooling models fitted to global surface heat flow data. Grey boxes with bars = median and interquartile ranges of measurements corrected for sedimentation rates and filtered to remove hydrothermal circulation (Richards et al., 2018). (d) Same for plate cooling models. Optimal models and parameters are same as those shown in Figs. 6 and 7.

studies, we conclude that additional mechanisms for reducing effective thermal expansivity are not necessarily required by current observations.

In summary, the development of progressively more realistic modelling frameworks that incorporate experimentally constrained thermal properties have given rise to improved fits to subsidence, heat flow, and geochemical observations (Figs. 6 and 7). These findings appear to validate the scalability of pressure and temperature dependencies of thermal properties inferred from laboratory experiments to mantle conditions, and do not currently require proposed mechanisms such as thermal cracking to be invoked (Korenaga, 2007). However, it should be noted that also incorporating the effect of phase transitions (e.g. spinel-garnet) results in substantial misfits to subsidence data, indicating that some additional processes may yet be required to explain observed subsidence trends (Korenaga and Korenaga, 2016). As pointed out by Korenaga and Korenaga (2016), isotherms in half-space cooling and plate models begin to diverge at ~40 Ma in the deepest portions of the plate, but only become recognisably different in the surface observations beyond ~90 Ma (Figs. 8 and 9). Thus, the use of plate cooling models implies that resupply of basal heat begins earlier than the commonly assumed ~70 Ma onset age for small-scale convection. Nevertheless, better overall fits are generally obtained for plate models, especially in the Pacific domain, where seismological and magnetotelluric observations suggest flattening of the LAB in older portions of the plate.

3.2. Pervasiveness of seafloor flattening

Global compilations of subsidence, heat flow, and seismological observations generally indicate some form of 'flattening' at old plate ages, consistent with resupply of heat to the base of the lithosphere. Nevertheless, it is instructive to investigate whether this behaviour is consistently retrieved in each of the principal ocean basins.

3.2.1. Evidence from heat flow and subsidence measurements

We select the subset of subsidence and heat flow measurements that occur in each of the Pacific, Atlantic, and Indian Oceans (Fig. 10). Each basin exhibits basement depths with a degree of flattening at old ages, a feature that is generally more consistent with plate cooling than half-space cooling models. However, there are observable differences between basins, especially in their subsidence trends, which may represent differences in lithospheric cooling or regional variations in dynamic topography (Crosby and McKenzie, 2009). In the Pacific Ocean, basement depths are generally deeper than the global average at < 40 Ma and shallower from ~60 Ma onwards (Fig. 10c). The opposite is true in the Atlantic Ocean, where young basement depths lie above the global average and those > 100 Ma predominantly sit at or below this background trend (Fig. 10e). Indian Ocean basement depths are close to plate model predictions at all ages, albeit, slightly deeper on average at age ~50 Ma (Fig. 10g). Moreover, the age at which
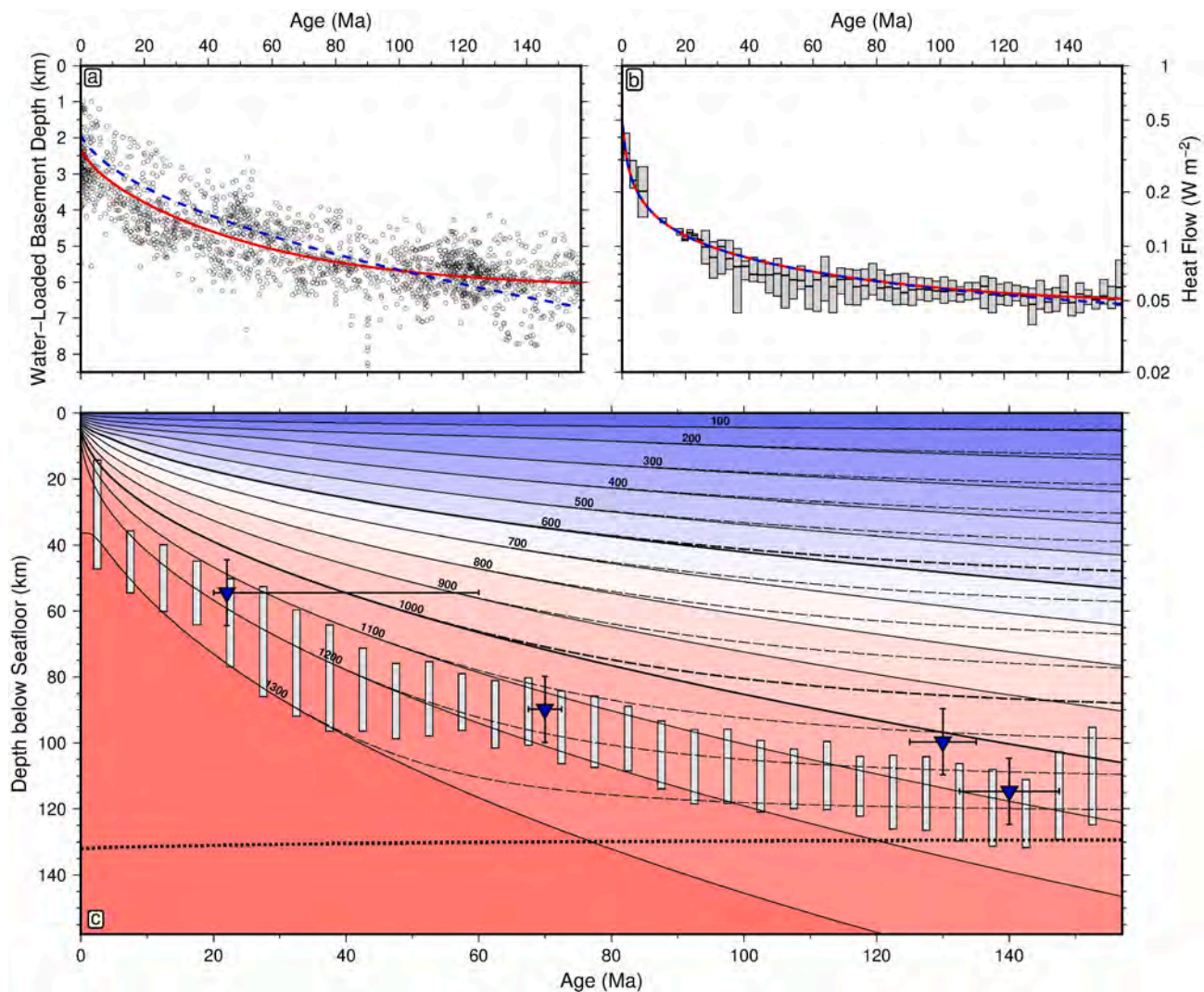
Fig. 9. Comparison of optimal half-space and plate cooling models. Both models are geochemically constrained to T_p = 1333°C, include pressure and temperature-dependence of thermal properties, and a 7 km-thick crustal layer. For the half-space, z_r = 1906 m; for the plate, z_r = 2292 m and z_p = 132 km. (a) Global subsidence data. Black circles = water-loaded oceanic basement depths (Hoggard et al., 2017; Richards et al., 2018); dashed blue line = half-space cooling model; red line = plate cooling model. (b) Global surface heat flow data. Grey boxes with bars = median and interquartile ranges of measurements corrected for sedimentation rates and filtered to remove hydrothermal circulation (Richards et al., 2018). (c) Predicted thermal structure compared to selected seismological and magnetotelluric observations. Solid/dashed numbered contours = half-space/plate cooling model isothermal surfaces plotted in °C; black dotted line = plate thickness; vertical grey bars = Pacific LAB inferred using depth to top of layer in which azimuthal anisotropy aligns with absolute motion (Burgos et al., 2014); blue inverted triangles = depth to high electrical conductivity layer defined using maximum curvature of conductivity profile (HCL; Utada, 2019).

subsidence apparently flattens off varies from ∼70 Ma in the Pacific to ∼100 Ma in the Atlantic and ∼120 Ma in the Indian Ocean.

Whilst water-loaded basement depth is affected by both lithospheric cooling and dynamic topography arising from deeper mantle flow, heat flow measurements should be predominantly influenced by the former. Similar patterns are observed between each basin once < 25 Ma measurements that are affected by hydrothermal circulation are removed, generally asymptotically approaching a value of ∼50 mW m^{-2} at old ages. These measurements appear to exhibit similar regional patterns to those observed in the subsidence data. However, the noisiness of heat flow measurements makes these trends uncertain. Moreover, the effect of basal heat resupply on surface heat flow will lag behind associated changes in basement depth by a period controlled by the conductive time constant of the lithosphere (∼70 Myr for a 150 km-thick layer of silicates; Turcotte and Schubert, 2002). As a result, there is no observable difference between the heat flow predicted by our optimal ∼135 km-thick plate model and equivalent half-space cooling models, even after 150 Ma. This observation is consistent with previous studies

investigating the impact of small-scale convection on surface heat flow (Korenaga, 2009).

3.2.2. Seismological evidence

Surface observables hint that there may be differences in behaviour between the ocean basins. It is therefore worth exploring whether this is the case for the seismological observations, which have higher sensitivity to variations in thermal properties as a function of depth. We have chosen to stack shear-wave velocity (V_S) profiles from global tomography models as a function of lithospheric age, both globally and for each individual basin (Fig. 11). Care is taken to excise anomalous regions affected by intraplate magmatism and pervasive faulting, such as fracture zones, seamounts, and oceanic plateaux, using the bathymetry and short-wavelength gravity anomaly-derived exclusion polygons of Hoggard et al. (2017). We then use the thermal structure from the optimal half-space and plate cooling models to predict the expected V_S structure in each case, and compare it to the observations.

We apply two different techniques for estimating the relationship
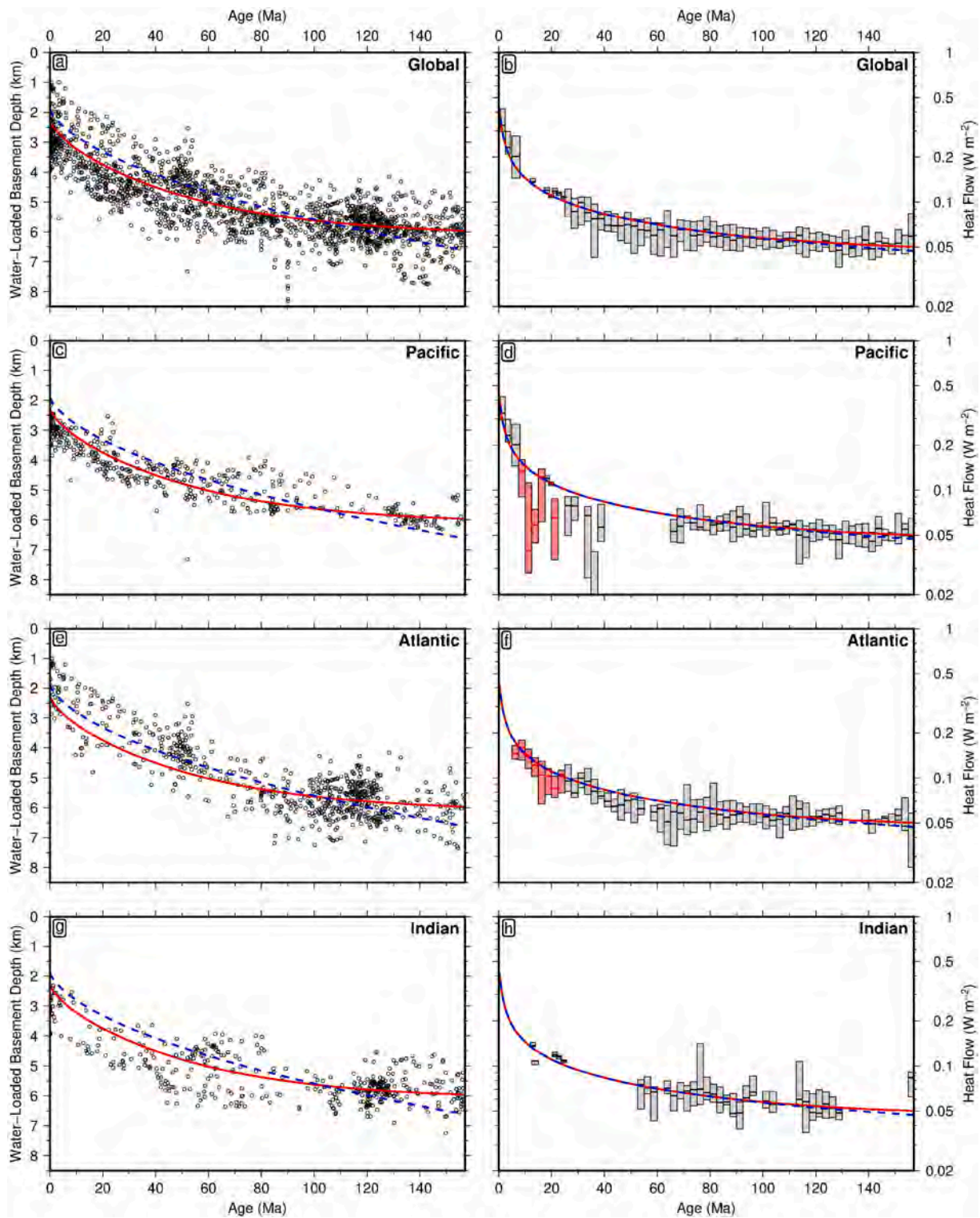
Fig. 10. Interbasin comparison of subsidence and heat flow trends. Thermal models are geochemically constrained to $T_p = 1333°C$, include pressure and temperature-dependence of thermal properties, and a 7 km-thick crustal layer. For the half-space, $z_r = 1906$ m; for the plate, $z_r = 2292$ m and $z_p = 132$ km. (a) Global subsidence data. Black circles = water-loaded oceanic basement depths (Hoggard et al., 2017; Richards et al., 2018); dashed blue line = half-space cooling model; red line = plate cooling model. (b) Global surface heat flow data. Grey boxes with bars = median and interquartile ranges of measurements corrected for sedimentation rates and filtered to remove hydrothermal circulation (Richards et al., 2018). (c) Subset of subsidence data from the Pacific Ocean only. (d) Subset of heat flow data from the Pacific Ocean only. Red boxes with bars = median and interquartile ranges of measurements excluded from global compilation due to hydrothermal circulation-induced heat flow deficit. (e) Atlantic Ocean subsidence. (f) Atlantic Ocean heat flow. (g) Indian Ocean subsidence. (h) Indian Ocean heat flow.

between temperature and V_S. The first is the forward modelling approach of Goes et al. (2012), where anharmonic velocities are calculated as a function of pressure and temperature using the Perple_X

software package and the thermodynamic database of Xu et al. (2008), assuming a pyrolitic mantle composition. These velocities are then corrected for anelastic effects assuming a dry peridotite solidus
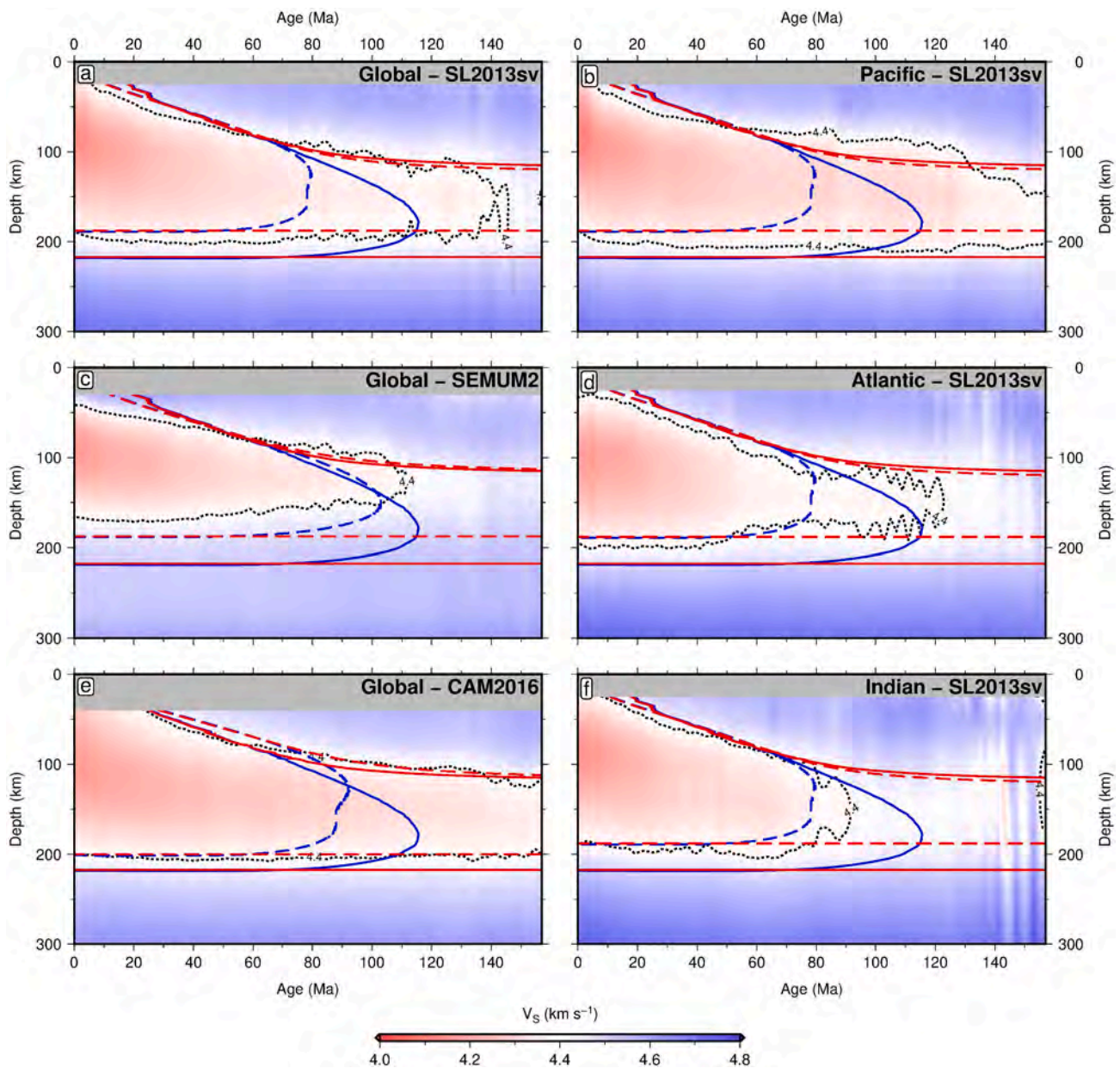
Fig. 11. Comparison between shear-wave velocities from seismic tomography and predictions from lithospheric cooling models. (a) Oceanic V_S from SL2013sv model stacked globally as a function of plate age (Schaeffer and Lebedev, 2013), excluding regions with anomalous oceanic crust using exclusion polygons from Hoggard et al. (2017). Contours are the 4.4 km s^{-1} isotach; black dotted = observed; blue solid = prediction from optimal half-space cooling model using Goes et al. (2012) anelastic parameterisation; red solid = same for optimal plate cooling model; blue dashed = prediction from optimal half-space cooling model using Yamauchi and Takei (2016) anelastic parameterisation with parameter values calibrated via inverse modelling for SL2013sv; red dashed = same for optimal plate cooling model. (b) Same for SL2013sv model stacked in Pacific Ocean. (c) Same for SEMUM2 model stacked globally (French et al., 2013). (d) Same for SL2013sv model stacked in Atlantic Ocean. (e) Same for CAM2016 model stacked globally (Ho et al., 2016). (f) Same for SL2013sv model stacked in Indian Ocean. Note that Yamauchi and Takei (2016) anelastic parameterisations in (c) and (e) use parameter values calibrated via inverse modelling for SEMUM2 and CAM2016, respectively (see Appendix F).

(Herzberg et al., 2000; Appendix B.3. in Lodhia et al., 2018). The second is the inverse approach pioneered by Priestley and McKenzie (2006), which we have coupled with the most recent polycrystalline anelastic parameterisation developed by Yamauchi and Takei (2016). This approach adopts an optimal thermal model to estimate oceanic mantle temperature, and an isentrope compatible with geochemical constraints in the upper mantle. By combining these temperature estimates with measurements of V_S, attenuation and viscosity as a function of age and depth, a suite of tie points are generated that can be inverted to obtain the various anharmonic and anelastic parameters (see Appendix F and Methods section of Hoggard et al., 2020). An advantage of this methodology is that mantle composition does not have to be

assumed in advance. Separate parameterisations are calibrated for each of the tested tomographic models: SL2013sv (Schaeffer and Lebedev, 2013), SEMUM2 (French et al., 2013) and CAM2016 (Ho et al., 2016). In order to avoid circularity when investigating the presence or absence of flattening at older ages, we use only the first 70 Ma of a half-space cooling model to create oceanic V_S-to-temperature tie points for this calibration procedure. Note that some of the tomographic models we test only record the vertical component of shear-wave velocity (V_{SV}) so, to facilitate inter-model comparison, we use V_{SV} in all calculations. By contrast, when applying the Goes et al. (2012) parameterisation, we do not convert anharmonic V_S from Perple_X into V_{SV} because of uncertainties in the depth profile of upper mantle radial anisotropy.

Consequently, a fraction of the depth-dependent divergence between the two parameterisations may result from anisotropic effects.

By applying two independent conversion methodologies, each with their own merits and disadvantages, it is possible to gauge not only whether imaged V_S variations are consistent with a particular cooling model, but also the extent to which these conclusions are robust to uncertainties associated with temperature to V_S conversion. To compare the performance of different cooling models and conversion methodologies, for each age-depth stack we calculate the misfit, χ, between predicted, V_{ij}^c, and observed V_S, V_{ij}^o, using

$$\chi = \sqrt{\frac{1}{M}\sum_{i=1}^{M}\frac{1}{N}\sum_{j=1}^{N}\left(\frac{V_{ij}^o - V_{ij}^c}{\sigma_{ij}}\right)}, \qquad (1)$$

where M represents the number of age bins between 0 Ma and 150 Ma, N represents the number of depth bins between the uppermost depth slice of the model and 300 km depth, and σ_{ij} reflects uncertainty in the V_S measurement, assumed to be a constant 0.1 km s^{-1} based on typical variations between different tomographic models at a given location.

For the SL2013sv and CAM2016 models, global V_S stacks are more consistent with plate cooling predictions (Fig. 11a and e; Table 2). By contrast, SEMUM2 is more consistent with a half-space cooling model (Fig. 11c). However, it should be noted that the misfit between predicted and observed V_S variations obtained for the other models is generally ~40% lower than for SEMUM2. This may reflect the fact that, although SEMUM2 uses a more sophisticated finite frequency approach, it is constructed using fewer waveforms than the other two models (~100,000 vs. > 750,000), reducing the density of ray path crossings and potentially resolution of the lithosphere-asthenosphere boundary region.

The Pacific pattern of shear-wave velocities agrees well with a plate model for both methods of converting temperatures into predicted V_S structure (Fig. 11b; Table 2). Intriguingly, deviations in the age dependence of shear-wave velocities mirror Pacific subsidence trends, with observed velocities initially exceeding plate model predictions, before becoming slower after ~70 Ma. This result supports a strong link between bathymetry and seismically imaged lithospheric thermal structure. In contrast, Atlantic shear-wave velocities are slightly better fit by half-space cooling models (Fig. 11d; Table 2). As for the subsidence data, flattening with respect to half-space predictions occurs after 80–100 Ma but, unlike in the subsidence data, after ~120 Ma velocities begin to deviate back towards a half-space cooling trend. Atlantic velocity structure therefore seems to be intermediate between plate and half-space cooling model expectations. Indian Ocean velocity structure is similar to that of the Atlantic in that it fits plate and half-space cooling predictions equally well (Fig. 11f; Table 2). Indian Ocean velocities largely follow half-space cooling expectations, possibly even cooling slightly faster until 120 Ma. After 120 Ma, slow shear-wave velocities reappear at ~ 125 km depth, which may be consistent with a resupply of basal heat responsible for the late flattening detected in subsidence data. In short, seismic velocity patterns in the tomographic models are largely consistent with the subsidence trends of individual

basins, suggesting that systematic differences in lithospheric thermal evolution may explain the first order differences between basins. All ocean basins show some degree of flattening with respect to half-space cooling predictions (Fig. 11). However, its onset is delayed and its magnitude is reduced in the Indian and Atlantic Oceans, leading to similar levels of fit for both cooling models in those two regions (Table 2).

Our conclusions appear to be robust to the choice of temperature to V_S conversion methodology, although the inverse calibration method yields ~25–60% lower misfit between predicted and observed shear-wave velocities. Moreover, while results vary in detail between seismic tomographic models, the first-order differences between individual ocean basins are largely consistent. Out of the models we have examined, only SEMUM2 does not exhibit significant plate-like behaviour in global stacks (French et al., 2013). This model has the least dense upper mantle ray coverage and this result may therefore reflect lower resolution in the oldest regions of ocean basins, which often abut thicker, higher velocity continental lithosphere. It appears that seafloor flattening occurs to some extent in all three major ocean basins. However, the onset time may be variable, beginning earliest in the Pacific (~70 Ma), followed by the Atlantic (~100 Ma) and Indian oceans (~120 Ma). This pattern appears to be consistent with mantle potential temperatures at the ridge axis, providing support for a mechanism involving the variable onset time of small-scale convection beneath the lithosphere (Ma and Dalton, 2019).

3.3. Mechanisms responsible for resupply of basal heat

Evidence for resupply of basal heat beneath old lithosphere, at least in the case of the Pacific Ocean, appears to be unequivocal. A plate cooling model attempts to represent this behaviour by introducing a constant temperature boundary condition at a particular depth controlled by the plate thickness. Whilst this model has had some success in matching subsidence, heat flow and seismological observations on old seafloor, this condition is somewhat arbitrary from a physical perspective, and the question remains: what process is responsible for re-supplying heat to the base of the lithosphere?

Several processes have been invoked to explain this behaviour. These include: thermal rejuvenation of the lithosphere as it passes over hotspots (Davies, 2011); advection of hot, plume-fed asthenosphere beneath older areas of the plate due to pressure-driven flow (Morgan and Smith, 1992); resupply of basal heat due to the decay of radionuclides (Korenaga, 2015); and the initiation of small-scale convection at the base of the plate as the lithosphere cools and thickens (Parsons and McKenzie, 1978). These different hypotheses have proven difficult to test, although insights from subsidence, heat flow, gravity and seismological data provide some indication of which is most likely. We provide a brief summary of each in turn.

Based on global analyses of oceanic basement depths, some studies have suggested that deviation of subsidence trends from half-space cooling predictions is restricted to areas that have been affected by intraplate hotspot magmatism and thermal rejuvenation by mantle plumes (Korenaga and Korenaga, 2008). However, re-examination of the original dataset, in addition to new compilations in which 'anomalous' regions affected by seamount volcanism, large igneous provinces and aseismic ridges have been carefully excised, suggest statistically significant flattening continues for ages beyond 70 Ma (Crosby et al., 2006; Crosby and McKenzie, 2009; Hillier, 2010; Hoggard et al., 2017; Richards et al., 2018). Moreover, Ma and Dalton (2019) found no significant correlation between intraplate volcanism and the failure of half-space cooling models to recreate shear-wave velocity and subsidence observations. Thus, this mechanism seems to be unsatisfactory unless the lithosphere can be thermally rejuvenated by plumes in the absence of associated volcanism, which has been difficult to achieve in numerical simulations (Sleep, 1994). Ocean island drowning histories suggest that, even at sites with substantial intraplate magmatism,

Table 2
Summary of misfit between observed and predicted V_S for half-space and plate cooling models. HSC = half-space cooling model; P = plate model; G12 = Goes et al. (2012) parameterisation; YT16 = calibrated Yamauchi and Takei (2016) parameterisation (see Appendix F).

Tomographic model	Region	χ_{HSC}^{G12}	χ_P^{G12}	χ_{HSC}^{YT16}	χ_P^{YT16}
SL2013sv	Global	0.96	0.96	0.56	0.43
SEMUM2	Global	1.24	1.32	0.91	0.96
CAM2016	Global	1.07	0.97	0.56	0.36
SL2013sv	Pacific	1.00	0.91	0.73	0.44
SL2013sv	Atlantic	1.04	1.10	0.55	0.56
SL2013sv	Indian	0.98	1.05	0.50	0.54

thermal rejuvenation of the lithosphere is not compatible with observed rates of subsidence downstream of hotspots (Huppert et al., 2020).

There is increasing evidence for the presence of a warm, low viscosity channel immediately beneath the plates that is fed by mantle plumes (Craig and McKenzie, 1986; Morgan et al., 1995; Lin et al., 2016; Stotz et al., 2018). Deeper mantle flow, mid-ocean ridge spreading, and subducting slabs can act to generate dynamic pressure gradients within this channel, which may be responsible for supporting seafloor at old ages (Morgan and Smith, 1992; Yamamoto et al., 2007; Holt et al., 2017; Rowley, 2018). However, it remains unclear how widespread this channel may be, and whether pressure gradients are correctly oriented to explain the degree of flattening observed in different basins (Natarov and Conrad, 2012; Becker et al., 2012; Schaeffer et al., 2016; Ho et al., 2016). Seismological constraints on anisotropy are likely to prove key to illuminating the asthenospheric flow field and testing the plausibility of this mechanism.

The decay of radionuclides provides an additional source of heat that, when added to background advection of thermal anomalies by mantle flow, may help to prevent continuous cooling of the lithosphere as a function of age, possibly contributing to seafloor flattening (Jarvis and Peltier, 1982). However, numerical modelling studies that quantify the influence of this internal heat source find that the required magnitude of flattening cannot be reproduced with geochemically plausible values of internal heat production (8.5 $\pm$ 5.5 TW), unless small-scale convection also plays an active role (Korenaga, 2008, 2015). Moreover, it is unclear to what extent the conclusions drawn from these simplified two-dimensional models can be applied to the complex three-dimensional pattern of convection in the real Earth. It therefore seems that, although radiogenic heat production may enhance the resupply of heat to the base of the lithosphere, in isolation, it is insufficient to explain observed age-depth subsidence trends.

The mechanism for resupplying heat to the base of the lithosphere that is most widely invoked, and for which the evidence is probably most compelling, is small-scale convection. This process is thought to initiate as the thermal boundary layer cools and thickens, eventually passing a critical threshold beyond which it mechanically destabilises and begins to convect away (Parsons and McKenzie, 1978; Houseman and McKenzie, 1982; Fleitout and Yuen, 1984; Davaille and Jaupart, 1994; Korenaga and Jordan, 2003b; Zaranek and Parmentier, 2004; Huang and Zhong, 2005; van Hunen et al., 2005). The onset of small-scale convection is predicted by fluid dynamical theory and laboratory experiments, and there are several strands of supporting evidence in observational datasets. Indeed, some studies have observed flattening, and potentially even shoaling, of global oceanic bathymetry at ages ranging from 70 Ma to 120 Ma (Crosby et al., 2006; Crosby and McKenzie, 2009; Hillier, 2010; Hoggard et al., 2017). It has also been suggested that a minor increase in observed heat flow at ages $\geq$ 132 Ma may be the delayed surface expression of these lithospheric instabilities, although observations at these ages have a very restricted spatial extent (McKenzie, 2018). Seismological evidence includes the study of Ritzwoller et al. (2004), which used surface wave velocities to show that the effective thermal age of the Pacific lithosphere follows half-space cooling trends until ~70 Ma, then remains flat until 100 Ma, when cooling resumes at a slower rate. This observation is supported by the work of Ma and Dalton (2019) who found a breakdown in the ability of half-space cooling models to match observed subsidence and surface wave phase velocities in certain older regions of the ocean basins, as also illustrated here in Section 3.2.

Theoretical arguments and observations indicate that the onset of small-scale convection may be abrupt and vary in time between different locations. One theory to explain this is that, as depleted harzburgite residue is more viscous than fertile lherzolite, the exact onset time is controlled by the depth extent of adiabatic decompression melting when the material was at the ridge axis (Korenaga and Jordan, 2002; Lee et al., 2005; Afonso et al., 2008b; Ballmer et al., 2009; Beghein et al., 2018). Ma and Dalton (2019) found evidence to support

this view by linking the variable onset age at which subsidence and surface wave phase velocities depart from half-space cooling expectations to changes in axial ridge depth at the present-day ridge axis (a proxy for potential temperature), assuming that this value has remained constant over the intervening time period. An alternative explanation for sudden and relatively consistent onset of small-scale convection beneath the oceans is that the pargasite dehydration solidus occurs at depths of ~90 km (Brown and Lesher, 2016; Niu and Green, 2018). This particular amphibole forms when the mantle has high water content, and its breakdown at 90 km to produce small amounts of melt may significantly alter rheological properties of the lithosphere, causing it to mechanically destabilise and begin convecting. However, it remains uncertain whether the ~100 ppm of water present in oceanic peridotite is sufficient to stabilise significant quantities of pargasite, and whether the small volume of melt produced at this interface would significantly alter rheological behaviour (Brown and Lesher, 2016). Given these issues and the apparent variability in flattening onset time in different locations, the pargasite dehydration mechanism currently appears to be less satisfactory for explaining seafloor flattening than variable melt depletion depths.

4. Residual depth anomalies and density structure of the upper mantle

Although additional observational and experimental constraints have improved our understanding of the global and basin-averaged behaviour of oceanic lithosphere, significant regional deviations have been detected in many datasets. These anomalies provide important insights into deep Earth processes, in particular the evolving planform of mantle convection, melt generation, and the length scales of compositional heterogeneity (Winterbourne et al., 2009; Zhou and Dick, 2013; Dalton et al., 2014). Although their individual interpretation is not straightforward and often ambiguous, powerful constraints can be obtained by combining multiple independent datasets.

Local departures from average subsidence trends place important bounds on dynamic topography arising from buoyancy variations and convective flow within Earth's interior, and the study of these *oceanic residual depth anomalies* has a long history (Menard, 1973; Cochran and Talwani, 1977; Le Douaran and Parsons, 1982; Crough and Jarrard, 1981; Crough, 1983; Cazenave et al., 1988). Until recently, the general paucity of modern controlled-source seismic experiments throughout oceanic regions made it harder to accurately correct for the effects of sedimentary loading and crustal thickness variation, especially on older oceanic plates close to continental margins. Thanks to the burgeoning availability of industrial seismic reflection surveys over the last two decades, inventories of > 2000 well-resolved measurements have been assembled (Winterbourne et al., 2014; Hoggard et al., 2017). These global databases have revealed significant undulations in residual bathymetry with peak amplitudes of $\pm$ 2 km and lateral wavelengths as short as 1000 km (Hoggard et al., 2016).

The significant contribution of shorter wavelength components to the oceanic residual topography field necessitates lateral variations in buoyancy structure within the shallow mantle at depths pertaining to the asthenosphere and/or lithosphere (Klein and Langmuir, 1987; Hoggard et al., 2016). Until recently, it has been difficult to image these features. However, computational advances and larger quantities of seismograms have enabled the creation of global surface wave tomographic models with sufficient resolution to detect velocity variations at these length scales (Priestley and McKenzie, 2013; Schaeffer and Lebedev, 2013; French et al., 2013; Debayle et al., 2016). Determining the amplitude and extent of anomalous buoyancy requires removal of the background lithospheric cooling trend in models of upper mantle velocity structure (Fig. 12a). This detrending can be achieved by stacking shear-wave velocity (V_S) profiles across the global ocean as a function of age, taking care to excise anomalous regions such as fracture zones, oceanic plateaux and aseismic ridges (Section 3.2; Fig. 12b).
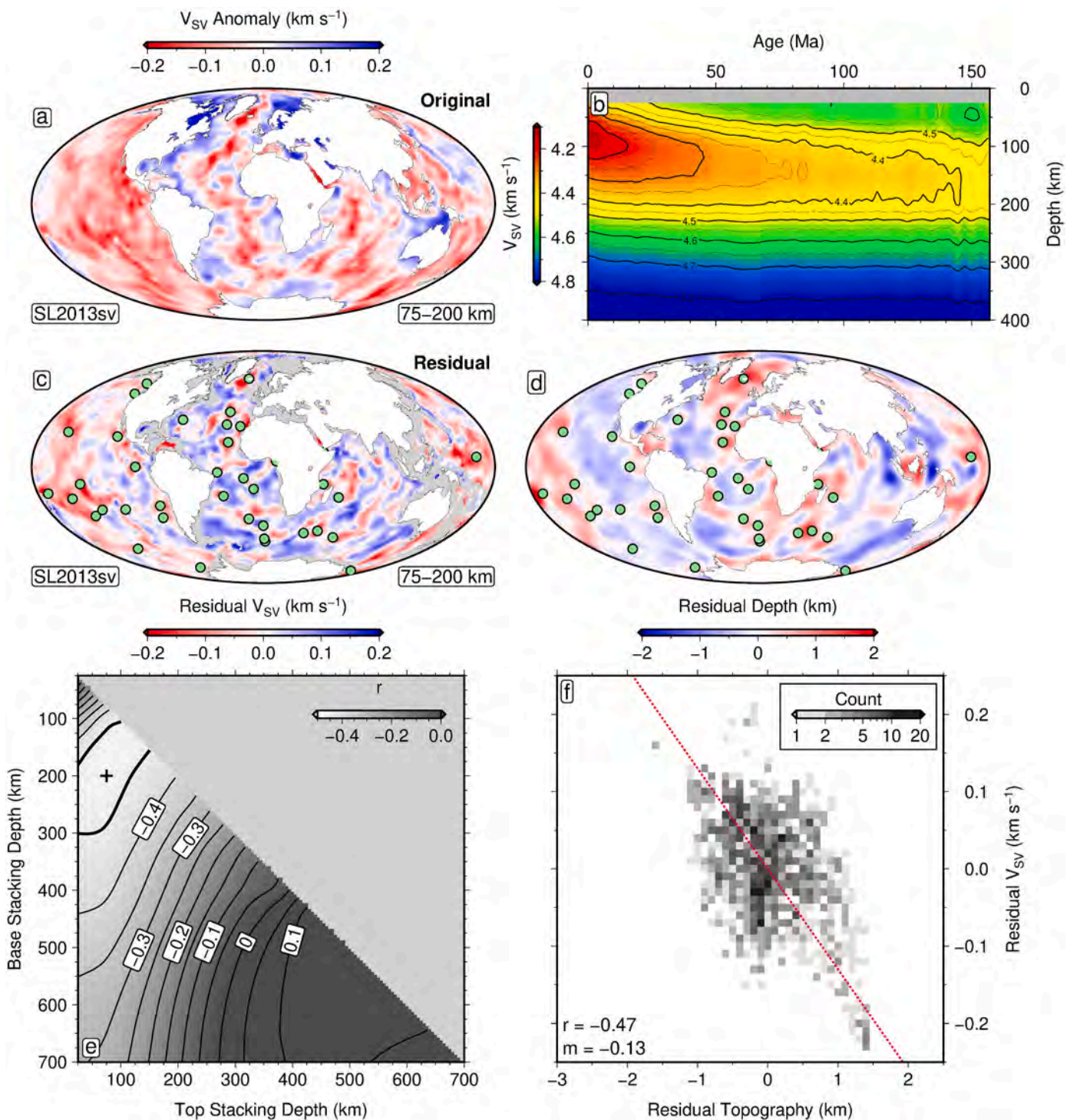
Fig. 12. Comparison between oceanic residual tomography and residual topography, following Richards et al. (2020). (a) SL2013sv shear-wave velocity anomalies averaged between depths of 75 km and 200 km (Schaeffer and Lebedev, 2013). (b) SL2013sv stacked globally in the oceans as a function of plate age, excluding regions with anomalous oceanic crust using the exclusion polygons of Hoggard et al. (2017). (c) Residual shear-wave velocities calculated by subtracting values from the global stack at the equivalent age from the local velocity structure, and averaging between depths of 75 km and 200 km. Green circles = major oceanic hotspots. (d) Spherical harmonic fit to residual depth measurements of Hoggard et al. (2017) up to maximum degree of 30. (e) Correlation between residual depth and residual shear-wave velocities as a function of depth over which velocity anomalies are averaged. r = Pearson's correlation coefficient; black cross = optimal correlation. (f) Pointwise correlation between residual depth measurements and residual shear-wave velocity averaged between depths of 75 km and 200 km. Red dashed line = best-fitting linear relationship; m = gradient of that fit.

Removal of this background trend results in a map of *residual tomography* (Wen and Anderson, 1997; Richards et al., 2020).

Assuming that temperature is the dominant cause of remaining residual velocity anomalies, the resulting pattern for the SL2013sv model is consistent with surface magmatism (Schaeffer and Lebedev, 2013). More than 80% of magmatic hotspots coincide with anomalously slow residual velocities in the upper mantle, and only Marion and St. Helena are greater than 200 km from the nearest low-velocity anomaly
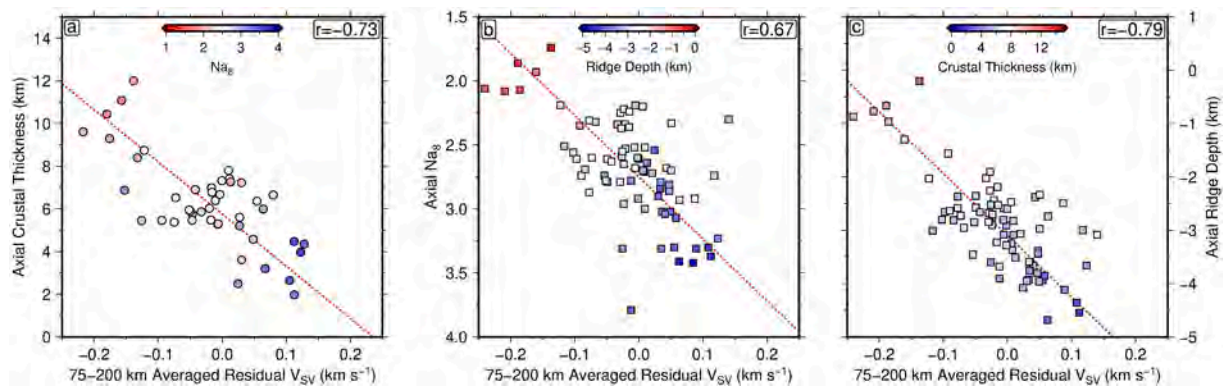
Fig. 13. Relationship between residual tomography and observational proxies for mantle temperature at the ridge axis. (a) Axial crustal thickness measurements plotted as a function of residual shear-wave velocity from SL2013sv model (75–200 km average; see Fig. 12c). Circles = average crustal thickness measurements (coloured according to Na_8 value) obtained from controlled-source seismic experiments compiled by Hoggard et al. (2017) for oceanic lithosphere younger than 5 Ma and located within 300 km of ridge axis. Measurements are averaged for each ridge segment from database of Gale et al. (2013). r = Pearson's correlation coefficient. (b) Same for axial Na_8 values. Squares = average values per ridge segment with more than 30 dredge sample analyses, coloured according to axial ridge depth (Gale et al., 2014) (c) Same for axial ridge depths at ridge segments identical to those shown in panel (b) and coloured according to axial crustal thickness. Gray points are located > 200 km from the nearest crustal thickness measurement.

(Fig. 12c). Moreover, there is clear spatial anti-correlation between residual topography and residual shear-wave velocities, suggesting a relationship between warm upper mantle temperatures and excess bathymetry (Fig. 12d). When both fields are expanded up to spherical harmonic degree 30, the optimal spatial correlation occurs when residual tomography is stacked over a depth range of 75–200 km ($r = -0.47$; Fig. 12e and f).

The contention that upper mantle shear-wave velocity and residual depth anomalies are largely controlled by temperature is further corroborated by several independent geochemical and geophysical observations at mid-ocean ridges. The crustal thickness produced at a spreading centre depends upon the volume of melt generated by decompression melting beneath the ridge axis, and is therefore a proxy for asthenospheric temperature (Klein and Langmuir, 1987; McKenzie and Bickle, 1988). Crustal thickness measurements from active ridges in the database of Hoggard et al. (2017) are found to be anti-correlated with residual tomography (Pearson's correlation coefficient $r \sim$ -0.7; Fig. 13a). In a similar manner, sodium concentration in mid-ocean ridge basalt (MORB) is a proxy for mantle temperature because it behaves incompatibly during melting, occurring in high concentrations for low melt fraction basalts and progressively diluting as melt fraction rises. Na_8 is defined as the concentration of Na_2O in a sample following correction for the fractional crystallisation of olivine back to 8 wt% MgO. Using the geochemical database of Gale et al. (2014) along mid-ocean ridge axes, a strong positive correlation ($r \sim 0.7$) is observed between residual velocities and basalt Na_8 (Dalton et al., 2014; Fig. 13b). Finally, there is a strong negative correlation between residual velocity and axial ridge depth that is compatible with temperature-controlled excess buoyancy ($r \sim$ -0.8; Fig. 13c).

Taken together, close agreement between these independent datasets indicates that thermal rather than compositional variations are the major control on sub-plate velocity anomalies. Despite tomographic resolution issues and the non-negligible contribution of deeper mantle flow, the match between residual tomography and residual depth anomalies at wavelengths shorter than ~6000 km underlines the importance of shallow mantle structure for supporting local deviations from age-depth cooling (Hoggard et al., 2016). It remains a topic of considerable ongoing research as to whether these buoyancy anomalies reside in the lithospheric mantle, within the asthenosphere, or both (Ball et al., 2019; Davies et al., 2019; Richards et al., 2020).

5. Remaining controversies and frontiers

The last 50 years have seen a considerable amount of work

conducted to investigate the structure and dynamics of the oceanic lithosphere-asthenosphere system. While seafloor spreading and the progressive cooling of a thermal boundary layer have successfully reconciled many of the first-order features visible in observational datasets, there remain several topics that are the focus of ongoing research efforts. Here, we finish this review by selecting three areas in which we anticipate significant progress to be made in the near future.

5.1. Can thermodynamically self-consistent models of the evolving oceanic upper mantle be constructed?

Assuming that the bulk thermal properties of lithospheric mantle are well-approximated by those of olivine provides satisfactory fits to many available datasets in the oceanic realm (Section 3.1; Richards et al., 2018). However, this assumption is probably overly simplistic, especially in terms of the evolution of composition and density structure with age. First, aluminous mantle lherzolites are depleted in clinopyroxene and plagioclase by melt extraction beneath the ridge axis, reducing the density of the harzburgitic residuum (Schutt and Lesher, 2006). Secondly, the aluminous phase that is stable in peridotite switches from plagioclase to spinel to garnet with increasing pressure, with the exact depth of transition dependent on both temperature and composition (Gasparik, 1984; Klemme, 2004). The spinel-garnet transition, in particular, could have a significant influence on subsidence as the depth of the transition is expected to decrease as the lithosphere cools, thickening the garnet stability field at older ages (Afonso et al., 2007, 2008a). Spinel and garnet are the densest major constituents of mantle peridotites, and therefore exert an important control on its overall buoyancy. While spinel is generally more dense than garnet, its modal proportion in peridotite is ~75% smaller, leading to a significant increase in the net density of the lithosphere as the garnet stability field expands (Schutt and Lesher, 2006; Bjerg et al., 2009; Korenaga and Korenaga, 2016).

The role of these compositional variations can now be investigated thanks to the development of powerful software packages that exploit growing mineral physics databases and sophisticated computational methods to predict how intrinsic physical properties of mantle lithologies vary as a function of temperature, composition and pressure (e.g. THERMOCALC, Powell and Holland, 1988; pMELTS, Ghiorso et al., 2002; Perple_X, Connolly, 2005; HeFESTo, Stixrude and Lithgow-Bertelloni, 2005; Theriak-Domino, de Capitani and Petrakakis, 2010; MMA-EoS, Chust et al., 2017). These software packages, and the thermodynamic datasets that underpin them, have successfully reproduced many fundamental observations. However, fully reconciling

petrological and geophysical models of the lithosphere-asthenosphere system remains a challenge. For example, lithospheric cooling models that incorporate the garnet-spinel phase transition predict that subsidence rates increase by an extra 80 m Myr^{-1} after 20 Ma to values of ~500 m Myr^{-1} (Korenaga and Korenaga, 2016). This rate is well above observed trends, necessitating the invocation of additional processes to counteract this effect. These processes include thermal cracking, and also a systematic increase in temperature beneath older aged lithosphere that extends throughout the deep mantle, which the authors attribute to the combined effects of radiogenic heating and secular cooling (Korenaga and Korenaga, 2016). However, as noted previously in Section 3, there is little observational evidence for the operation of thermal cracking on the scale envisaged by this study, and seismic tomographic models do not consistently image warmer mantle beneath older portions of the plate. Finally, as with the subsidence data, seismological observations such as tomographically imaged shear-wave velocity structure are better fit by calibrated pressure and temperature-dependent parameterisations than those that also account for phase transitions (see Fig. 11; Table 2). Some of this mismatch can be ascribed to seismic resolution issues, limited understanding of melting behaviour, and the uncertain contribution of anelastic effects. However, the magnitude of the discrepancy suggests that the equations of state that underpin these thermodynamic calculations may require some refinement (Beghein et al., 2018).

It therefore seems likely that these discrepancies partly reflect inaccurate or incomplete thermodynamic data, which often requires extrapolation of properties from laboratory to mantle conditions using pressure and temperature derivatives (Schutt and Lesher, 2006). Moreover, phase transitions and accompanying density and mineral proportion changes are dependent on the composition, volatile content and oxidation state, all of which are uncertain in the upper mantle (Jennings and Holland, 2015). A further important caveat is that the application of bulk equilibrium thermodynamics to these problems is increasingly being questioned, particularly in the case of melt formation and reactive transport, where effects of multiple phases and local reaction kinetics are likely to be important (Aagaard and Helgeson, 1982; Kelemen et al., 1992). Software capable of tackling these complex systems is currently in development, but its impact on our understanding on the evolution of oceanic lithosphere remains unknown (Tirone and Sessing, 2017; Tweed et al., 2019; Grose and Afonso, 2019a). Subsequently, it is not clear that experimental databases are sufficiently complete, nor upper mantle chemistry adequately constrained, for thermodynamically self-consistent phase assemblages to be accurately incorporated into thermal models at present.

Notwithstanding these issues, this topic remains a core goal of the Earth sciences. If remaining difficulties can be overcome, combined petrological and geophysical modelling has the potential to dramatically improve our understanding of melt extraction, evolution of the garnet-spinel transition, and the lengthscales of chemical heterogeneity in the upper mantle. Moreover, given the relative youthfulness and simplicity of the oceanic lithosphere-asthenosphere system, reconciling geophysical observations with models of its compositional evolution is likely to be key to improving our understanding of thermochemical structure in more complicated settings, including in subduction zones and the continental lithosphere.

5.2. Why are small-scale convection cells not consistently imaged?

Many models and observations indicate the likely role of small-scale convection at the base of the plate in maintaining observed oceanic subsidence, heat flow, seismic velocity and gravity anomaly patterns (Huang and Zhong, 2005). However, given the apparent pervasiveness of this process and its potentially abrupt onset, it is perhaps surprising that observations of a systematic change in the planform of mid-wavelength gravity anomalies and seismic anomalies remains elusive.

Beneath fast-moving plates such as the Pacific Ocean (~100 mm

yr^{-1}), convection simulations and laboratory studies have predicted that small-scale convection may take on the form of longitudinal rolls organised parallel to the direction of shear (plate motion), known as *Richter rolls* (Richter, 1973; Richter and Parsons, 1975; Buck and Parmentier, 1986). The wavelength of these features is expected to be similar to the thickness of the low-viscosity asthenosphere (~200 km; Richter, 1973; Craig and McKenzie, 1986). Although the onset of small-scale convection is not theoretically expected to occur until > 50 Ma for mantle viscosities compatible with studies of glacial isostatic adjustment, the most convincing observations of this behaviour come from significantly younger lithosphere near the ridge axis (Davies, 1988; Korenaga and Jordan, 2003b). 100 km–500 km wavelength geoid, gravity and topography lineations have been detected in both the Pacific and Indian Oceans at ages ranging from 5 Ma to 100 Ma, often accompanied by non-age-progressive intraplate volcanism (Haxby and Weissel, 1986; Cazenave et al., 1987; Maia and Diament, 1991; Marquart et al., 1999; Harmon et al., 2006; Ballmer et al., 2007; Cadio and Korenaga, 2016). Alternative explanations have therefore been put forward, including lithospheric extension, plate motion-parallel thermal contraction, or channelised asthenospheric flow (Sandwell et al., 1995; Gans et al., 2003; Holmes et al., 2007; Weeraratne et al., 2007; Cormier et al., 2011). On a broader scale, French et al. (2013) have used seismic tomography to image elongated low-velocity structures in the asthenosphere beneath all of the ocean basins. However, these features underlie lithosphere of all ages, appear to be offset from observed geoid undulation patterns, and are much longer wavelength (~1500 km) than existing geodynamic models predict for small-scale convection cells (French et al., 2013).

If it does occur, the lack of unambiguous detections of small-scale convection in subsidence, heat flow, gravity and seismic wave speed anomalies at ~200 km wavelengths may indicate that these observations currently have insufficient signal-to-noise ratios, or are being overprinted by other processes occurring at similar wavelengths. However, it may also suggest that the convection cells are even smaller in scale than anticipated, possibly as a result of anisotropic viscosity, non-linear rheology, melt-induced destabilisation, or complexities introduced by the interplay between compositionally buoyant, high-viscosity depleted mantle and lower viscosity, fertile mantle (Lev and Hager, 2008). Moreover, as the onset time of small-scale convection is highly sensitive to viscosity, and the extent of melt depletion at the ridge axis is likely to vary geographically, the change in geophysical observables associated with small-scale convection may not be sufficiently systematic for it to be clearly discerned from background trends (Korenaga and Jordan, 2003b; Afonso et al., 2008b; Ma and Dalton, 2019). Finally, two-dimensional linear stability analysis suggests that if the local Rayleigh number associated with small-scale convection is sufficiently high, roll-like convective features would eventually become unstable, even at high plate velocities (Korenaga and Jordan, 2003a, 2004). As a result, small-scale convective planforms could become disordered and multimodal at older ages, complicating their detection in geophysical observations (e.g. Busse and Whitehead, 1971).

In summary, although convincing observations of small-scale convection are currently lacking, the thermal evolution of the oceanic lithosphere inferred from oceanic datasets provides compelling evidence for its operation beneath large swathes of the seafloor. Ongoing efforts to deploy high-density seismic arrays in ocean basins, such as the Pacific Array and ORCA experiments, allow the oceanic thermal boundary region to be studied in far greater detail (Kawakatsu and Utada, 2017; Gaherty et al., 2018). In particular, detailed seismic anisotropy observations may allow complex flow patterns to be identified and conclusively confirm the presence or absence of small-scale convection.

5.3. Can we match geophysical observables with dynamical models of lithospheric cooling?

Seismological, magnetotelluric and subsidence data all appear to show flattening at old ages that is consistent with a basal resupply of

heat. Whilst the plate model is one attempt to represent this behaviour, it is a simplification of the physical processes that control the transition from the conductively cooling mechanical boundary layer into the convecting thermal boundary layer and adiabatic mantle beneath. Key assumptions are that oceanic lithosphere cools purely by conduction to a fixed depth, below which temperature is held constant, and that this densification is perfectly coupled to surface bathymetry by isostatic compensation, with zero contribution from structure deeper than the notional plate thickness. This effect introduces an inconsistency whereby the model assumes no advective flow of material, yet isostasy necessitates lateral flow of material beneath the compensation depth to equalise lithostatic pressure gradients.

In the context of a vigorously convecting mantle, viscous flow produces pressure gradients and dynamical stresses that affect the coupling between internal density anomalies and bathymetry. This behaviour can be more accurately described by weighting cooling-related density changes with a wavelength-dependent *topographic response kernel*, H, that accounts for variations in viscosity as a function of depth (Parsons and Daly, 1983). H is unity in the high-viscosity mechanical boundary layer, corresponding to full expression of isostatic topography at the surface. H then decreases smoothly to between ~ 0.8 and ~ 0.3 at the base of the low-viscosity thermal boundary layer, depending on the wavelength of the density anomaly and viscosity contrast between this layer and the underlying mantle (Fig. 14; Robinson and Parsons, 1988). This behaviour contrasts with the plate model, where $H = 1$ everywhere above the notional plate thickness and $H = 0$ below.

The increase in lithospheric density and resulting seafloor subsidence scales with the depth-integrated temperature change between the geotherm and the original adiabat. Importantly, as illustrated by the schematic example shown in Fig. 14, $\sim 90\%$ of this temperature change occurs within the mechanical boundary layer, where $H = 1$ and both formulations produce the same quantity of subsidence. The remaining $\sim 10\%$ of subsidence is controlled by temperature changes within the thermal boundary layer, where H is less than 1. However, the deviation from the original ridge adiabat is relatively modest at these depths, and, as a result, the depth-integrated temperature change, when weighted by the kernel, is within 2% of the equivalent value that would be obtained for the plate model. Given the ≥ 100 m uncertainties in water-loaded basement depth calculations, this difference is below the threshold of detectability. This result also potentially reconciles the apparent inconsistency between otherwise successful plate models, where temperature differences persist no deeper than 95–135 km, and seismic observations that indicate age-dependent temperature variations actually persist to depths of ~ 150 km (e.g. Fig. 11).

In order to account for additional complexities such as a spherical geometry, Richards and Hager (1984) extended the *instantaneous flow* kernel approach outlined by Parsons and Daly (1983). In their formulation, spatially varying fields, such as the internal density structure, are expressed in spherical harmonics of degree, l, and order m. The equivalent wavelength, λ, of a given harmonic at the Earth's surface can be calculated using $\lambda = \frac{2\pi R_{\oplus}}{\sqrt{l(l+1)}} \approx \frac{40{,}000 \text{ km}}{l + 0.5}$, where $R_{\oplus}$ is the Earth's radius (6371 km). Water-loaded deflections of the Earth's surface, δa, can be calculated according to

$$\delta a^{lm} = \frac{1}{(\rho_0 - \rho_w)} \int_{CMB}^{R_{\oplus}} H^l(z) \delta \rho^{lm}(z) dz \tag{2}$$

where $\rho_0 \approx 3330$ kg m^{-3} is the density of the mantle, $\rho_w \approx 1030$ kg m^{-3} is the density of water, and $\delta\rho(z)$ represents the internal density perturbations as a function of depth. H^l is the topography kernel, which depends on both the radial viscosity profile and spherical harmonic degree of the driving density anomaly.

Following the approach of D. McKenzie (pers. comm., 2019), we want to investigate whether density variations imaged by seismic tomography are consistent with global subsidence observations, without imposing the physics of either half-space or plate cooling models at old
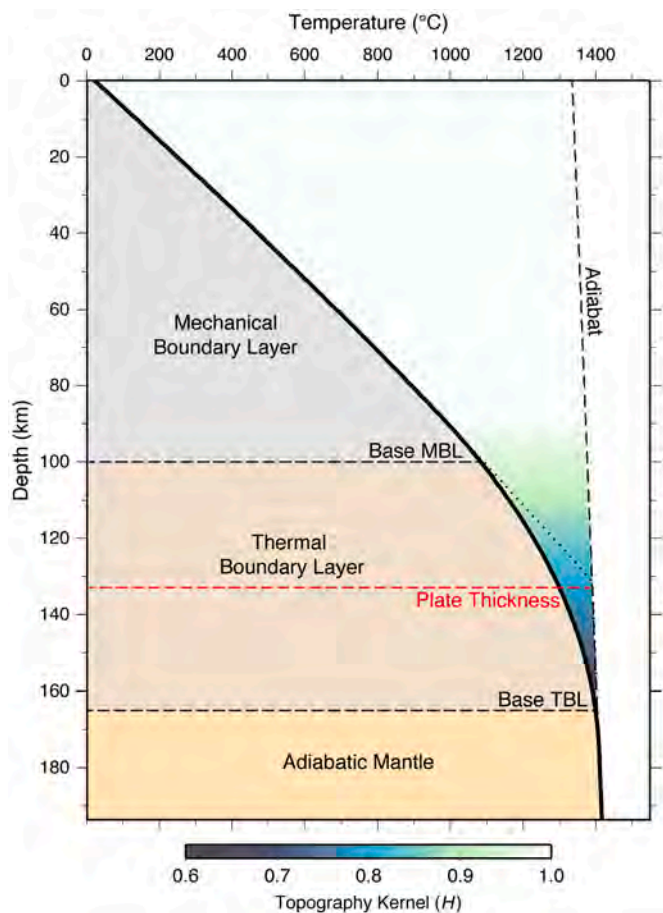

Fig. 14. Schematic of plate model approximation to probable boundary layer structure at old ages. Vertical black dashed line = adiabatic temperature gradient that approximates geotherm during decompression beneath a mid-ocean spreading ridge; solid black line = representative steady-state geotherm for old oceanic lithosphere (McKenzie and Bickle, 1988; McKenzie et al., 2005); dotted black line = plate model geotherm for old oceanic lithosphere; red dashed line = notional plate thickness; horizontal black dashed lines mark transitions from conductively cooling mechanical boundary layer (MBL) into thermal boundary layer (TBL) into the convecting adiabatic mantle; colours = representative topography sensitivity kernel values based on Fig. 10 of Robinson and Parsons (1988).

ages *a priori*. Since both models have almost identical temperature structure at young ages, we calibrate the shear-wave velocity to density conversion using only temperatures from the half-space cooling model for ages ≤ 70 Ma (see Section 3.3). We adopt the SL2013sv tomographic model and expand the resulting density perturbations in spherical harmonics up to a maximum degree, $l_{max} = 90$ (Schaeffer and Lebedev, 2013). Conductive cooling is not expected to reach the transition zone over the course of 200 Myr, so we evaluate the integral in Eq. (2) between 400 km and the surface to determine the expected subsidence as a function of age. We use an instantaneous flow formulation that includes the effects of self-gravitation and compressibility, with free-slip boundary conditions applied at the Earth's surface and core-mantle boundary (see Corrieu et al., 1995; Colli et al., 2016). We adopt the radial viscosity profile of Steinberger et al. (2010) throughout the mantle, but vary asthenospheric (100–220 km) values and compare predicted basement depths and gravity anomalies with the observations in each case (Fig. 15).

Despite calibration against a half-space cooling model for ages ≤ 70 Ma, at older ages, subsidence trends expected from tomographically inferred buoyancy anomalies match both observed basement depths and the predictions of the optimal plate model remarkably well
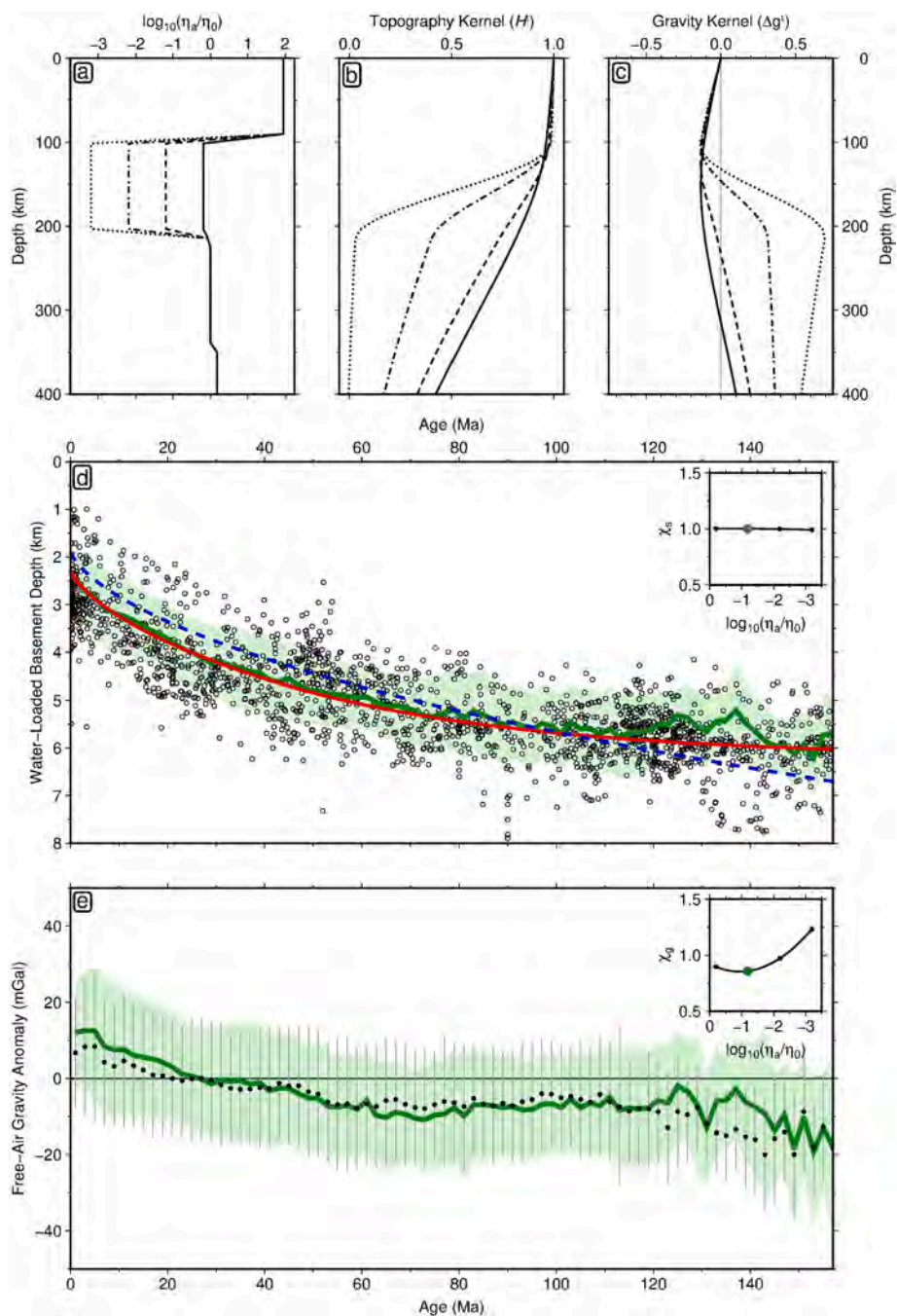
Fig. 15. Global subsidence and gravity predictions from seismic tomography and instantaneous flow. (a) Normalised mantle viscosity profiles. Solid line = Steinberger et al., 2010 normalised by the sub-asthenospheric viscosity in this profile, $\eta_0 = 2.9 \times 10^{20}$ Pa s; dashed line = asthenospheric viscosity, η_a, is decreased by factor of 10; dot-dashed line = η_a decreased by a factor of 100; dotted line = η_a decreased by a factor of 1000; (b) $l = 8$ (~5000 km wavelength) topography kernel for each profile. (c) $l = 8$ (~5000 km wavelength) gravity anomaly kernel for each profile. (d) Global subsidence trends. Black circles = water-loaded oceanic basement depths (Hoggard et al., 2017; Richards et al., 2018); dashed blue line = optimal half-space cooling model from joint fitting of subsidence and heat flow data; red line = optimal plate cooling model; green line/ envelope = mean/2σ for instantaneous flow model output where $\log_{10}(\eta_a/\eta_0) = -1.1$ and density structure is converted from SL2013sv tomography using anelastic parameterisation of Yamauchi and Takei (2016) and parameter values calibrated via inverse modelling with < 70 Ma temperature constraints taken from optimal half-space cooling model (see Section 3.2 & Appendix F). Inset shows misfit between observed basement depth and flow model output as a function of asthenospheric viscosity contrast; green circle = minimum misfit. Note divergence between tomography-based instantaneous flow model output and half-space cooling predictions beyond ~70 Ma, showing better agreement with plate cooling predictions. (e) Same for gravity anomalies. Black circles with vertical bars = mean observed global free-air gravity anomaly with 2σ variations (Sandwell et al., 2014).

(Fig. 15d). There is a positive excursion around 120–140 Ma, which may represent the imprint of small-scale convection, and is approximately consistent with the gentle bathymetric shoaling observed by Crosby et al. (2006). As found by Robinson and Parsons (1988), expected subsidence is relatively insensitive to the asthenospheric viscosity contrast. However, this insensitivity is not replicated by the gravity data, for which a notable change in the quality of fit occurs as the viscosity contrast between the asthenosphere and underlying mantle, $\frac{\eta_a}{\eta_0}$, is varied from $10^0 - 10^{-3}$ (Fig. 15e). Optimal fits occur with a viscosity jump of 10–30, which is consistent both with predictions from the anelastic parameterisation used to determine density structure and with previous studies of mantle rheology (Robinson and Parsons, 1988; Iaffaldano and Lambeck, 2014).

These instantaneous flow calculations implicitly assume that viscosity varies only as a function of depth, an assumption that is probably valid at older lithospheric ages, but may be less well founded in younger areas if the effect of temperature on viscosity dominates the compositional effect of depletion and dehydration by melt removal at the ridge axis. Although some previous studies have attempted to account for these lateral viscosity variations, they do not include seismologically constrained temperature and density anomalies, nor are they carried out in a three-dimensional spherical geometry, making it difficult to draw useful comparisons with the results presented here (Davies, 1988; Huang and Zhong, 2005; Korenaga, 2015; Korenaga and Korenaga, 2016). In any case, the relative insensitivity of dynamic topography and gravity observations to lateral viscosity variations suggests that our global calculations would not change appreciably if this rheological complexity were accounted for (Moucha et al., 2007). Therefore, while future work should aim to address whether the flattening signal we have identified is constant through time or represents a

snapshot of a complex and time-evolving lithosphere-asthenosphere system, our results provide important justification for using a plate cooling model to predict present-day subsidence and gravity anomalies related to lithospheric cooling.

6. Conclusions

The last few decades have seen significant advances in the quantity, quality, and types of observational data collected in the oceanic realm. These new datasets, in combination with improved numerical, theoretical and laboratory-based studies on the thermal and rheological properties of mantle rocks, have considerably improved our understanding of the oceanic lithosphere-asthenosphere system. Subsidence, heat flow, seismological, magnetotelluric, and gravity observations independently suggest that temperature evolution generally approaches a steady-state profile at old ages, rather than continuing to cool indefinitely. This behaviour is shown to be more compatible with plate rather than half-space cooling models, although results are more equivocal in the Atlantic and Indian Oceans than in the Pacific Ocean. Significantly, cooling models that incorporate the latest experimentally derived parameterisations for pressure and temperature-dependence of olivine thermal properties, in addition to a 7 km-thick layer of insulating oceanic crust, are essential for simultaneously fitting both surficial and deep observational data.

Recently, there have been calls to abandon simple cooling parameterisations in favour of more complex reference models that directly account for processes including secular cooling, internal heating, thermal cracking, and small-scale convection (Korenaga, 2020). However, considerable uncertainty surrounds the relevance and magnitude of these processes, and incorporating them into dynamical simulations remains computationally expensive. We therefore suggest that, given the demonstrated ability of plate cooling models to accurately represent the first-order evolution of oceanic lithosphere, these simple models remain of great utility.

Whilst the thermal evolution is increasingly well understood, upper mantle rheology and flow patterns are less well constrained. In particular, although there is convincing evidence for resupply of heat beneath lithosphere at older ages, the plate model gives limited insight into the underlying dynamics. Small-scale convection appears to be the most likely cause of this resupply, but unambiguous observations of this phenomenon remain elusive. Nevertheless, irrespective of reheating mechanism, we have demonstrated that globally averaged flattening signals in subsidence and gravity data can be successfully predicted

with three-dimensional instantaneous flow models that incorporate tomographically inferred density structure. Importantly, this result confirms that the plate model provides a good approximation of the thermal evolution of oceanic lithosphere. Moreover, since we have shown that departures from this background trend correlate well with independent geochemical constraints on mantle temperature, residual deviations can be used to delineate upper mantle thermal anomalies and regions of actively upwelling and downwelling mantle flow.

Although observations of the oceanic lithosphere-asthenosphere system are becoming increasingly consistent with one another, a full understanding of the dynamics, chemical heterogeneity and time-dependent behaviour of this region is still under development. Making progress on these outstanding questions will involve integrated petrological and geophysical modelling, improved constraints on the physical properties of mantle mineral assemblages at relevant pressures and temperatures, and higher-resolution imaging of the seismic and conductivity structure of sub-oceanic mantle. This endeavour is critical to many branches of geoscience, since the relatively simple structure and behaviour of the oceanic upper mantle makes it the ideal foundation on which to build our understanding of Earth's internal structure, dynamics, and its impact on surface processes.

Declaration of competing interest

Acknowledgements

Appendix A. Thermal structure

All cooling models calculated here parameterise the thermal structure of the oceanic lithosphere using the one-dimensional heat equation expressed as

$$\rho(P,T,X)C_P(T,X)\frac{\partial T}{\partial t} = \frac{\partial}{\partial z}\left[k(P,T,X)\frac{\partial T}{\partial z}\right] \tag{A.1}$$

where ρ is density, C_P is heat capacity, and k is thermal conductivity.

We solve Eq. (A.1) numerically with an unconditionally stable time and space-centered Crank-Nicholson finite-difference scheme and a predictor-corrector step (Press et al., 1992). Accordingly, Eq. (A.1) is recast as

$$T_j^{n+1} + A\left[-\frac{k_{j+\frac{1}{2}}^m}{\Delta z_j^m}T_{j+1}^{n+1} + \left(\frac{k_{j+\frac{1}{2}}^m}{\Delta z_j^m} + \frac{k_{j-\frac{1}{2}}^m}{\Delta z_{j-1}^m}\right)T_j^{n+1} - \frac{k_{j-\frac{1}{2}}^m}{\Delta z_{j-1}^m}T_{j-1}^{n+1}\right] \tag{A.2}$$

$$= T_j^n + A\left[\frac{k_{j+\frac{1}{2}}^m}{\Delta z_j^m}T_{j+1}^n - \left(\frac{k_{j+\frac{1}{2}}^m}{\Delta z_j^m} + \frac{k_{j-\frac{1}{2}}^m}{\Delta z_{j-1}^m}\right)T_j^n + \frac{k_{j-\frac{1}{2}}^m}{\Delta z_{j-1}^m}T_{j-1}^n\right] \tag{A.3}$$

where

$$A = \frac{\Delta t}{\rho_j^m C_{Pj}^m(\Delta z_j^m + \Delta z_{j-1}^m)}. \tag{A.4}$$

For the predictor step $m = n$, whilst for the corrector step $m = n + \frac{1}{2}$ (see Richards et al., 2018). These sets of equations are solved by tridiagonal elimination (Press et al., 1992). For incompressible models, Δz_j^m has a constant value of 1 km whilst in compressible models, Δz_j^m is space-centered and scales with thermal contraction. We use a timestep, Δt, of 5 kyr.

Half-space cooling models are calculated in the same manner as plate models except the base of the domain is set to 400 km so that the constant temperature boundary condition has no impact on cooling over the ~200 Myr model timespan. Initial ridge axis temperature profiles for each potential temperature are calculated using the melting parameterisation of Shorttle et al. (2014), with temperature assumed to linearly decrease from the melting parameterisation value at 7 km depth to 0°C at the surface.

Appendix B. Subsidence and heat flow calculations

For cooling models that use constant or temperature-dependent thermal properties, water-loaded subsidence through time, $w(t)$, is calculated using an isostatic balance given by

$$w(t) = \frac{1}{\rho_m - \rho_w} \int_0^\infty [\rho(0, z) - \rho(t, z)] dz$$

(B.1)

where $\rho_m = 3330$ kg m^{-3} is mantle density, $\rho_w = 1030$ kg m^{-3} is the density of seawater, and ρ is the density of the lithosphere that varies as a function of depth, z, and age, t. At $t = 0$, the mid-ocean ridge generally sits in 2–3 km of water, the water-loaded depth to basement, z_b, therefore evolves as $z_b(t) = w(t) + z_r$, where z_r represents the zero-age water depth. In the case of the plate cooling model, conductive cooling of the lithosphere only extends down to a fixed depth, z_p, which can be substituted for ∞ in the upper limit of the integral in Eq. (B.1). Similarly, as half-space cooling models are evaluated numerically within a domain that extends to 400 km depth, ∞ is replaced by this value when calculating subsidence.

The pressure- and temperature-dependent models we evaluate in this study are also compressible, so Eq. B.1 is recast as

$$w(t) = \frac{\rho_b}{\rho_b - \rho_w(t)} \int_0^\infty \left[1 - \frac{\rho(0, z')}{\rho(t, z')} \right] dz'$$

(B.2)

where z' is the Lagrangian depth coordinate that contracts vertically as the lithosphere cools, ρ_b is the density at the depth of compensation (i.e. the shallowest depth where $\rho(t, z')$ and $\rho(0, z')$ are equal) and $\rho_w(t) = 1028 + 0.0024 z_b(t)$ kg m^{-3} to account for the compressibility of seawater (Grose and Afonso, 2013).

For all models, surface heat flow, $H(n\Delta t)$, at time $n\Delta t$ is calculated using

$$H(n\Delta t) = \frac{k_0^n (T_1^n - T_0^n)}{\Delta z_0^n}$$

(B.3)

where k_0^n is the surface conductivity T_0^n is surface temperature, T_1^n is temperature at the next deepest node (1 km depth for incompressible models), and Δz_0^n is the depth increment between these nodes.

Appendix C. Parameterisation of thermal properties

C.1. Constant conductivity models

Constant conductivity models adopt thermal properties from Parsons and Sclater (1977), where $k = 3.138$ W m^{-1} K^{-1}, $\alpha = 3.28 \times 10^{-5}$ K^{-1} and $C_P = 1171.52$ J kg^{-1} K^{-1}.

C.2. Temperature-dependent models

Temperature-dependent models adopt parameterisations derived from experimental data on olivine. Radiative conductivity is based on Hofmeister (2005), lattice diffusivity on Pertermann and Hofmeister (2006), thermal expansivity on Bouhifd et al. (1996), and heat capacity on Korenaga and Korenaga (2016).

Total conductivity is expressed according to

$$k(T) = \kappa_{lat}(T)\rho(T)C_P(T) + k_{rad}(T).$$

(C.1)

Thermal diffusivity, κ_{lat}

$$\kappa_{lat}(T) = \left[\kappa_0 + \kappa_1 \exp\left(-\frac{T - T_0}{\kappa_2} \right) + \kappa_3 \exp\left(-\frac{T - T_0}{\kappa_4} \right) \right] \times 10^{-6},$$

(C.2)

where $\kappa_0 = 0.565$, $\kappa_1 = 0.67$, $\kappa_2 = 590$, $\kappa_3 = 1.4$, $\kappa_4 = 135$, and $T_0 = 273$K. Density is determined using the expression of McKenzie et al. (2005), where

$$\rho(T) = \rho_0 \exp\left\{ -\left[\alpha_0(T - T_0) + \frac{\alpha_1}{2}(T^2 - T_0^2) \right] \right\},$$

(C.3)

and $\alpha_0 = 2.832 \times 10^{-5}$, $\alpha_1 = 0.758 \times 10^{-8}$ and $\rho_0 = 3330$ kg m^{-3}. Heat capacity is evaluated using

$$C_P(T) = c_0 - c_1 T^{-\frac{1}{2}} - c_2 T^{-3},$$

(C.4)

where $c_0 = 1580$, $c_1 = 12230$ and $c_2 = 1694 \times 10^6$.

To calculate radiative conductivity, we adopt the expressions of Grose and Afonso (2013), where

$$k_{rad}(T) = A_r \exp\left[-\frac{(T - T_A)^2}{2x_A^2} \right] + B_r \exp\left[-\frac{(T - T_B)^2}{2x_B^2} \right],$$

(C.5)

where

$$A_r = 1.8 \left[1 - \exp\left(-\frac{d^{1.3}}{0.15}\right) \right] - \left[1 - \exp\left(-\frac{d^{0.5}}{5}\right) \right],$$

$$B_r = 11.7 \exp\left(-\frac{d}{0.159}\right) + 6 \exp\left(-\frac{d^3}{10}\right),$$

$$T_A = 490 + 1850 \exp\left(-\frac{d^{0.315}}{0.825}\right) + 875 \exp\left(-\frac{d}{0.18}\right),$$

$$T_B = 2700 + 9000 \exp\left(-\frac{d^{0.5}}{0.205}\right),$$

$$x_A = 167.5 + 505 \exp\left(-\frac{d^{0.5}}{0.85}\right),$$

$$x_B = 465 + 1700 \exp\left(-\frac{d^{0.94}}{0.175}\right),$$

and $d = 0.5\,\text{cm}$ is the grain size.

C.3. Pressure and temperature-dependent models

Total conductivity in the pressure and temperature-dependent models is expressed using

$$k(P, T) = \kappa_{lat}(T) \rho(P, T) C_P(T) \exp\left[\frac{\partial \ln(k)}{\partial P} P \right] + k_{rad}(T), \tag{C.6}$$

where $\frac{\partial \ln(k)}{\partial P} = 0.05\,\text{W m}^{-1}\,\text{K}^{-1}\,\text{GPa}^{-1}$ (Hofmeister, 2007). The pressure dependence of density is calculated using the approach of Grose and Afonso (2013). First, isothermal volume change, $\left(\frac{V_0}{V}\right)_T$, is calculated at each pressure using a Brent minimisation algorithm and the third-order Birch-Murnaghan equation of state

$$P = \frac{3}{2} K_0 \left[\left(\frac{V_0}{V}\right)_T^{\frac{7}{3}} - \left(\frac{V_0}{V}\right)_T^{\frac{5}{3}} \right] \left\{ 1 + \frac{3}{4}(K_T' - 4) \left[\left(\frac{V_0}{V}\right)_T^{\frac{2}{3}} - 1 \right] \right\} \tag{C.7}$$

where $K_0 = 130\,\text{GPa}$ is the bulk modulus at zero pressure and $K_T' = 4.8$ is the pressure-derivative of the isothermal bulk modulus. The associated isothermal density change with pressure, $\rho(P)$, is given by

$$\rho(P) = \rho_0 \left(\frac{V_0}{V}\right)_T \tag{C.8}$$

where $\rho_0 = 3330\,\text{kg m}^{-3}$ is the density of mantle at surface pressure and temperature. The effect of pressure on thermal expansivity is included according to

$$\frac{\alpha(P, T)}{\alpha(T)} = \left(\frac{V_0}{V}\right)_T \exp\left\{ (\delta_T + 1) \left[\left(\frac{V_0}{V}\right)_T^{-1} - 1 \right] \right\} \tag{C.9}$$

where $\delta_T = 6$ is the Anderson-Grüneisen parameter and $\alpha(T) = \alpha_0 + \alpha_1 T$. Thus, the density as a function of both pressure and temperature, $\rho(P, T)$, can be calculated using

$$\rho(P, T) = \rho_0 \left(\frac{V_0}{V}\right)_T \left\{ 1 - \left[\frac{\alpha(P, T)}{\alpha(T)} \right] \left[\alpha_0 (T - T_0) + \frac{\alpha_1}{2} (T^2 - T_0^2) \right] \right\}. \tag{C.10}$$

In models that also include a 7 km-thick insulating crustal layer we adopt the same parameterisations of thermal conductivity, thermal expansivity and heat capacity as Grose and Afonso (2013) and Korenaga and Korenaga (2016). Thermal conductivity of the crust is formulated as

$$k^c(P, T) = \kappa_{lat}^c(T) \rho^c(P, T) C_P^c(T) \exp\left[\frac{\partial \ln(k)}{\partial P} P \right] + k_{rad}(T), \tag{C.11}$$

with the lattice diffusivity of the crust, κ_{lat}^c is calculated using

$$\kappa_{lat}^c(T) = \left[\kappa_0^c + \kappa_1^c \exp\left(-\frac{T - T_0}{\kappa_2^c}\right) + \kappa_3^c \exp\left(-\frac{T - T_0}{\kappa_4^c}\right) \right] \times 10^{-6}, \tag{C.12}$$

where $\kappa_0^c = 0.432$, $\kappa_1^c = 0.44$, $\kappa_2^c = 380$, $\kappa_3^c = 0.305$, and $\kappa_4^c = 145$. Thermal expansivity of oceanic crust, α^c, is parameterised as α above but with α_0 and α_1 replaced by $\alpha_0^c = 1.639 \times 10^{-5}$ and $\alpha_1^c = 1.322 \times 10^{-8}$, respectively. Crustal heat capacity is calculated assuming the oceanic crust is 65% plagioclase, 15% olivine and 20% clinopyroxene according to

$$
\begin{aligned}
C_P^c &= 0.15 \left[c_0^{ol} + c_1^{ol} T^{-\frac{1}{2}} + c_2^{ol} T^{-3} \right] \\
&\quad + 0.2 \left[c_0^{cpx} + c_1^{cpx} T + c_2^{cpx} T^{-2} + c_3^{cpx} T^{-\frac{1}{2}} + c_4^{cpx} T^2 \right] \\
&\quad + 0.65 \left[c_0^{plag} + c_1^{plag} T + c_2^{plag} T^{-2} + c_3^{plag} T^{-\frac{1}{2}} + c_4^{plag} T^2 \right],
\end{aligned}
\tag{C.13}
$$

where $c_0^{ol} = 1.6108 \times 10^3$, $c_1^{ol} = -1.24788 \times 10^4$, $c_2^{ol} = -1.728477 \times 10^9$; $c_0^{cpx} = 2.1715 \times 10^3$, $c_1^{cpx} = -4.555 \times 10^{-1}$, $c_2^{cpx} = 1.1332 \times 10^6$, $c_3^{cpx} = -2.22716 \times 10^4$, $c_4^{cpx} = 1.299 \times 10^{-4}$; $c_0^{plag} = 1.85757 \times 10^3$, $c_1^{plag} = -3.324 \times 10^{-1}$, $c_2^{plag} = -5.061 \times 10^6$, $c_3^{plag} = -1.64946 \times 10^4$, and $c_4^{plag} = 1.505 \times 10^{-4}$.

Appendix D. Model assessment

All numerical model outputs are jointly fit to subsidence and heat flow observations. The misfit between observed and calculated subsidence is assessed using

$$\chi_s = \sqrt{\frac{1}{M_s} \sum_{i=1}^{M_s} \left(\frac{w_i^o - w_i^c}{\sigma_i} \right)^2} \tag{D.1}$$

where w_i^o and w_i^c are the observed and calculated values of water-loaded subsidence, M_s is the number of measurements, and σ_i is the standard deviation of observed subsidence ($\sim$700 m). Subsidence observations from seafloor younger than 5 Ma are excluded in order to sidestep any possible effects of vigorous hydrothermal circulation near the ridge axis (Grose and Afonso, 2013). The two water-loaded basement depths on seafloor older than 200 Ma are also omitted, leaving 1861 measurements in total.

Misfit between observed and calculated heat flow is calculated using

$$\chi_h = \sqrt{\frac{1}{M_h} \sum_{i=1}^{M_h} \left(\frac{H_i^o - H_i^c}{\sigma_i^*} \right)^2} \tag{D.2}$$

where H_i^o and H_i^c are the observed and calculated values of heat flow, M_h is the number of 2.5 Ma age bins, and σ_i^* is defined as the interquartile range of each 2.5 Ma bin divided by 1.349, in accordance with the statistical analysis of Hasterok et al. (2011). As with the subsidence constraints, observations from seafloor younger than 5 Ma are excluded. Since measurements from seafloor older than 168 Ma are spatially biased and noisy we have excised them from the data compilation, leaving 64 age bins in total. Note that heat flow measurements have been corrected for the effect of sedimentation on conductive geotherms following the methodology outlined in Richards et al. (2018).

These two misfit functions are equally weighted and combined into a single misfit function given by

$$\chi_t = \sqrt{\frac{\chi_s^2 + \chi_h^2}{2}} \tag{D.3}$$

The optimal model for each parameterisation is determined via a parameter sweep with potential temperature fixed at the geochemically constrained value of 1333°C, zero-age ridge depth, z_r, varied between 1 and 4 km at 0.05 km intervals, and, in the case of the plate models, plate thickness, z_p, is also varied between 50 km and 210 km in 5 km increments. The resulting misfit functions are then interpolated at finer resolution to find the global minimum (0.001 km for z_r; 1 km for z_p).

Appendix E. Gravitational response calculation

To calculate the isostatic gravity field associated with different cooling models, we follow the approach outlined by Crosby et al. (2006). First, the oceanic age grid of Richards et al. (2018) is expanded into spherical harmonic coefficients up to and including degree 90. Secondly, a grid of anomalous gravitational potential, $\Delta U(x,y)$, is calculated on this filtered age grid using

$$\Delta U(x,y) = -2\pi G \left[\frac{(\rho_0 - \rho_w) w(x,y)^2}{2} + \int_0^{z_p} z \Delta\rho(x,y,z) dz \right], \tag{E.1}$$

where $\Delta\rho$ is the density contrast between a vertical column of hot asthenosphere at the ridge axis and a column of cooling and thickening lithosphere away from the ridge axis, w is plate subsidence, and z_p is plate thickness or, in the case of half-space cooling models, the base of the model domain, i.e., 400 km. $z = 0$ is at the seabed, $\rho_0 = 3330$ kg m^{-3}, is mantle density at 0°C and $\rho_w = 1030$ kg m^{-3} is the density of water. Thirdly, the grid of ΔU (x,y) values is fitted using real spherical harmonics up to degree 120, generating a suite of coefficients C_{lm} and S_{lm} (where l is the degree and m is the order). Finally, the predicted free-air gravity field can be calculated with the expression

$$\Delta g = -\frac{1}{R} \sum_{l=0}^{120} (l+1) \sum_{m=0}^{l} [C_{lm} \cos(m\lambda) + S_{lm} \sin(m\lambda)] \overline{P}_{lm}(\cos\theta), \tag{E.2}$$

where $\overline{P}_{lm}$ is the normalised Legendre polynomial, λ is longitude, θ is co-latitude and $R = 6371$ km is the Earth's radius (Fig. 4b and c).

Appendix F. Calibrated anelastic parameterisations

For the anelastic parameterisation of Yamauchi and Takei (2016), best-fitting parameter values are calibrated for each seismic tomographic model using an inverse modelling approach and a suite of constraints on upper mantle shear-wave velocity, temperature, attenuation and viscosity. The inversion methodology, mathematical formulations and input constraints we use are identical to those detailed in Richards et al. (2020), except that oceanic V_S versus temperature constraints are obtained from the optimal half-space cooling model ($T_p = 1333$°C; $z_r = 1906$ m), and only for ages up to 70 Ma. Due to the limited vertical resolution of the tomographic models (25–50 km), these constraints were drawn from two depth slices created by averaging V_S between 75–100 km and 100–125 km, with corresponding temperatures obtained at the midpoints (87.5 km and 112.5 km).

Seven parameters are calibrated in total. μ_U^0, $\frac{\partial \mu_U}{\partial T}$, and $\frac{\partial \mu_U}{\partial P}$ describe variation of the unrelaxed shear modulus, μ_U, with pressure and temperature, thereby controlling anharmonic behaviour. η_r, E_a, V_a, $\frac{\partial T_s}{\partial z}$ and define the diffusion creep viscosity, η, and therefore control anelastic behaviour related to diffusionally accommodated grain boundary sliding. The calibrated parameter values are given in Table F.3.

Table F.3
Calibrated parameter values for Yamauchi and Takei (2016) anelastic parameterisation based on different seismic tomographic models. H = weighted misfit (see Richards et al., 2020). Units are: GPa (μ_U^0); GPa $°C^{-1}$ ($\frac{\partial\mu_U}{\partial T}$); dimensionless ($\frac{\partial\mu_U}{\partial P}$); Pa s ($\eta_r$); kJ mol^{-1} (E_a); cm^3 mol^{-1} (V_a); and $°C$ km^{-1} ($\frac{\partial T_S}{\partial z}$).

Model	μ_U^0	$\frac{\partial\mu_U}{\partial T}$	$\frac{\partial\mu_U}{\partial P}$	η_r	E_a	V_a	$\frac{\partial T_S}{\partial z}$	H
SL2013sv	77.9	−0.020	2.70	1.36×10^{22}	300	0.00	0.93	0.64
SEMUM2	79.9	−0.020	2.32	3.12×10^{17}	100	8.35	4.50	0.84
CAM2016	74.0	−0.016	2.31	1.21×10^{22}	295	0.00	0.92	1.06

References

Aagaard, P., Helgeson, H.C., 1982. Thermodynamic and kinetic constraints on reaction rates among minerals and aqueous solutions. I. Theoretical considerations. Am. J. Sci. 282, 237–285.

Abers, G.A., Fischer, K., Hirth, G., Wiens, D., Plank, T., Holtzman, B.K., McCarthy, C., Gazel, E., 2014. Reconciling mantle attenuation-temperature relationships from seismology, petrology, and laboratory measurements. Geochem. Geophys. Geosyst. 15, 3521–3542.

Adenis, A., Debayle, E., Ricard, Y., 2017. Attenuation tomography of the upper mantle. Geophys. Res. Lett. 44, 7715–7724.

Afonso, J.C., Ranalli, G., Fernàndez, M., 2007. Density structure and buoyancy of the oceanic lithosphere revisited. Geophys. Res. Lett. 34, 2–6.

Afonso, J.C., Fernàndez, M., Ranalli, G., Griffin, W.L., Connolly, J.A., 2008a. Integrated geophysical-petrological modeling of the lithosphere and sublithospheric upper mantle: methodology and applications. Geochem. Geophys. Geosyst. 9, Q05008.

Afonso, J.C., Zlotnik, S., Fernandez, M., 2008b. Effects of compositional and rheological stratifications on small-scale convection under the oceans: implications for the thickness of oceanic lithosphere and seafloor flattening. Geophys. Res. Lett. 35, L20308.

Auer, L., Becker, T.W., Boschi, L., Schmerr, N., 2015. Thermal structure, radial anisotropy, and dynamics of oceanic boundary layers. Geophys. Res. Lett. 42, 9740–9749.

Bagley, B., Revenaugh, J., 2008. Upper mantle seismic shear discontinuities of the Pacific. J. Geophys. Res. 113, B12301.

Ball, P., White, N., Masoud, A., Nixon, S., Hoggard, M., Maclennan, J., Stuart, F., Oppenheimer, C., Kröpelin, S., 2019. Quantifying asthenospheric and lithospheric controls on mafic magmatism across North Africa. Geochem. Geophys. Geosyst. 20, 3520–3555.

Ballmer, M., Van Hunen, J., Ito, G., Tackley, P., Bianco, T., 2007. Non-hotspot volcano chains originating from small-scale sublithospheric convection. Geophys. Res. Lett. 34, L23310.

Ballmer, M., Van Hunen, J., Ito, G., Bianco, T., Tackley, P., 2009. Intraplate volcanism with complex age-distance patterns: a case for small-scale sublithospheric convection. Geochem. Geophys. Geosyst. 10, Q06015.

Becker, T., Lebedev, S., Long, M., 2012. On the relationship between azimuthal anisotropy from shear wave splitting and surface wave tomography. Journal of Geophysical Research: Solid Earth 117, B01306.

Beghein, C., Yuan, K., Schmerr, N., Xing, Z., 2014. Changes in seismic anisotropy shed light on the nature of the Gutenberg discontinuity. Science 343, 1237–1240.

Beghein, C., Xing, Z., Goes, S., 2018. Thermal nature and resolution of the lithosphere–asthenosphere boundary under the Pacific from surface waves. Geophys. J. Int. 216, 1441–1465.

Benisek, A., Kroll, H., Dachs, E., 2012. The heat capacity of fayalite at high temperatures. Am. Mineral. 97, 657–660.

Berman, R.G., 1988. Internally-consistent thermodynamic data for minerals in the system $Na_2O-K_2O-CaO-MgO-FeO-Fe_2O_3-Al_2O_3-SiO_2-TiO_2-H_2O-CO_2$. J. Petrol. 29, 445–522.

Berman, R.G., Aranovich, L.Y., 1996. Optimized standard state and solution properties of minerals 1. Model calibration for olivine, orthopyroxene, cordierite, garnet, ilmenite in the system $FeO-MgO-CaO-Al_2O_3-TiO_2-SiO_2$. Cont. Mineral. Pet. 126, 1–24.

Bjerg, E.A., Ntaflos, T., Thöni, M., Aliani, P., Labudia, C.H., 2009. Heterogeneous lithospheric mantle beneath northern Patagonia: evidence from Prahuaniyeu garnet-and spinel-peridotites. J. Petrol. 50, 1267–1298.

Boettcher, M.S., Hirth, G., Evans, B., 2007. Olivine friction at the base of oceanic seismogenic zones. Journal of Geophysical Research: Solid Earth 112, 1–13.

Booth, C.M., Forsyth, D.W., Weeraratne, D.S., 2014. Upper mantle Q structure beneath old seafloor in the western Pacific. Journal of Geophysical Research: Solid Earth 119, 3448–3461.

Bouhifd, M.A., Andrault, D., Fiquet, G., Richet, P., 1996. Thermal expansion of forsterite up to the melting point. Geophys. Res. Lett. 23, 1143–1146.

Boyd, F., 1989. Compositional distinction between oceanic and cratonic lithosphere. Earth Planet. Sci. Lett. 96, 15–26.

Brown, E., Lesher, C., 2016. REEBOX PRO: a forward model simulating melting of thermally and lithologically variable upwelling mantle. Geochem. Geophys. Geosyst. 17, 3929–3968.

Bry, M., White, N., 2007. Reappraising elastic thickness variation at oceanic trenches. Journal of Geophysical Research: Solid Earth 112, B08414.

Buck, W.R., Parmentier, E., 1986. Convection beneath young oceanic lithosphere: implications for thermal structure and gravity. Journal of Geophysical Research: Solid Earth 91, 1961–1974.

Burgos, G., Montagner, J.P., Beucler, E., Capdeville, Y., Mocquet, A., Drilleau, M., 2014.

Oceanic lithosphere-asthenosphere boundary from surface wave dispersion data. Journal of Geophysical Research: Solid Earth 119, 1079–1093.

Busse, F.H., Whitehead, J., 1971. Instabilities of convection rolls in a high Prandtl number fluid. J. Fluid Mech. 47, 305–320.

Cadio, C., Korenaga, J., 2012. Localization of geoid anomalies and the evolution of oceanic lithosphere: a case study from the Mendocino fracture zone. Journal of Geophysical Research: Solid Earth 117.

Cadio, C., Korenaga, J., 2016. Macroscopic strength of oceanic lithosphere revealed by ubiquitous fracture-zone instabilities. Earth Planet. Sci. Lett. 449, 295–301.

Cammarano, F., Goes, S., Vacher, P., Giardini, D., 2003. Inferring upper-mantle temperatures from seismic velocities. Phys. Earth Planet. Inter. 138, 197–222.

Cazenave, A., Lago, B., 1991. Long wavelength topography, seafloor subsidence and flattening. Geophys. Res. Lett. 18, 1257–1260.

Cazenave, A., Monnereau, M., Gibert, D., 1987. Seasat gravity undulations in the central Indian Ocean. Phys. Earth Planet. Inter. 48, 130–141.

Cazenave, A., Dominh, K., Rabinowicz, M., Ceuleneer, G., 1988. Geoid and depth anomalies over ocean swells and troughs: evidence of an increasing trend of the geoid to depth ratio with age of plate. Journal of Geophysical Research: Solid Earth 93, 8064–8077.

Chang, Y.Y., Hsieh, W.P., Tan, E., Chen, J., 2017. Hydration-reduced lattice thermal conductivity of olivine in Earth's upper mantle. Proc. Natl. Acad. Sci. 114, 4078–4081.

Chust, T., Steinle-Neumann, G., Dolejš, D., Schuberth, B., Bunge, H.P., 2017. MMA-EoS: a computational framework for mineralogical thermodynamics. Journal of Geophysical Research: Solid Earth 122, 9881–9920.

Clark, S.P., 1966. Handbook of Physical Constants. Volume 97 Geological Society of America.

Cochran, J.R., Talwani, M., 1977. Free-air gravity anomalies in the world's oceans and their relationship to residual elevation. Geophys. J. Roy. Astr. Soc. 50, 495–552.

Colli, L., Ghelichkhan, S., Bunge, H.P., 2016. On the ratio of dynamic topography and gravity anomalies in a dynamic Earth. Geophys. Res. Lett. 43, 2510–2516.

Connolly, J.A.D., 2005. Computation of phase equilibria by linear programming: a tool for geodynamic modeling and its application to subduction zone decarbonation. Earth Planet. Sci. Lett. 236, 524–541.

Cormier, M.H., Gans, K.D., Wilson, D.S., 2011. Gravity lineaments of the Cocos Plate: evidence for a thermal contraction crack origin. Geochem. Geophys. Geosyst. 12, Q07007.

Corrieu, V., Thoraval, C., Ricard, Y., 1995. Mantle dynamics and geoid Green functions. Geophys. J. Int. 120, 516–523.

Courtney, R.C., White, R.S., 1986. Anomalous heat flow and geoid across the Cape Verde Rise: evidence for dynamic support from a thermal plume in the mantle. Geophys. J. Int. 87, 815–867.

Craig, C.H., McKenzie, D., 1986. The existence of a thin low-viscosity layer beneath the lithosphere. Earth Planet. Sci. Lett. 78, 420–426.

Craig, T.J., Copley, A., 2014. An explanation for the age independence of oceanic elastic thickness estimates from flexural profiles at subduction zones, and implications for continental rheology. Earth Planet. Sci. Lett. 392, 207–216.

Craig, T.J., Copley, A., Jackson, J., 2014. A reassessment of outer-rise seismicity and its implications for the mechanics of oceanic lithosphere. Geophys. J. Int. 197, 63–89.

Crosby, A., McKenzie, D., 2009. An analysis of young ocean depth, gravity and global residual topography. Geophys. J. Int. 178, 1198–1219.

Crosby, A.G., McKenzie, D., Sclater, J.G., 2006. The relationship between depth, age and gravity in the oceans. Geophys. J. Int. 166, 553–573.

Crough, S.T., 1983. The correction for sediment loading on the seafloor. Journal of Geophysical Research: Solid Earth 88, 6449–6454.

Crough, S.T., Jarrard, R.D., 1981. The Marquesas-Line Swell. Journal of Geophysical Research: Solid Earth 86, 11763–11771.

Czarnota, K., Hoggard, M.J., White, N., Winterbourne, J., 2013. Spatial and temporal patterns of Cenozoic dynamic topography around Australia. Geochem. Geophys. Geosyst. 14, 634–658.

Dalton, C.A., Ekström, G., Dziewoński, A.M., 2008. The global attenuation structure of the upper mantle. Journal of Geophysical Research: Solid Earth 113, B09303.

Dalton, C.A., Ekström, G., Dziewoński, A.M., 2009. Global seismological shear velocity and attenuation: a comparison with experimental observations. Earth Planet. Sci. Lett. 284, 65–75.

Dalton, C.A., Langmuir, C.H., Gale, A., 2014. Geophysical and geochemical evidence for deep temperature variations beneath mid-ocean ridges. Science 344, 80–83.

Davaille, A., Jaupart, C., 1994. Onset of thermal convection in fluids with temperature-dependent viscosity: application to the oceanic mantle. Journal of Geophysical Research: Solid Earth 99, 19853–19866.

Davies, D.R., Valentine, A.P., Kramer, S.C., Rawlinson, N., Hoggard, M.J., Eakin, C.M.,

Wilson, C.R., 2019. Earth's multi-scale topographic response to global mantle flow. Nat. Geosci. 12, 845–850.

Davies, G.F., 1988. Ocean bathymetry and mantle convection: 2. Small-scale flow. Journal of Geophysical Research: Solid Earth 93, 10481–10488.

Davies, G.F., 2011. Mantle Convection for Geologists. Cambridge University Press.

de Capitani, C., Petrakakis, K., 2010. The computation of equilibrium assemblage diagrams with Theriak/Domino software. Am. Mineral. 95, 1006–1016.

Debayle, E., Dubuffet, F., Durand, S., 2016. An automatically updated S-wave model of the upper mantle and the depth extent of azimuthal anisotropy. Geophys. Res. Lett. 43, 674–682.

DeLaughter, J., Stein, S., Stein, C.A., 1999. Extraction of a lithospheric cooling signal from oceanwide geoid data. Earth Planet. Sci. Lett. 174, 173–181.

Denlinger, R.P., 1992. A revised estimate for the temperature structure of the oceanic lithosphere. Journal of Geophysical Research: Solid Earth 97, 7219–7222.

Dick, H.J., Fisher, R.L., Bryan, W.B., 1984. Mineralogic variability of the uppermost mantle along mid-ocean ridges. Earth Planet. Sci. Lett. 69, 88–106.

Doin, M.P., Fleitout, L., 1996. Thermal evolution of the oceanic lithosphere: an alternative view. Earth Planet. Sci. Lett. 142, 121–136.

Eilon, Z.C., Abers, G.A., 2017. High seismic attenuation at a mid-ocean ridge reveals the distribution of deep melt. Sci. Adv. 3, e1602829.

Ellam, R., 1992. Lithospheric thickness as a control on basalt geochemistry. Geology 20, 153–156.

Erikson, A., 1973. Initial Report on Downhole Temperature and Shipboard Thermal Conductivity Measurements, Leg 19. Initial Reports of the Deep Sea Drilling Project 19. pp. 643–656.

Farla, R.J., Jackson, I., Fitz Gerald, J.D., Faul, U.H., Zimmerman, M.E., 2012. Dislocation damping and anisotropic seismic wave attenuation in Earth's upper mantle. Science 336, 332–335.

Faul, U., Jackson, I., 2015. Transient creep and strain energy dissipation: an experimental perspective. Annu. Rev. Earth Planet. Sci. 43, 541–569.

Faul, U.H., Jackson, I., 2005. The seismological signature of temperature and grain size variations in the upper mantle. Earth Planet. Sci. Lett. 234, 119–134.

Fei, Y., Saxena, S., 1987. An equation for the heat capacity of solids. Geochimica Cosmochimica Acta 51, 251–254.

Fischer, K.M., Ford, H.A., Abt, D.L., Rychert, C.A., 2010. The lithosphere-asthenosphere boundary. Annual Reviews of Earth and Planetary Sciences 38, 551–575.

Fleitout, L., Yuen, D.A., 1984. Steady state, secondary convection beneath lithospheric plates with temperature- and pressure-dependent viscosity. Journal of Geophysical Research: Solid Earth 89, 9227–9244.

French, S., Lekic, V., Romanowicz, B., 2013. Waveform tomography reveals channeled flow at the base of the oceanic asthenosphere. Science 342, 227–230.

Gaherty, J.B., Eilon, Z.C., Forsyth, D.W., Ekström, G., 2018. Pacific Array: Pacific ORCA (Pacific OBS Research into Convecting Asthenosphere). http://www.obsip.org/experiments/experiment-table/2018/pacific-array/ (Accessed: 2019-09-17).

Gale, A., Dalton, C.A., Langmuir, C.H., Su, Y., Schilling, J.-G., 2013. The mean composition of ocean ridge basalts. Geochem. Geophys. Geosyst. 14, 489–518.

Gale, A., Langmuir, C.H., Dalton, C.A., 2014. The global systematics of ocean ridge basalts and their origin. J. Petrol. 55, 1051–1082.

Gans, K.D., Wilson, D.S., Macdonald, K.C., 2003. Pacific plate gravity lineaments: diffuse extension or thermal contraction? Geochem. Geophys. Geosyst. 4, 1074.

Gasparik, T., 1984. Two-pyroxene thermobarometry with new experimental data in the system CaO–MgO–Al$_2$O$_3$–SiO$_2$. Contrib. Mineral. Petrol. 87, 87–97.

Ghiorso, M.S., Hirschmann, M.M., Reiners, P.W., Kress, V.C., 2002. The pMELTS: a revision of MELTS for improved calculation of phase relations and major element partitioning related to partial melting of the mantle to 3 GPa. Geochem. Geophys. Geosyst. 3, 1–35.

Gibert, B., Schilling, F.R., Tommasi, A., Mainprice, D., 2003. Thermal diffusivity of olivine single-crystals and polycrystalline aggregates at ambient conditions — a comparison. Geophys. Res. Lett. 30, 2172.

Gillet, P., Richet, P., Guyot, F., Fiquet, G., 1991. High-temperature thermodynamic properties of forsterite. J. Geophys. Res. 96, 11805–11816.

Goes, S., Armitage, J., Harmon, N., Smith, H., Huismans, R., 2012. Low seismic velocities below mid-ocean ridges: attenuation versus melt retention. Journal of Geophysical Research: Solid Earth 117, B12403.

Goetze, C., 1978. The mechanisms of creep in olivine. Phil. Trans. R. Soc. A 288, 99–119.

Grose, C.J., 2012. Properties of oceanic lithosphere: revised plate cooling model predictions. Earth Planet. Sci. Lett. 333-334, 250–264.

Grose, C.J., Afonso, J.C., 2013. Comprehensive plate models for the thermal evolution of oceanic lithosphere. Geochem. Geophys. Geosyst. 14, 3751–3778.

Grose, C.J., Afonso, J.C., 2015. The hydrothermal power of oceanic lithosphere. Solid Earth 6, 1131–1155.

Grose, C.J., Afonso, J.C., 2019a. Chemical disequilibria, lithospheric thickness, and the source of ocean island basalts. J. Petrol. 60, 755–790.

Grose, C.J., Afonso, J.C., 2019b. New constraints on the thermal conductivity of the upper mantle from numerical models of radiation transport. Geochem. Geophys. Geosyst. 20, 2378–2394.

Gung, Y., Romanowicz, B., 2004. Q tomography of the upper mantle using three-component long-period waveforms. Geophys. J. Int. 157, 813–830.

Hager, B.H., 1983. Global isostatic geoid anomalies for plate and boundary layer models of the lithosphere. Earth Planet. Sci. Lett. 63, 97–109.

Hansen, L.N., Cheadle, M.J., John, B.E., Swapp, S.M., Dick, H.J., Tucholke, B.E., Tivey, M.A., 2013. Mylonitic deformation at the Kane oceanic core complex: implications for the rheological behavior of oceanic detachment faults. Geochem. Geophys. Geosyst. 14, 3085–3108.

Hansen, L.N., Qi, C., Warren, J.M., 2016. Olivine anisotropy suggests Gutenberg discontinuity is not the base of the lithosphere. Proc. Natl. Acad. Sci. 113, 10503–10506.

Hansen, L.N., Kumamoto, K.M., Thom, C.A., Wallis, D., Durham, W.B., Goldsby, D.L., Breithaupt, T., Meyers, C.D., Kohlstedt, D.L., 2019. Low-temperature plasticity in olivine: grain size, strain hardening, and the strength of the lithosphere. Journal of Geophysical Research: Solid Earth 124, 5427–5449.

Harmon, N., Forsyth, D.W., Scheirer, D.S., 2006. Analysis of gravity and topography in the GLIMPSE study region: isostatic compensation and uplift of the Sojourn and Hotu Matua ridge systems. Journal of Geophysical Research: Solid Earth 111, B11406.

Hasterok, D., 2013. A heat flow based cooling model for tectonic plates. Earth Planet. Sci. Lett. 361, 34–43.

Hasterok, D., Chapman, D.S., Davis, E.E., 2011. Oceanic heat flow: implications for global heat loss. Earth Planet. Sci. Lett. 311, 386–395.

Haxby, W.F., Weissel, J.K., 1986. Evidence for small-scale mantle convection from Seasat altimeter data. Journal of Geophysical Research: Solid Earth 91, 3507–3520.

Herzberg, C., Raterron, P., Zhang, J., 2000. New experimental observations on the anhydrous solidus for peridotite KLB-1. Geochem. Geophys. Geosyst. 1, 1051.

Herzberg, C., Asimow, P.D., Arndt, N., Niu, Y., Lesher, C.M., Fitton, J.G., Cheadle, M.J., Saunders, A.D., 2007. Temperatures in ambient mantle and plumes: constraints from basalts, picrites, and komatiites. Geochem. Geophys. Geosyst. 8, Q02006.

Hess, H.H., 1962. History of ocean basins. In: Petrologic Studies. Geological Society of America, pp. 599–620.

Hillier, J.K., 2010. Subsidence of "normal" seafloor: observations do indicate "flattening". Journal of Geophysical Research: Solid Earth 115, 1–6.

Hillier, J.K., Watts, A.B., 2005. Relationship between depth and age in the North Pacific Ocean. Journal of Geophysical Research: Solid Earth 110, 1–22.

Ho, T., Priestley, K., Debayle, E., 2016. A global horizontal shear velocity model of the upper mantle from multimode Love wave measurements. Geophys. J. Int. 207, 542–561.

Hofmeister, A.M., 1999. Mantle values of thermal conductivity and the geotherm from phonon lifetimes. Science 283, 1699–1706.

Hofmeister, A.M., 2005. Dependence of diffusive radiative transfer on grain-size, temperature, and Fe-content: implications for mantle processes. J. Geodyn. 40, 51–72.

Hofmeister, A.M., 2007. Pressure dependence of thermal transport properties. Proc. Natl. Acad. Sci. 104, 9192–9197.

Hofmeister, A.M., Pertermann, M., 2008. Thermal diffusivity of clinopyroxenes at elevated temperature. Eur. J. Mineral. 20, 537–549.

Hoggard, M.J., White, N., Al-Attar, D., 2016. Global dynamic topography observations reveal limited influence of large-scale mantle flow. Nat. Geosci. 9, 456–463.

Hoggard, M.J., Winterbourne, J., Czarnota, K., White, N., 2017. Oceanic residual depth measurements, the plate cooling model, and global dynamic topography. Journal of Geophysical Research: Solid Earth 122, 2328–2372.

Hoggard, M.J., Czarnota, K., Richards, F.D., Huston, D.L., Jaques, A.L., Ghelichkhan, S., 2020. Global distribution of sediment-hosted metals controlled by craton edge stability. Nat. Geosci. 13, 504–510.

Holmes, R.C., Webb, S.C., Forsyth, D.W., 2007. Crustal structure beneath the gravity lineations in the Gravity Lineations, Intraplate Melting, Petrologic and Seismic Expedition (GLIMPSE) study area from seismic refraction data. Journal of Geophysical Research: Solid Earth 112, B07316.

Holt, A., Royden, L., Becker, T., 2017. The dynamics of double slab subduction. Geophys. J. Int. 209, 250–265.

Houseman, G., McKenzie, D.P., 1982. Numerical experiments on the onset of convective instability in the Earth's mantle. Geophys. J. Int. 68, 133–164.

Huang, J., Zhong, S., 2005. Sublithospheric small-scale convection and its implications for the residual topography at old ocean basins and the plate model. Journal of Geophysical Research: Solid Earth 110, 1–17.

Huang, J., Niu, F., Gordon, R.G., Cui, C., 2015. Accurate focal depth determination of oceanic earthquakes using water-column reverberation and some implications for the shrinking plate hypothesis. Earth Planet. Sci. Lett. 432, 133–141.

Hunter, J., Watts, A., 2016. Gravity anomalies, flexure and mantle rheology seaward of circum-Pacific trenches. Geophys. J. Int. 207, 288–316.

Huppert, K.L., Perron, J.T., Royden, L.H., 2020. Hotspot swells and the lifespan of volcanic ocean islands. Sci. Adv. 6, eaaw6906.

Iaffaldano, G., Lambeck, K., 2014. Pacific plate-motion change at the time of the Hawaiian-Emperor bend constrains the viscosity of Earth's asthenosphere. Geophys. Res. Lett. 41, 3398–3406.

Isaak, D.G., 1992. High-temperature elasticity of iron-bearing olivines. Journal of Geophysical Research: Solid Earth 97, 1871–1885.

Jackson, I., Faul, U.H., 2010. Grain size-sensitive viscoelastic relaxation in olivine: towards a robust laboratory-based model for seismological application. Phys. Earth Planet. Inter. 183, 151–163.

Jackson, I., Faul, U.H., Fitz Gerald, J.D., Tan, B.H., 2004. Shear wave attenuation and dispersion in melt-bearing olivine polycrystals: 1. Specimen fabrication and mechanical testing. Journal of Geophysical Research: Solid Earth 109, B06201.

Jackson, I., Faul, U.H., Skelton, R., 2014. Elastically accommodated grain-boundary sliding: new insights from experiment and modeling. Phys. Earth Planet. Inter. 228, 203–210.

Jackson, J.M., Palko, J.W., Andrault, D., Sinogeikin, S.V., Lakshtanov, D.L., Wang, J., Bass, J.D., Zha, C.-S., 2003. Thermal expansion of natural orthoenstatite to 1473 K. Eur. J. Mineral. 15, 469–473.

Jaroslow, G., Hirth, G., Dick, H., 1996. Abyssal peridotite mylonites: implications for grain-size sensitive flow and strain localization in the oceanic lithosphere. Tectonophysics 256, 17–37.

Jarvis, G.T., Peltier, W., 1982. Mantle convection as a boundary layer phenomenon. Geophys. J. Int. 68, 389–427.

Jennings, E.S., Holland, T.J.B., 2015. A simple thermodynamic model for melting of peridotite in the system NCFMASOCr. J. Petrol. 56, 869–892.

Johnson, H.P., Carlson, R.L., 1992. Variation of sea floor depth with age: a test of models

based on drilling results. Geophys. Res. Lett. 19, 1971–1974.

Karaoğlu, H., Romanowicz, B., 2018. Inferring global upper-mantle shear attenuation structure by waveform tomography using the spectral element method. Geophys. J. Int. 213, 1536–1558.

Katsura, T., Yoneda, A., Yamazaki, D., Yoshino, T., Ito, E., 2010. Adiabatic temperature profile in the mantle. Phys. Earth Planet. Inter. 183, 212–218.

Katz, R.F., Spiegelman, M., Langmuir, C.H., 2003. A new parameterization of hydrous mantle melting. Geochem. Geophys. Geosyst. 4, 1073.

Kawakatsu, H., Utada, H., 2017. Seismic and electrical signatures of the litho-sphere–asthenosphere system of the normal oceanic mantle. Annu. Rev. Earth Planet. Sci. 45, 139–167.

Kawakatsu, H., Kumar, P., Takei, Y., Shinohara, M., Kanazawa, T., Araki, E., Suyehiro, K., 2009. Seismic evidence for sharp lithosphere-asthenosphere boundaries of oceanic plates. Science 324, 499–502.

Kelemen, P., Kikawa, E., Miller, D., 2004. Shipboard scientific party, 2004. Leg 209 summary. In: Proceedings of the Ocean Drilling Program, Initial Reports, 209. Ocean Drilling Program, College Station TX, pp. 1–139.

Kelemen, P.B., Dick, H.J., Quick, J.E., 1992. Formation of harzburgite by pervasive melt/rock reaction in the upper mantle. Nature 358, 635–641.

King, D.S.H., Marone, C., 2012. Frictional properties of olivine at high temperature with applications to the strength and dynamics of the oceanic lithosphere. Journal of Geophysical Research: Solid Earth 117, 1–16.

Klein, E.M., Langmuir, C.H., 1987. Global correlations of ocean ridge basalt chemistry with axial depth and crustal thickness. J. Geophys. Res. 92, 8089–8115.

Klemme, S., 2004. The influence of Cr on the garnet-spinel transition in the Earth's mantle: experiments in the system MgO-Cr_2O_3-SiO_2 and thermodynamic modelling. Lithos 77, 639–646.

Korenaga, J., 2007. Thermal cracking and the deep hydration of oceanic lithosphere: a key to the generation of plate tectonics? J. Geophys. Res. 112, B05408.

Korenaga, J., 2008. Urey ratio and the structure and evolution of Earth's mantle. Rev. Geophys. 46, RG2007.

Korenaga, J., 2009. How does small-scale convection manifest in surface heat flux? Earth Planet. Sci. Lett. 287, 329–332.

Korenaga, J., 2015. Seafloor topography and the thermal budget of Earth. Geol. Soc. Am. Spec. Pap. 514, 167–185.

Korenaga, J., 2020. Plate tectonics and surface environment: role of the oceanic upper mantle. Earth Sci. Rev. 205, 103185.

Korenaga, J., Jordan, T.H., 2002. Onset of convection with temperature-and depth-de-pendent viscosity. Geophys. Res. Lett. 29, 1923.

Korenaga, J., Jordan, T.H., 2003a. Linear stability analysis of Richter rolls. Geophys. Res. Lett. 30, 2157.

Korenaga, J., Jordan, T.H., 2003b. Physics of multiscale convection in Earth's mantle: onset of sublithospheric convection. J. Geophys. Res. 108.

Korenaga, J., Jordan, T.H., 2004. Physics of multiscale convection in Earth's mantle: evolution of sublithospheric convection. Journal of Geophysical Research: Solid Earth 109, B01405.

Korenaga, T., Korenaga, J., 2008. Subsidence of normal oceanic lithosphere, apparent thermal expansivity, and seafloor flattening. Earth Planet. Sci. Lett. 268, 41–51.

Korenaga, T., Korenaga, J., 2016. Evolution of young oceanic lithosphere and the meaning of seafloor subsidence rate. Journal of Geophysical Research: Solid Earth 121, 6315–6332.

Kumar, P., Kawakatsu, H., Shinohara, M., Kanazawa, T., Araki, E., Suyehiro, K., 2011. P and S receiver function analysis of seafloor borehole broadband seismic data. Journal of Geophysical Research: Solid Earth 116, B12309.

Lambeck, K., 1972. Gravity anomalies over ocean ridges. Geophys. J. Int. 30, 37–53.

Lattard, D., Engelmann, R., Kontny, A., Sauerzapf, U., 2006. Curie temperatures of syn-thetic titanomagnetites in the Fe-Ti-O system: effects of composition, crystal chem-istry, and thermomagnetic methods. Journal of Geophysical Research: Solid Earth 111, B12S28.

Le Douaran, S., Parsons, B.E., 1982. A note on the correction of ocean floor depths for sediment loading. Journal of Geophysical Research: Solid Earth 87, 4715–4722.

Lee, C.T.A., Lenardic, A., Cooper, C.M., Niu, F., Levander, A., 2005. The role of chemical boundary layers in regulating the thickness of continental and oceanic thermal boundary layers. Earth Planet. Sci. Lett. 230, 379–395.

Lev, E., Hager, B.H., 2008. Rayleigh-Taylor instabilities with anisotropic lithospheric viscosity. Geophys. J. Int. 173, 806–814.

Li, C.F., Wang, J., 2018. Thermal structures of the Pacific lithosphere from magnetic anomaly inversion. Earth and Planetary Physics 2, 52–66.

Li, C.F., Wang, J., Lin, J., Wang, T., 2013. Thermal evolution of the North Atlantic li-thosphere: new constraints from magnetic anomaly inversion with a fractal magne-tization model. Geochem. Geophys. Geosyst. 14, 5078–5105.

Li, C.F., Lu, Y., Wang, J., 2017. A global reference model of Curie-point depths based on EMAG2. Sci. Rep. 7, 45129.

Lin, P.Y.P., Gaherty, J.B., Jin, G., Collins, J.A., Lizarralde, D., Evans, R.L., Hirth, G., 2016. High-resolution seismic constraints on flow dynamics in the oceanic asthenosphere. Nature 535, 538–541.

Lister, C.R.B., 1972. On the thermal balance of a mid-ocean ridge. Geophys. J. Int. 26, 515–535.

Lister, C.R.B., 1980. Heat flow and hydrothermal circulation. Annu. Rev. Earth Planet. Sci. 8, 95–117.

Lodhia, B.H., Roberts, G.G., Fraser, A.J., Fishwick, S., Goes, S., Jarvis, J., 2018. Continental margin subsidence from shallow mantle convection: example from West Africa. Earth Planet. Sci. Lett. 481, 350–361.

Ma, Z., Dalton, C.A., 2019. Evidence for dehydration-modulated small-scale convection in the oceanic upper mantle from seafloor bathymetry and Rayleigh wave phase velo-city. Earth Planet. Sci. Lett. 510, 12–25.

Maia, M., Diament, M., 1991. An analysis of the altimetric geoid in various wavebands in the central Pacific Ocean: constraints on the origin of intraplate features. Tectonophysics 190, 133–153.

Marquart, G., Schmeling, H., Braun, A., 1999. Small-scale instabilities below the cooling oceanic lithosphere. Geophys. J. Int. 138, 655–666.

Matthews, S., Shorttle, O., Maclennan, J., 2016. The temperature of the Icelandic mantle from olivine-spinel aluminum exchange thermometry. Geochem. Geophys. Geosyst. 17, 4725–4752.

Mayhew, M., 1982. Application of satellite magnetic anomaly data to Curie isotherm mapping. Journal of Geophysical Research: Solid Earth 87, 4846–4854.

McCarthy, C., Takei, Y., 2011. Anelasticity and viscosity of partially molten rock ana-logue: toward seismic detection of small quantities of melt. Geophys. Res. Lett. 38, 3–7.

McKenzie, D., 2018. A geologist reflects on a long career. Annu. Rev. Earth Planet. Sci. 46, 1–20.

McKenzie, D., Bickle, M.J., 1988. The volume and composition of melt generated by extension of the lithosphere. J. Petrol. 29, 625–679.

McKenzie, D., Weiss, N., 1975. Speculations on the thermal and tectonic history of the Earth. Geophys. J. Int. 42, 131–174.

McKenzie, D., Jackson, J., Priestley, K., 2005. Thermal structure of oceanic and con-tinental lithosphere. Earth Planet. Sci. Lett. 233, 337–349.

McKenzie, D.P., 1967. Some remarks on heat flow and gravity anomalies. J. Geophys. Res. 72, 6261–6273.

Menard, H.W., 1973. Depth anomalies and the bobbing motion of drifting islands. J. Geophys. Res. 78, 5128–5137.

Mishra, J.K., Gordon, R.G., 2016. The rigid-plate and shrinking-plate hypotheses: im-plications for the azimuths of transform faults. Tectonics 35, 1827–1842.

Mooney, W.D., Prodehl, C., Pavlenkova, N.I., 2002. Seismic velocity structure of the continental lithosphere from controlled source data. Int. Geophys. Ser. 81, 887–910.

Morgan, J.P., Smith, W.H., 1992. Flattening of the sea-floor depth-age curve as a response to asthenospheric flow. Nature 359, 524–527.

Morgan, J.P., Morgan, W.J., Zhang, Y.S., Smith, W.H.F., 1995. Observational hints for a plume-fed, suboceanic asthenosphere and its role in mantle convection. J. Geophys. Res. 100, 12753–12767.

Moucha, R., Forte, A., Mitrovica, J., Daradich, A., 2007. Lateral variations in mantle rheology: implications for convection related surface observables and inferred visc-osity models. Geophys. J. Int. 169, 113–135.

Müller, R.D., Sdrolias, M., Gaina, C., Roest, W.R., 2008. Age, spreading rates, and spreading asymmetry of the world's ocean crust. Geochem. Geophys. Geosyst. 9, Q04006.

Müller, R.D., Seton, M., Zahirovic, S., Williams, S.E., Matthews, K.J., Wright, N.M., Shephard, G.E., Maloney, K.T., Barnett-Moore, N., Bower, D.J., Cannon, J., 2016. Ocean basin evolution and global-scale reorganization events since Pangea breakup. Annual Reviews of Earth and Planetary Science Letters 44, 107–138.

Natarov, S.I., Conrad, C.P., 2012. The role of Poiseuille flow in creating depth-variation of asthenospheric shear. Geophys. J. Int. 190, 1297–1310.

Niu, Y., Green, D.H., 2018. The petrological control on the lithosphere-asthenosphere boundary (LAB) beneath ocean basins. Earth Sci. Rev. 185, 301–307.

Niu, Y., Wilson, M., Humphreys, E.R., O'Hara, M.J., 2011. The origin of intra-plate ocean island basalts (OIB): the lid effect and its geodynamic implications. J. Petrol. 52, 1443–1468.

Parsons, B., Daly, S., 1983. The relationship between surface topography, gravity anomalies, and temperature structure of convection. Journal of Geophysical Research: Solid Earth 88, 1129–1144.

Parsons, B., McKenzie, D., 1978. Mantle convection and the thermal structure of the plates. Journal of Geophysical Research: Solid Earth 83, 4485–4496.

Parsons, B., Sclater, J.G., 1977. An analysis of the variation of ocean floor bathymetry and heat flow with age. J. Geophys. Res. 82, 803–827.

Pavlenkova, N., 1996. General features of the uppermost mantle stratification from long-range seismic profiles. Tectonophysics 264, 261–278.

Pertermann, M., Hofmeister, A.M., 2006. Thermal diffusivity of olivine-group minerals at high temperature. Am. Mineral. 91, 1747–1760.

Pilet, S., Baker, M.B., Müntener, O., Stolper, E.M., 2011. Monte Carlo simulations of metasomatic enrichment in the lithosphere and implications for the source of alkaline basalts. J. Petrol. 52, 1415–1442.

Pollack, H.N., 1980. On the use of the volumetric thermal expansion coefficient in models of ocean floor topography. Tectonophysics 64, T45–T47.

Powell, R., Holland, T., 1988. An internally consistent dataset with uncertainties and correlations: 3. Applications to geobarometry, worked examples and a computer program. J. Metamorph. Geol. 6, 173–204.

Press, W.H., Teukolsky, S.A., Vetterling, W.T., Flannery, B.P., 1992. Numerical Recipes in C (2nd Ed.): The Art of Scientific Computing. Cambridge University Press, New York, NY, USA.

Priestley, K., McKenzie, D., 2006. The thermal structure of the lithosphere from shear wave velocities. Earth Planet. Sci. Lett. 244, 285–301.

Priestley, K., McKenzie, D., 2013. The relationship between shear wave velocity, tem-perature, attenuation and viscosity in the shallow part of the mantle. Earth Planet. Sci. Lett. 381, 78–91.

Putirka, K., 1999. Melting depths and mantle heterogeneity beneath Hawaii and the East Pacific Rise: constraints from Na/Ti and rare earth element ratios. Journal of Geophysical Research: Solid Earth 104, 2817–2829.

Ricard, Y., Durand, S., Montagner, J.P., Chambat, F., 2014. Is there seismic attenuation in the mantle? Earth Planet. Sci. Lett. 388, 257–264.

Richards, F., Hoggard, M., Cowton, L., White, N.J., 2018. Reassessing the thermal structure of oceanic lithosphere with revised global inventories of basement depths and heat flow measurements. Journal of Geophysical Research: Solid Earth 123,

9136–9161.

Richards, F.D., Hoggard, M.J., White, N.J., Ghelichkhan, S., 2020. Quantifying the relationship between short-wavelength dynamic topography and thermomechanical structure of the upper mantle using calibrated parameterization of anelasticity. J. Geophys. Res. Solid Earth 125, e2019JB019062.

Richards, M.A., Hager, B.H., 1984. Geoid anomalies in a dynamic Earth. Journal of Geophysical Research: Solid Earth 89, 5987–6002.

Richardson, W.P., Stein, S., Stein, C.A., Zuber, M.T., 1995. Geoid data and thermal structure of the oceanic lithosphere. Geophys. Res. Lett. 22, 1913–1916.

Richter, F.M., 1973. Convection and the large-scale circulation of the mantle. J. Geophys. Res. 78, 8735–8745.

Richter, F.M., McKenzie, D.P., 1981. On some consequences and possible causes of layered mantle convection. Journal of Geophysical Research: Solid Earth 86, 6133–6142.

Richter, F.M., Parsons, B., 1975. On the interaction of two scales of convection in the mantle. J. Geophys. Res. 80, 2529–2541.

Ritzwoller, M.H., Shapiro, N.M., Zhong, S.J., 2004. Cooling history of the Pacific lithosphere. Earth Planet. Sci. Lett. 226, 69–84.

Robinson, E.M., Parsons, B., 1988. Effect of a shallow low-viscosity zone on the formation of midplate swells. Journal of Geophysical Research: Solid Earth 93, 3144–3156.

Romanowicz, B., Mitchell, B.J., 2015. Deep Earth structure: Q of the Earth from crust to core. In: Treatise on Geophysics, 2nd ed. Elsevier, pp. 789–827.

Rowley, D.B., 2018. Oceanic axial depth and age-depth distribution of oceanic lithosphere: comparison of magnetic anomaly picks versus age-grid models. Lithosphere 11, 21–43.

Russell, J.B., Gaherty, J.B., Lin, P.Y.P., Lizarralde, D., Collins, J.A., Hirth, G., Evans, R.L., 2019. High-resolution constraints on Pacific upper mantle petrofabric inferred from surface-wave anisotropy. Journal of Geophysical Research: Solid Earth 124, 631–657.

Rychert, C.A., Harmon, N., 2017. Constraints on the anisotropic contributions to velocity discontinuities at 60 km depth beneath the Pacific. Geochem. Geophys. Geosyst. 18, 2855–2871.

Rychert, C.A., Shearer, P.M., 2011. Imaging the lithosphere-asthenosphere boundary beneath the Pacific using SS waveform modeling. Journal of Geophysical Research: Solid Earth 116, B07307.

Rychert, C.A., Schmerr, N., Harmon, N., 2012. The Pacific lithosphere-asthenosphere boundary: seismic imaging and anisotropic constraints from SS waveforms. Geochem. Geophys. Geosyst. 13, Q0AK10.

Sandwell, D.T., Winterer, E.L., Mammerickx, J., Duncan, R.A., Lynch, M.A., Levitt, D.A., Johnson, C.L., 1995. Evidence for diffuse extension of the Pacific plate from Pukapuka ridges and cross-grain gravity lineations. Journal of Geophysical Research: Solid Earth 100, 15087–15099.

Sandwell, D.T., Muller, R.D., Smith, W.H.F., Garcia, E., Francis, R., 2014. New global marine gravity model from CryoSat-2 and Jason-1 reveals buried tectonic structure. Science 346, 65–67.

Sarafian, E., Evans, R.L., Collins, J.A., Elsenbeck, J., Gaetani, G.A., Gaherty, J.B., Hirth, G., Lizarralde, D., 2015. The electrical structure of the central Pacific upper mantle constrained by the NoMelt experiment. Geochem. Geophys. Geosyst. 16, 1115–1132.

Schaeffer, A., Lebedev, S., Becker, T., 2016. Azimuthal seismic anisotropy in the Earth's upper mantle and the thickness of tectonic plates. Geophys. J. Int. 207, 901–933.

Schaeffer, A.J., Lebedev, S., 2013. Global shear speed structure of the upper mantle and transition zone. Geophys. J. Int. 194, 417–449.

Schatz, J.F., Simmons, G., 1972. Thermal conductivity of Earth materials at high temperatures. J. Geophys. Res. 77, 6966–6983.

Schmerr, N., 2012. The Gutenberg discontinuity: melt at the lithosphere-asthenosphere boundary. Science 335, 1480–1483.

Schutt, D.L., Lesher, C.E., 2006. Effects of melt depletion on the density and seismic velocity of garnet and spinel lherzolite. Journal of Geophysical Research: Solid Earth 111, 1–24.

Sclater, J.G., Francheteau, J., 1970. The implications of terrestrial heat flow observations on current tectonic and geochemical models of the crust and upper mantle of the Earth. Geophys. J. Int. 20, 509–542.

Selby, N.D., Woodhouse, J.H., 2002. The Q structure of the upper mantle: constraints from Rayleigh wave amplitudes. Journal of Geophysical Research: Solid Earth 107, ESE 5-1–ESE 5-11.

Selway, K., O'Donnell, J., 2019. A small, unextractable melt fraction as the cause for the low velocity zone. Earth Planet. Sci. Lett. 517, 117–124.

Shankland, T., Waff, H., 1977. Partial melting and electrical conductivity anomalies in the upper mantle. J. Geophys. Res. 82, 5409–5417.

Shankland, T., Nitsan, U., Duba, A., 1979. Optical absorption and radiative heat transport in olivine at high temperature. Journal of Geophysical Research: Solid Earth 84, 1603–1610.

Sheriff, R.E., 2002. Encyclopedic Dictionary of Applied Geophysics. Society of Exploration Geophysicists.

Sheriff, R.E., Geldart, L.P., 1995. Exploration Seismology. Cambridge University Press.

Shito, A., Suetsugu, D., Furumura, T., 2015. Evolution of the oceanic lithosphere inferred from Po/So waves traveling in the Philippine Sea Plate. Journal of Geophysical Research: Solid Earth 120, 5238–5248.

Shorttle, O., Maclennan, J., Lambart, S., 2014. Quantifying lithological variability in the mantle. Earth Planet. Sci. Lett. 395, 24–40.

Sleep, N.H., 1990. Hotspots and mantle plumes: some phenomenology. Journal of Geophysical Research: Solid Earth 95, 6715–6736.

Sleep, N.H., 1994. Lithospheric thinning by midplate mantle plumes and the thermal history of hot plume material ponded at sublithospheric depths. Journal of Geophysical Research: Solid Earth 99, 9327–9343.

Sleep, N.H., 2011. Small-scale convection beneath oceans and continents. Chin. Sci. Bull. 56, 1292–1317.

Steer, D.N., Knapp, J.H., Brown, L.D., 1998. Super-deep reflection profiling: exploring the continental mantle lid. Tectonophysics 286, 111–121.

Stein, C.A., Stein, S., 1992. A model for the global variation in oceanic depth and heat flow with lithospheric age. Nature 356, 133–135.

Steinberger, B., Becker, T.W., 2018. A comparison of lithospheric thickness models. Tectonophysics 746, 325–338.

Steinberger, B., Werner, S.C., Torsvik, T.H., 2010. Deep versus shallow origin of gravity anomalies, topography and volcanism on Earth, Venus and Mars. Icarus 207, 564–577.

Steinberger, B., Conrad, C.P., Osei Tutu, A., Hoggard, M.J., 2019. On the amplitude of dynamic topography at spherical harmonic degree two. Tectonophysics 760, 221–228.

Stern, T.A., Henrys, S.A., Okaya, D., Louie, J.N., Savage, M.K., Lamb, S., Sato, H., Sutherland, R., Iwasaki, T., 2015. A seismic reflection image for the base of a tectonic plate. Nature 518, 85–88.

Stixrude, L., Lithgow-Bertelloni, C., 2005. Mineralogy and elasticity of the oceanic upper mantle: origin of the low-velocity zone. Journal of Geophysical Research: Solid Earth 110, B03204.

Stotz, I.L., Iaffaldano, G., Davies, D.R., 2018. Pressure-driven Poiseuille flow: a major component of the torque-balance governing Pacific plate motion. Geophys. Res. Lett. 45, 117–125.

Takei, Y., 2017. Effects of partial melting on seismic velocity and attenuation: a new insight from experiments. Annual Reviews of Earth and Planetary Sciences 45, 1–25.

Takei, Y., Karasawa, F., Yamauchi, H., 2014. Temperature, grain size, and chemical controls on polycrystal anelasticity over a broad frequency range extending into the seismic range. Journal of Geophysical Research: Solid Earth 119, 5414–5443.

Takeuchi, N., Kawakatsu, H., Shiobara, H., Isse, T., Sugioka, H., Ito, A., Utada, H., 2017. Determination of intrinsic attenuation in the oceanic lithosphere-asthenosphere system. Science 358, 1593–1596.

Thybo, H., 2006. The heterogeneous upper mantle low velocity zone. Tectonophysics 416, 53–79.

Tirone, M., Sessing, J., 2017. Petrological geodynamics of mantle melting I. AlphaMELTS + multiphase flow: dynamic equilibrium melting, method and results. Front. Earth Sci. 5, 81.

Tonegawa, T., Helffrich, G., 2012. Basal reflector under the Philippine Sea plate. Geophys. J. Int. 189, 659–668.

Turcotte, D.L., Oxburgh, E.R., 1967. Finite amplitude convective cells and continental drift. J. Fluid Mech. 28, 29–42.

Turcotte, D.L., Schubert, G., 2002. Geodynamics, 2nd ed. Cambridge University Press, Cambridge.

Tweed, L.E.L., Spiegelman, M.W., Kelemen, P.B., Ghiorso, M.S., Evans, O., Wolf, A.S., 2019. A tractable approach to coupling the thermodynamics, kinetics, and fluid dynamics of mantle melting. In: AGU Fall Meeting, San Francisco, USA.

Utada, H., 2019. Ocean bottom geophysical array studies may reveal the cause of seafloor flattening. Earth Planet. Sci. Lett. 518, 100–107.

van Hunen, J., Zhong, S., Shapiro, N.M., Ritzwoller, M.H., 2005. New evidence for dislocation creep from 3-D geodynamic modeling of the Pacific upper mantle structure. Earth Planet. Sci. Lett. 238, 146–155.

Vine, F.J., Matthews, D.H., 1963. Magnetic anomalies over oceanic ridges. Nature 199, 947–949.

Von Herzen, R.P., Uyeda, S., 1963. Heat flow through the eastern Pacific ocean floor. J. Geophys. Res. 68, 4219–4250.

Waples, D.W., Waples, J.S., 2004. A review and evaluation of specific heat capacities of rocks, minerals, and subsurface fluids. Part 2: fluids and porous rocks. Nat. Resour. Res. 13, 123–130.

Warren, J.M., Hirth, G., 2006. Grain size sensitive deformation mechanisms in naturally deformed peridotites. Earth Planet. Sci. Lett. 248, 438–450.

Watkins, C.E., Conrad, C.P., 2018. Constraints on dynamic topography from asymmetric subsidence of the mid-ocean ridges. Earth Planet. Sci. Lett. 484, 264–275.

Watson, S., McKenzie, D., 1991. Melt generation by plumes: a study of Hawaiian volcanism. J. Petrol. 32, 501–537.

Watts, A., Zhong, S., Hunter, J., 2013. The behavior of the lithosphere on seismic to geologic timescales. Annual Reviews of Earth and Planetary Sciences 41, 443–468.

Weeraratne, D.S., Forsyth, D.W., Yang, Y., Webb, S.C., 2007. Rayleigh wave tomography beneath intraplate volcanic ridges in the South Pacific. Journal of Geophysical Research: Solid Earth 112, B06303.

Wen, L., Anderson, D.L., 1997. Slabs, hotspots, cratons and mantle convection revealed from residual seismic tomography in the upper mantle. Phys. Earth Planet. Inter. 99, 131–144.

White, R.S., McKenzie, D., O'Nions, R.K., 1992. Oceanic crustal thickness from seismic measurements and rare earth element inversions. J. Geophys. Res. 97, 19683–19715.

Wiens, D.A., Stein, S., 1983. Age dependence of oceanic intraplate seismicity and implications for lithospheric evolution. J. Geophys. Res. 88, 6455–6468.

Wilson, J.T., 1965. A new class of faults and their bearing on continental drift. Nature 207, 343–347.

Winterbourne, J., Crosby, A., White, N., 2009. Depth, age and dynamic topography of oceanic lithosphere beneath heavily sedimented Atlantic margins. Earth Planet. Sci. Lett. 287, 137–151.

Winterbourne, J., White, N., Crosby, A., 2014. Accurate measurements of residual topography from the oceanic realm. Tectonics 33, 982–1015.

Xu, W., Lithgow-Bertelloni, C., Stixrude, L., Ritsema, J., 2008. The effect of bulk composition and temperature on mantle seismic structure. Earth Planet. Sci. Lett. 275, 70–79.

Xu, Y., Shankland, T.J., Linhardt, S., Rubie, D.C., Langenhorst, F., Klasinski, K., 2004. Thermal diffusivity and conductivity of olivine, wadsleyite and ringwoodite to 20 GPa and 1373 K. Phys. Earth Planet. Inter. 143, 321–336.

Yamamoto, M., Morgan, J.P., Morgan, W.J., 2007. Global plume-fed asthenosphere flow-I: motivation and model development. Special Papers - Geological Society of America 430, 165.

Yamauchi, H., Takei, Y., 2016. Polycrystal anelasticity at near-solidus temperatures. Journal of Geophysical Research: Solid Earth 121, 7790–7820.

Yang, T., Gurnis, M., 2016. Dynamic topography, gravity and the role of lateral viscosity variations from inversion of global mantle flow. Geophys. J. Int. 207, 1186–1202.

Yang, Y., Forsyth, D.W., Weeraratne, D.S., 2007. Seismic attenuation near the East Pacific Rise and the origin of the low-velocity zone. Earth Planet. Sci. Lett. 258, 260–268.

Yoshino, T., Katsura, T., 2013. Electrical conductivity of mantle minerals: role of water in conductivity anomalies. Annu. Rev. Earth Planet. Sci. 41, 605–628.

Zaranek, S.E., Parmentier, E., 2004. The onset of convection in fluids with strongly temperature-dependent viscosity cooled from above with implications for planetary lithospheres. Earth Planet. Sci. Lett. 224, 371–386.

Zhou, H., Dick, H.J., 2013. Thin crust as evidence for depleted mantle supporting the Marion Rise. Nature 494, 195–200.